

PROCESSING, COMPOSITIONAL RANGE, AND MECHANICAL BEHAVIOR OF
THE $\text{Mo}_3\text{Si}_3\text{C}$ INTERMETALLIC COMPOUND

By

ELI N. ROSS

A DISSERTATION PRESENTED TO THE GRADUATE SCHOOL
OF THE UNIVERSITY OF FLORIDA IN PARTIAL FULFILLMENT
OF THE REQUIREMENTS FOR THE DEGREE OF
DOCTOR OF PHILOSOPHY

UNIVERSITY OF FLORIDA

1999

For Mom, Dad, Barbara, Carl, and Nera.

ACKNOWLEDGMENTS

Like most endeavors requiring significant effort, the research and writing of a dissertation involves the support and assistance of a large number of people. To begin with, I am very grateful to Andre Costa e Silva for introducing me to the basics of research, while always maintaining his patience and good humor. To Paul Eason and Luisa Amelia Dempere, I am indebted for their many useful discussions and team-approach to problem solving. For his ability to take on equipment and computer problems, willingness to help and positive attitude, Ryan Kaufman deserves recognition. I am also appreciative of Dr. Fereshteh Ebrahimi, Dr. Jian Hu, and Dr. Ozer Unal, who provided invaluable assistance during the mechanical testing portion of this work. The assistance of Wayne Acree at the Major Analytical Instrumentation Center was important to the materials characterization efforts in this study.

I consider myself very fortunate to have worked under the direction of Dr. Michael Kaufman during my time at Florida—his inquisitive nature, approachability, and broad knowledge base have served me very well during this research effort. I am also glad to have forged a friendship with Dr. Kaufman, as have many of his present and former students. I am also grateful to the other members of my graduate committee for adding their perspectives and guidance toward producing a focused research project. I would also like to thank Jim Cotton for his encouragement and pragmatism during our discussions. Finally and most importantly, the support and love given to me by my friends and family members has been an integral part of my graduate studies, without which none of this would have been possible.

TABLE OF CONTENTS

	page
ACKNOWLEDGEMENTS	iii
ABSTRACT	vi
CHAPTERS	
1 INTRODUCTION	1
2 LITERATURE REVIEW	4
2.1 Drivers and Materials Requirements for High-Temperature Applications	4
2.2 Binary Silicide Compounds for High-Temperature Applications	6
2.2.1 Molybdenum Disilicide	7
2.2.1.1 Processing of MoSi ₂ and its composites	9
2.2.1.2 Low-temperature mechanical behavior	14
2.2.1.3 Elevated-temperature mechanical behavior	15
2.2.1.4 Carbon additions to MoSi ₂	17
2.2.2 M ₃ Si ₃ Compounds	18
2.3 Ternary Silicide Compounds	21
2.3.1 Mo-Si-Al System	23
2.3.2 Mo-Si-B System	24
2.3.3 Mo-Si-C System and the Mo ₅ Si ₃ C Phase	24
2.3.3.1 Thermodynamics of the Mo-Si-C system	24
2.3.3.2 Atomic arrangement and crystal structure of Mo ₅ Si ₃ C	27
2.3.3.3 Processing, microstructures and properties of Mo ₅ Si ₃ C	27
3 PROCESSING AND COMPOSITIONAL RANGE ISSUES	33
3.1 Introduction	33
3.2 Materials and Experimental Procedures	33
3.2.1 Raw Materials	33
3.2.2 Processing Routes	34
3.2.2.1 Arc melting	35
3.2.2.2 Powder mixing and hot pressing	35
3.2.2.3 Mechanical alloying + hot pressing	37
3.2.3 Materials Characterization and Analysis	41
3.2.3.1 Physical properties	41

3.2.3.2 Microstructural analysis	42
3.2.3.3 Phase identification and compositional analysis	44
3.3 Results and Discussion	48
3.3.1 Processing	48
3.3.1.1 Compositions studied	48
3.3.1.2 Arc melting	49
3.3.1.3 Powder processing methods	52
3.3.2 Compositional Range of $\text{Mo}_5\text{Si}_3\text{C}$	68
3.3.2.1 Width of $\text{Mo}_5\text{Si}_3\text{C}$ single-phase field	70
3.3.2.2 Height of $\text{Mo}_5\text{Si}_3\text{C}$ single-phase field	72
3.3.2.3 Heat treatment	72
3.3.2.4 Conclusions	76
3.4 Summary and Conclusions	77
4 MECHANICAL BEHAVIOR OF $\text{Mo}_5\text{Si}_3\text{C}$ -BASED MATERIALS	82
4.1 Introduction	82
4.2 Experimental Procedure	83
4.2.1 Sample Characterization and Analysis	83
4.2.2 Hardness Testing	84
4.2.3 Indentation Fracture Toughness Measurements	84
4.2.4 Elevated Temperature Compression Testing	85
4.2.5 Four-Point Bend Testing	88
4.3 Results and Discussion	90
4.3.1 Microstructural Characterization of Test Specimens	90
4.3.2 Hardness and Fracture Toughness Measurements	93
4.3.3 High-Temperature Deformation Behavior in Compression	97
4.3.4 Four-Point Flexure Testing of $\text{Mo}_5\text{Si}_3\text{C}$	111
4.3.5 Mechanical Property Comparisons with Other Silicide Materials	116
4.3.6 Effectiveness of Alloying to Improve Ductility	118
4.4 Summary and Conclusions	122
5 GENERAL DISCUSSION AND CONCLUSIONS	124
APPENDICES	
A SELECTED HOT PRESS TIME-TEMPERATURE-PRESSURE PROFILES	129
B SELECTED COMPRESSIVE STRESS-STRAIN CURVES	132
REFERENCES	136
BIOGRAPHICAL SKETCH	149

Abstract of Dissertation Presented to the Graduate School
of the University of Florida in Partial Fulfillment of the
Requirements for the Degree of Doctor of Philosophy

PROCESSING, COMPOSITIONAL RANGE, AND MECHANICAL BEHAVIOR OF
THE $\text{Mo}_5\text{Si}_3\text{C}$ INTERMETALLIC COMPOUND

By

Eli N. Ross

August 1999

Chairman: Michael J. Kaufman
Major Department: Materials Science and Engineering

The intermetallic compound $\text{Mo}_5\text{Si}_3\text{C}$ was studied in order to examine optimal processing methods, elevated temperature mechanical behavior, and the influence of crystal symmetry on the potential for improved room temperature ductility/toughness in ternary silicides. During the course of the investigation, samples were produced using non-consumable arc melting and vacuum hot pressing of either blended or mechanically alloyed powders. The most significant challenge to the production of single-phase $\text{Mo}_5\text{Si}_3\text{C}$ was the significantly narrower range of homogeneity for the ternary compound than originally reported. The primary reason for this discrepancy is thought to be the use of x-ray diffraction (XRD) as the sole means of phase identification in the original study, whereas the current work augmented XRD with other microstructural analysis techniques.

Further complicating the processing of $\text{Mo}_5\text{Si}_3\text{C}$ was the occurrence of composition shifts during powder processing. These shifts in stoichiometry were correlated to observed microstructural features and likely the result of thermodynamically favored reactions between silica present in the starting powders and carbon. Because of these complications, materials for mechanical testing typically contained between one and 6 volume percent of

phases other than $\text{Mo}_3\text{Si}_3\text{C}$, with samples having the nominal composition $\text{Mo}_{4.8}\text{Si}_3\text{C}_{0.87}$ closest to single phase.

An average microhardness value of 13.2 GPa was recorded for the ternary phase at room temperature, and an indentation fracture toughness of approximately $2.5 \text{ MPa}\cdot\text{m}^{1/2}$ was determined. In the temperature range 1000 to 1300°C, materials tested in compression displayed properties that were highly strain rate and grain size dependent, indicating the influence of boundary-controlled deformation mechanisms. The behavior of samples tested in four-point bending at 1200°C showed similar behavior, with larger grain size materials failing after limited deformation while finer grain size materials deformed readily.

Examination of deformed specimens using transmission electron microscopy indicated that slip in $\text{Mo}_3\text{Si}_3\text{C}$ occurs through motion of $c[0001]$ -type dislocations at temperatures above 1000°C. This is consistent with the observed lack of improvement in the toughness or ductility of $\text{Mo}_3\text{Si}_3\text{C}$, resulting from any positive contributions due to crystal symmetry being nullified by the intrinsically high resistance of the complex $\text{Mo}_3\text{Si}_3\text{C}$ crystal lattice to the generation and motion of dislocations.

CHAPTER 1 INTRODUCTION

In recent years, there has been renewed interest in silicide compounds, MoSi_2 in particular, as possible high-temperature structural materials. In the case of MoSi_2 , this is largely due to its high melting point (2020°C) [1], moderate density (6.24 g/cm^3) [2], measurable deformation at elevated temperatures [3] and excellent oxidation and corrosion resistance to $\sim 1700^\circ\text{C}$ due to the presence of an adherent, passivating silica scale [4]. These properties are direct analogues to several of the primary materials requirements for future generations of gas-turbine engines, namely increased operating temperatures, reduction of rotating weight and environmental resistance. However, like the majority of intermetallic materials investigated as potential replacements for current superalloys, MoSi_2 -based materials suffer from inadequate low-temperature fracture toughness and poor formability. In addition, silicides typically show a drop in strength at elevated temperatures and poor resistance to creep deformation.

In all likelihood, the mechanical property shortcomings of MoSi_2 have origins both intrinsic and extrinsic. For example, the high bond strengths and low-symmetry crystal structure ($C11_1$, tetragonal) of MoSi_2 significantly limit the potential for ductility at low temperatures [5], while the presence of a glassy SiO_2 phase in powder processed MoSi_2 may act as fracture initiation sites at ambient temperatures and adversely affect strength at elevated temperatures because of grain refinement and viscous flow at high temperatures [6]. Because of this, researchers have attempted to address these issues through microstructural control, compositing, and alloying additions [7].

Due to the high melting point of MoSi_2 , traditional casting and forming processes have for the most part been abandoned in favor of powder-based methods. Techniques

such as handling of siliceous powders in inert atmospheres to suppress silica formation, etching of powders to remove SiO_2 , and reduction of silica through alloying additions have all been attempted as ways to control the presence of silica in MoSi_2 microstructures [8, 9]. The effectiveness of these approaches has varied, especially given the difficulty in isolating the detrimental effects of silica from other possible mechanisms at work. Some success in improving the high temperature properties of MoSi_2 has been achieved through use of reinforcing phases; SiC has been widely utilized in both conventional and *in situ* compositing techniques in long fiber, whisker and particulate forms [3]. Ternary alloying additions (e.g., Al, B, Cr, Ge, Hf, Nb, Re) to MoSi_2 have been studied as a possible way to improve mechanical properties through solid solution strengthening and second phase precipitation effects, although property improvements have been minimal [10].

In a few intermetallic systems, it has been shown that macro-alloying to produce ternary and higher-order compounds having higher symmetry (e.g., cubic, hexagonal) crystal structures results in a significant increase in room-temperature ductility compared with the parent binary compound [11]. Phase stability studies in Mo-Si-X systems have shown the presence of a number of ternary silicide phases, many of which exhibit higher symmetry crystal structures than tetragonal MoSi_2 . Included among these phases is the hexagonal D_{8h} compound $\text{Mo}_3\text{Si}_3\text{C}$. As the only ternary phase identified in the Mo-Si-C system, $\text{Mo}_3\text{Si}_3\text{C}$ has attracted recent interest since it is the third component in *in situ* processed MoSi_2 -SiC composites [12, 13]. Very little is known about the physical and mechanical properties of ternary hexagonal silicide compounds such as $\text{Mo}_3\text{Si}_3\text{C}$, including whether enough mobile, low energy dislocations are present at low temperatures to make the potential activation of additional slip systems meaningful. Other than selected ternary isotherms, little information exists regarding the processing of these compounds. In processing approaches which take advantage of solid-solution strengthening, eutectic transformations, or displacement reactions, the importance of having accurate

thermodynamic data is vital, especially since many desirable phase combinations exist adjacent to phase regions of undesirable, low melting (e.g., Si) phases [14].

From the standpoint of investigating the relationship between higher-symmetry crystal structures and mechanical properties in ternary silicides [15-17] and clarifying the mechanical behavior of the third component of *in situ* processed $\text{MoSi}_2\text{-SiC}$ composites [12], the $\text{Mo}_3\text{Si}_3\text{C}$ phase seems a reasonable choice for further study. In addition, it may be possible during the course of the study to clarify uncertainties as to the actual compositional range of the ternary silicide compound [18, 19].

The initial stages of this project were concerned with optimizing methods for the processing of single-phase $\text{Mo}_3\text{Si}_3\text{C}$. While it was possible to screen out methods that were obviously unsuited to the production of samples for mechanical testing, process optimization was greatly complicated by confusion surrounding the size of the $\text{Mo}_3\text{Si}_3\text{C}$ single phase field. A systematic reexamination of compositions near the $\text{Mo}_3\text{Si}_3\text{C}$ phase field was used to determine the stoichiometry which had the highest potential for yielding single-phase materials. After refinement of the best combinations of processing and composition for producing near-single phase $\text{Mo}_3\text{Si}_3\text{C}$ over a range of grain sizes, an assessment of baseline mechanical properties for $\text{Mo}_3\text{Si}_3\text{C}$ -based materials was conducted and these properties compared with those of other candidate high-temperature materials. In light of the sizeable number of interrelated process, composition, and property variables inherent in this materials system, an emphasis was placed on such issues as sample quality control, process monitoring, extensive documentation, and efficient design of experiments.

CHAPTER 2 LITERATURE REVIEW

2.1 Drivers and Materials Requirements for High-Temperature Applications

The search for materials systems capable of withstanding higher temperatures and extreme environments while maintaining strength is one of the foremost technical challenges to continued improvements in performance, efficiency, and reliability of gas turbine engines for aerospace and power generation applications. Representative materials requirements and properties of interest for these high-temperature applications are given in Table 2.1.

Table 2.1 Materials and process requirements for high-temperature materials in gas turbine engines [20-22].

<i>Property/Issue</i>	<i>Relevance</i>
<i>High melting point</i>	Higher operating temperatures
<i>Strength retention at high temperatures</i>	Rotating, load bearing critical structures
<i>High elastic modulus</i>	Resist centrifugal stresses, thermal fatigue
<i>Creep resistance</i>	Increased operating life, reliability
<i>Environmental resistance</i>	Combustion products, water vapor, cyclic exposure
<i>Low, high cycle fatigue resistance</i>	Increased operating life, less downtime
<i>High thermal conductivity, low thermal expansion</i>	Reduced cooling requirements; efficient design, coating compatibility
<i>Low density</i>	Rotating parts, power/weight
<i>Toughness, impact resistance</i>	Design flexibility, foreign object damage, low temp. = most of service life
<i>Ease of forming, machining, joining</i>	Use existing processes, increased yield
<i>Cost</i>	Benefits must justify development costs

Nickel-based superalloys are currently the material of choice for the most demanding of gas turbine engine applications; alloy optimization and development of single-crystal technologies along with active cooling and thermal barrier coatings have led to significant increases in engine operating temperatures [23]. An increase in turbine engine operating temperature has as a direct result an increase in specific power output while at the same time leading to a decrease in fuel consumption [21]. In spite of the documented success of superalloy systems, current superalloys operate within $\sim 100^{\circ}\text{C}$ of their incipient melting temperatures [23], thus in order for increases in engine operating temperatures to continue, new materials systems need to be considered.

Potential materials systems to replace superalloys include refractory metals, advanced ceramics, and intermetallics. Refractory metals maintain strength to very high temperatures ($\sim 1600^{\circ}\text{C}$) and can be processed to have acceptable ductility and toughness, but oxidize readily above $\sim 500^{\circ}\text{C}$ and specific properties suffer because of high material densities [24]. Ceramics are attractive because of high strength at temperature, excellent creep resistance, low density, and usually good oxidation resistance, but a lack of ductility and poor electrical conductivity makes forming very difficult and their generally low fracture toughness values limit design options [25].

Intermetallics, mainly aluminides and silicides, exhibit good oxidation resistance, low specific gravity, high strength and modulus, good thermal conductivity, and can, in some cases, be formed using traditional techniques such as casting and forging [11]. In addition, they often have sufficient electrical conductivity to be machined using electrical-discharge methods [26]. However, achieving a balance of properties in a particular material or even an alloy system has proven to be very difficult. Intermetallics are also generally plagued by low impact resistance, high notch and strain rate sensitivity, and poor ductility at room temperature [27]. Because of their potentially attractive properties for high-temperature structural applications, considerable effort has gone into the study and

development of materials such as nickel, iron, and titanium aluminides, Laves phases, and silicide compounds [11, 28-30].

2.2 Binary Silicide Compounds for High-Temperature Applications

Over 130 different binary silicide compounds have been identified and characterized [3] with roughly 75 percent being transition metal silicides. Most of these compounds show mixed covalent-metallic bond character, maintain ordered structures until melting, and exist as line compounds having little compositional variation. Current applications for silicides include heating elements, coatings (Figure 2.1), thermal protection systems, diesel engine glow plugs, infrared detectors, and electrical contacts for improved microelectronic device performance [7, 26, 31].



Figure 2.1 Silicide coating on Nb-alloy (C-103) afterburner flaps of Pratt & Whitney F-100 engine [32].

2.2.1 Molybdenum Disilicide

Of the refractory metal silicides, MoSi_2 has generated by far the most interest for high-temperature applications, primarily because of its excellent oxidation resistance which extends to 1700°C [33]. In addition to oxidation resistance, MoSi_2 also exhibits a high melting point (2020°C) [1] and a density of 6.24 g/cm^3 [2], roughly 25 % less than a typical Ni-based superalloy. In the absence of impurities, MoSi_2 maintains the tetragonal C11_b structure (Figure 2.2) up to its melting point. Molybdenum disilicide has seen application in various forms for almost 90 years [3], with the most well-known being the use of MoSi_2 as the primary component of oxidation-resistant Kanthal Super heating elements (Figure 2.3).

Research by W.A. Maxwell and coworkers in the early 1950s was probably the first to consider MoSi_2 -based compounds for use as high-temperature structural materials [34, 35]. Maxwell's work noted that monolithic MoSi_2 exhibits several undesirable features, namely a decrease in strength and poor creep resistance at high temperatures and lack of ductility at room temperature (RT). In fact Maxwell and others [36, 37] investigated doping MoSi_2 with carbon and the use of Al_2O_3 as a potential reinforcement for MoSi_2 as early as 1953. However, at that time, with gas turbine engine development still in its early stages, the primary technological demands of aerospace could readily be satisfied with traditional metallic materials. This, combined with a limited design base for use of brittle materials in structural applications, is a probable explanation for the limited amount of work on MoSi_2 from the time of Maxwell and his contemporaries until about the mid-1980s [3].

By the end of the 1980s, promising work in identifying toughening mechanisms in structural ceramics [38] combined with a recognized need for increased operating temperatures and lower weight in aerospace applications [21] brought about a renewed interest in MoSi_2 as a potential replacement for current superalloy materials. From Table 2.2, MoSi_2 compares fairly well with other intermetallics and ceramics being developed to

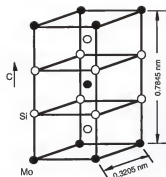


Figure 2.2 Tetragonal C11_b (tI6) crystal structure of MoSi₂ having six atoms per unit cell [39].

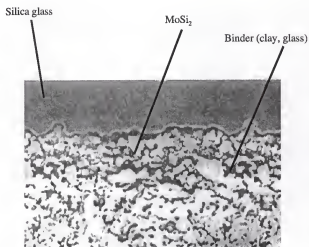


Figure 2.3 Microstructure of Kanthal Super heating element (1000x) showing two phase matrix covered by protective silica layer [40]

replace current superalloys. However, the same problems Maxwell first observed of low toughness at ambient temperatures and poor creep resistance at elevated temperatures remain as challenges to the realization of MoSi₂-based materials for structural applications.

Table 2.2 Comparison of physical and mechanical properties of MoSi₂ with other current and potential high temperature materials. Where scatter existed in the literature, values were averaged. Thermal conductivity (k) is given in W/m K at 1000 K, coefficient of thermal expansion (CTE) data is in ppm/K, elastic modulus (E) is in GPa, toughness values (K_{IC}) are in MPa·m^{1/2}, and yield strength (YS) is given in MPa. Values for Nb alloy and superalloy are typical for these metals, [3, 7, 11, 41-47].

Material	T _m (°C)	Density (g/cc)	Oxidation Limit (°C)	k	CTE	E (RT)	K _{IC} (RT)	Y.S. (1000°C)
MoSi ₂	2020	6.24	1700	35	8.1	440	3	300
NiAl	1647	5.86	1227	70	15	294	5	35
TiAl	1440	3.9	900	22	12	162	25	150
Ti ₃ Al	1602	4.2	652	7	10	145	10	40
SiC	2500	3.18	1600	60	5	480	3.5	>2000
Al ₂ O ₃	2050	4	>1600	7	10	380	5	1000
Nb-alloy	2400	8.6	600	45	8	90	30	300
superalloy	1350	8.4	920	12	14	206	50	300

2.2.1.1 Processing of MoSi₂ and its composites

Processing techniques for polycrystalline MoSi₂-based materials can be grouped into either powder-based or melt-based routes. Of the powder processing routes, hot pressing (HP) is the most commonly used for the production of both monolithic MoSi₂ and composites [48]. Starting powders for HP can be either elemental or pre-alloyed in nature, with the latter usually requiring higher consolidation temperatures; typically pressing temperatures range from 1500°C to 1800°C in either vacuum or inert gas atmospheres [49]. When high consolidation temperatures (~1800°C) are used, weight losses on the order of 20% have been reported for carbon-doped MoSi₂ materials [50], the result of a lower-melting ternary Mo-Si-C eutectic being expelled from the die. Another contributing factor to weight losses at high temperatures, especially during vacuum HP, is the high vapor

pressure of silicon over MoSi_2 (Figure 2.4); for this reason, high-temperature consolidation is often done in an inert gas environment [13].

A variation on HP is hot isostatic pressing (HIP), which typically results in higher density, higher purity MoSi_2 materials [51], although it is a more complex process than HP. To vary the scale of MoSi_2 microstructures produced by HP or HIP, options include, (1) changing the particle size of the major element or compound in the starting powders [52], (2) affecting grain growth and sintering kinetics by varying pressing temperature and time [49], and (3) refinement of the MoSi_2 matrix by introduction of second phase particles which retard grain growth by a Zener drag mechanism [53]. Reactive sintering techniques such as reactive HP/HIP or self-propagating high-temperature synthesis (SHS) take advantage of the thermal energy generated by exothermic reactions between starting powders, which in some cases dramatically reduces processing times [54]. Residual porosity and limited microstructural control are limitations of typical reactive sintering processes [48]. Another method successfully used to produce MoSi_2 composites is low-pressure plasma-spray deposition, which typically results in very fine microstructures [55]. Mechanical alloying (MA), high-energy impact milling of powders, has been used to synthesize sub-micron silicide powders, often with simultaneous solid-state phase formation (Figure 2.5). These features allow for the consolidation of MoSi_2 and its composites at lower temperatures with the resultant materials having highly refined microstructures [56-58]. One concern common to all variants of MA is contamination of the powder charge by the milling vial and balls [48]; the severity of impurity pickup during MA is primarily a function of the relative hardness of the powder and milling media and the solubility of the impurity elements in the powder constituents.

For all powder processing routes, oxygen contamination of the powders is a key concern. Elemental Si or silicide powders exposed to the atmosphere rapidly oxidize to form SiO_2 on their surfaces; in the absence of process modifications, 5 – 10 Vol.% of the

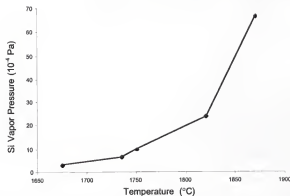


Figure 2.4 Plot of equilibrium dissociation pressure of Si over MoSi_2 , adapted from Searcy and Tharp [59].

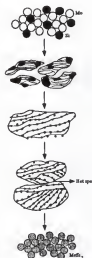


Figure 2.5 Schematic representation of the mechanical alloying process for MoSi_2 , wherein repeated cold-welding and fracture processes lead to the formation of the silicide from its constituent powders [48].

oxide will be retained in the consolidated materials (Figure 2.6), typically as pockets of amorphous silica at the grain boundaries and triple points [34, 35, 60, 61]. The amount of silica present in a silicide material is a strong function of starting particle size of the siliceous powders; fine particles having large surface area typically have the highest percentage of oxide, meaning that control of atmosphere is crucial during processes that result in very fine powders, such as MA or plasma-spray [48, 49]. Minimizing the amount of silica in MoSi_2 -based materials is important primarily from the standpoint of strength at high temperatures, where the glassy silica is thought to soften and accelerate strength degradation through grain boundary sliding [62].

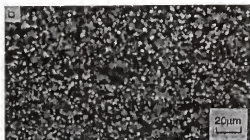


Figure 2.6 Light optical micrograph of MoSi_2 under polarized light, revealing intergranular silica particles (white spots). Silica is incorporated into powder processed MoSi_2 from oxides resident on the starting powders [9].

In spite of some disagreement over the exact role of silica in elevated temperature deformation, it is generally agreed that it is an undesirable feature in consolidated MoSi_2 . Accordingly, a large amount of effort has focused on ways to remove the oxide phase from MoSi_2 , including powder etching [35], inert-gas handling [9] and intentional additions of elements such as Al, C, Zr, or rare earth elements which reduce silica [34, 58, 63–66]. Table 2.3 shows typical oxygen content values for MoSi_2 powders and consolidated parts,

indicating a wide variation depending on powder size and processing parameters. The effects of silica on mechanical properties will be discussed in greater detail below.

Table 2.3 Oxygen content in MoSi₂ powders and consolidated material [63].

Material	Form	Oxygen (Wt.%)	Source/Investigator
MoSi ₂	powder, 45-75 μ m	0.3	Cerac [®]
MoSi ₂	powder, <45 μ m	2.02 \pm 0.4	Alfa AESAR [®]
MoSi ₂ , MA	powder, <1 μ m	4.07 \pm 0.016	Jayashankar
MoSi ₂ + SiC, <i>in situ</i>	hot-pressed	0.167	Jayashankar
MoSi ₂ + SiC, blended	hot-pressed	1.71 \pm 0.05	Jayashankar
MoSi ₂ , glove box processing	hot isostatically-pressed	0.16-0.22	Rockwell
MoSi ₂ , MA+ Glove box processing	hot-pressed	0.1	Los Alamos

Various fiber, whisker, and particulate reinforcements have been combined with MoSi₂ using variants on the aforementioned powder processing techniques. Ductile reinforcements include Nb [67-69], Ta [67] and W [68]; complications associated with refractory metal reinforcements include the need for diffusion barrier coatings on the metal because of their thermodynamic incompatibility with MoSi₂ [48, 64, 68] and the reduced oxidation resistance of the composites [48]. A number of oxide and non-oxide ceramics, in fiber, whisker, and particulate form, have also been used as reinforcing phases for MoSi₂ and other silicides [3, 48, 49, 70]. One common way of producing MoSi₂-ceramic composites are so-called *in situ* processing routes which take advantage of solid-state displacement reactions [71] to produce fine, homogeneously distributed, and thermodynamically stable reinforcements including SiC [13, 72] and TiB₂ [73]. The processing and properties of *in situ* MoSi₂-SiC composites will be discussed in more detail below.

Of the melt-based methods, the simplest is non-consumable arc melting, which has been used extensively in alloying studies involving MoSi_2 [10, 74, 75]. Another process of note is the patented exothermic dispersion or XD™ process, wherein ceramic particulates are precipitated within in a MoSi_2 -based master alloy; composites produced via XD™ have the advantage of being inherently stable thermodynamically and can contain high volume fractions of uniformly distributed ceramic, in excess of 40 Vol.% [76, 77]. Two other melt-based silicide composite processing methods are *in situ* melt processing [78] and eutectic solidification [79, 80].

2.2.1.2 Low-temperature mechanical behavior

Studies of deformation mechanisms in MoSi_2 single crystals have indicated the following possible slip systems and temperature ranges: $\{001\}\langle 100\rangle$ (20°C) [81]; $\{110\}\langle 111\rangle$, $\{013\}\frac{1}{2}\langle 331\rangle$ ($900 - 1500^\circ\text{C}$) [82]; $\{1\bar{1}1\}\langle 110\rangle$ (1200°C) [83]; $\{011\}\langle 100\rangle$ (RT), $\{1\bar{1}0\}\frac{1}{2}\langle 111\rangle$ ($T > 600^\circ\text{C}$) [84]. Even in the temperature regimes in which multiple slip systems are operative in MoSi_2 , it has been shown that at most four of these represent independent slip mechanisms [84]. It was shown by von Mises [85] that for a single crystal to undergo an arbitrary shape change, a minimum of five independent slip mechanisms must be operative; by extension, the deformation of a collection of randomly oriented single-crystals (i.e., polycrystalline material) also requires five independent slip systems [86]. Note that the von Mises criterion is a necessary, but not sufficient condition, since deformation also requires the availability of mobile dislocations [27].

At ambient temperatures, polycrystalline MoSi_2 fractures in a brittle manner with zero ductility and exhibits low fracture toughness ($\sim 3 \text{ MPa}\cdot\text{m}^{1/2}$) [7, 87, 88]. This behavior is common to many intermetallics, which typically have: (1) strong atomic bonding; (2) ordered atomic arrangements and large unit cells; and (3) low-symmetry crystal structures [27]. These factors combine to greatly increase the difficulty of plastic deformation; the first two result in increased energy and complexity of dislocations (broad cores), reducing their generation and subsequent mobility. Along with bond strength, high

bond directionality is also associated with brittleness; using a valence-force-field approach, it was recently determined that the bond directionality in the C11_b (MoSi₂) structure was stronger than in either the C40 (CrSi₂) or C54 (TiSi₂) structures [89]. Low crystal symmetry generally results in the number of operative slip systems being insufficient to satisfy the von Mises criterion [20, 27, 86].

For MoSi₂, noticeable permanent deformation is possible only at temperatures (>1000°C) where thermal activation can increase dislocation density and mobility [27, 41] or produce apparent plastic deformation through time-dependent deformation mechanisms [90]. For powder processed silicides, it has been proposed that silica present in MoSi₂ (Figure 2.6) may have further adverse effects on RT fracture toughness and ductility, although by what mechanism is not clear [9].

Phase stability studies of MoSi₂ with additions such as Ta, Ti, Nb and Cr have indicated the possibility producing multi-phase silicides, although these materials did not show any improvement in fracture toughness over monolithic MoSi₂ [14, 91, 92]. Removal of silica through carbon additions provides some increase in toughness at high temperatures, but has shown little effect on ambient temperature properties [66]. Ductile reinforcements such as Nb [67-69], Ta [67] and W [68] in filament, particulate and wire result in modest toughness improvements. Although reinforcing of MoSi₂ with SiC, ZrO₂, or β Si₃N₄ has resulted in RT fracture toughness values as high as 8.5 MPa·m^{1/2} [3, 26, 48, 93] this is still well below the range of some aluminides (e.g., Ti₂ (Al, Nb) ~ 30 MPa·m^{1/2} [11]) and superalloys. Very limited information exists on the fatigue properties of MoSi₂-based materials, although as might be expected from its low toughness, fatigue crack growth rates increase rapidly with increasing stress intensity [6].

2.2.1.3 Elevated-temperature mechanical behavior

Monolithic MoSi₂ is generally regarded to exhibit three regimes of mechanical behavior: (1) strong and brittle below ~ 1000°C; (2) strong and ductile between ~1000 and ~1250°C; and (3) weak and ductile above ~ 1250°C [41]. The onset of regime (2) is

associated with the brittle-to-ductile transition temperature (BDTT), although there exists considerable dispute regarding the definition of the BDTT for MoSi_2 , and its reported value ranges from 950 to 1400°C [94]. Much of this confusion relates to the presence of silica in MoSi_2 as a result of powder processing and how its softening might influence definition of the BDTT [94] as well as lead to a decrease in the elevated-temperature strength and creep resistance of MoSi_2 [48].

For most single-crystal and coarser grain silicides ($\geq 20 \mu\text{m}$) tested at temperatures above 1000°C, stress exponents (n) of around 3 are observed, consistent with dislocation glide-controlled deformation [62]. Materials with finer grain sizes ($\sim 5 \mu\text{m}$) typically have n less than 2, which is often associated with a combination of viscous/diffusional flow and dislocation mechanisms; it is believed that the softening of glassy silica acts a lubricant to further enhance grain boundary sliding in the finer grain materials, whose fine scale already predisposes them to boundary-related mechanisms [6]. For example, the creep rate of a 20 μm grain size monolithic MoSi_2 is more than three orders of magnitudes lower than a 5 μm grain size material at 1200°C [6]. When the deformation behavior of fine grain silica-free and silica-containing materials of equivalent grain size was compared [63], the silica-free material did show higher n values than the silica-containing MoSi_2 , indicating the deleterious effects of the oxide on creep strength. However, both materials displayed similar trends of decreasing n with increasing temperature, while a 40 μm silica-free sample showed the opposite trend, indicating that grain size may actually be a more important factor than silica content in controlling the high temperature deformation of silicides. Temperature and strain rate effects on the compressive strength of a coarse ($\sim 40 \mu\text{m}$) grain, low-oxygen MoSi_2 sample are presented in Figure 2.7 (a).

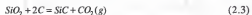
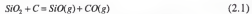
To further improve the elevated-temperature properties of MoSi_2 , a variety of reinforcing phases have been examined; viable reinforcements for high-temperature applications need to have desirable mechanical properties, as well as thermodynamic compatibility and minimal thermal expansion (CTE) mismatch with the matrix. Of potential

reinforcement materials, SiC has proven to be one of the most popular because of its thermodynamic compatibility with MoSi₂, its negligible effect on matrix oxidation and its availability in a wide range of forms [41, 48]. However, SiC does display a rather large CTE mismatch with MoSi₂ (see Table 2.2) resulting in thermal strains and matrix cracking [41] upon cooling. Even so, significant improvements in yield strength, particularly above 1300°C, have been reported with both particulate and whisker SiC reinforcements (Figure 2.7 (b)) [3, 77, 91].

Improvements in creep resistance over monolithic MoSi₂ have also been observed (Figure 4.8 (a)) with C additions to form SiC and remove silica, with dual mechanisms of composite strengthening and elimination of the viscous silica [48, 62]. However, as described above, the effects of silica on creep properties are still somewhat unclear, with some low-silica MoSi₂-based materials showing stress exponents close to unity, although usually at finer grain sizes [95]. Some of the highest creep resistance reported for MoSi₂-based materials is that of an *in situ* MoSi₂-SiC composite (Figure 4.8 (b)) containing only 5 Vol.% reinforcement, resultant from carbon addition just sufficient to reduce all silica; this small fraction of SiC still allows for sufficient grain growth during consolidation to obtain a 40 µm grain size, and it is this combination of low silica and large grain size which leads to the excellent creep strength of this material.

2.2.1.4 Carbon additions to MoSi₂

Since carbon additions to MoSi₂ are the most common route of silica removal and are also one common method for producing *in situ* composites of MoSi₂-SiC it is worthwhile to examine this method more closely. The concept of adding C to MoSi₂ was recognized early on [35, 96] as an effective way to reduce the siliceous grain boundary phase through reactions of the form [65]:



As an extension of carbon additions to MoSi_2 , it seems logical that the concept of solid state displacement reactions [71, 97] could be used to produce a SiC reinforcement phase using *in situ* methods. Compared with traditional composite processing schemes, *in situ* reactions can often be initiated at lower temperatures and the resultant materials have interfaces which are inherently stable thermodynamically [64, 97]. Using an exothermal-dispersion (XD™) technique, Aiken [76, 77] produced MoSi_2 +30 Vol.% SiC composites with equiaxed reinforcement morphology, reduced oxygen content compared with unreinforced MoSi_2 , and increased strength at high temperatures. Jayashankar [58, 63] used a combination of carbon additions, MA and a carbothermal reduction step to eliminate silica and produce SiC reinforcements. Microstructures in this work contained three phases—low-oxygen MoSi_2 , uniformly distributed SiC and the ternary phase $\text{Mo}_5\text{Si}_3\text{C}$, which contained iron presumably picked up from the steel milling media.

Another approach to producing *in situ* MoSi_2 +SiC composites was that of Henager and collaborators [12, 72] who hot pressed compacts of $\text{Mo}_2\text{C} + \text{Si}$ at 1350°C/1700°C and modeled their microstructural evolution from diffusion and interfacial reaction considerations. This *in situ* approach led to a fine-grain (1-2 μm) MoSi_2 matrix with ~30 Vol.% of sub-micron SiC and $\text{Mo}_5\text{Si}_3\text{C}$. As expected, an improvement in strength is seen for these MoSi_2 +SiC composites although the authors note that the lack of information on the mechanical properties of the $\text{Mo}_5\text{Si}_3\text{C}$ phase complicates analysis of the composite mechanical behavior.

2.2.2 $\text{Mo}_5\text{Si}_3\text{C}$ Compounds

Because of their relationship to the $\text{Mo}_5\text{Si}_3\text{C}$ compound which is the focus of this study, available information about the compounds Mo_5Si_3 and Ti_5Si_3 will now be reviewed. Having the nearest stoichiometry to $\text{Mo}_5\text{Si}_3\text{C}$ of the three binary silicides of molybdenum, Mo_5Si_3 has a tetragonal $\text{D}_{8h}(\text{I}32)$ crystal structure [98], a density of 8.24 g/cm^3 , and melts congruently at 2180°C. From the Mo-Si binary diagram [1], Mo_5Si_3 has a homogeneity range of 37 to 40 At.% Si at 1200°C.

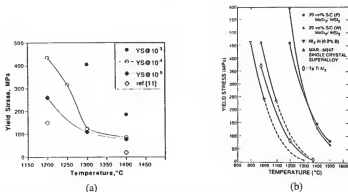


Figure 2.7 (a) Compressive flow behavior of high-purity, 40 μm grain size MoSi₂ [9]. (b) Bend strength versus temperature for two MoSi₂-based composites, along with other intermetallics and the single-crystal superalloy MAR M247 for comparison [3].

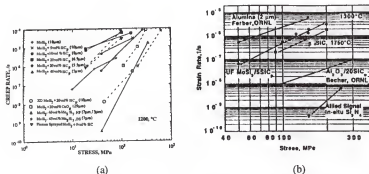


Figure 2.8 (a) Creep data for monolithic MoSi₂ and several MoSi₂ composites [95]. (b) Comparison plot showing creep data for several MoSi₂-SiC composites and values for ceramic-matrix composites [63].

Because of its reduced silicon activity, Mo_5Si_3 does not form a protective, adherent silica scale like MoSi_2 and as such has poor oxidation resistance; doping with less than 2 Wt.% boron seems to improve the oxidation resistance of Mo_5Si_3 , with the proposed mechanism being boron-aided viscous sintering to close porosity in the scale formed during intermediate temperature oxidation [99]. Little is known of the mechanical properties of Mo_5Si_3 , other than elastic constants of single-crystal material [100]; Mo_5Si_3 has been reported to show superior creep resistance [101] compared with MoSi_2 .

The Ti_3Si_3 compound melts at 2130°C , has a density of 4.32 g/cm^3 , and solidifies in the hexagonal D_{8h} (hP16) crystal structure. One reason given for the study of Ti_3Si_3 was to examine its oxidation resistance, expected to be controlled by a mixed silica-rutile scale; in fact, the reported oxidation behavior of Ti_3Si_3 was similar to titanium in that a transition from parabolic to linear oxidation kinetics occurs as the external TiO_2 scale spalls off. Doping with less than 3 Wt. % carbon considerably slowed the oxidation process, perhaps as a result of the formation of an underlying continuous silica scale [102]. In addition, because of the presence of a $\text{Ti-Ti}_3\text{Si}_3$ eutectic at 1350°C it is possible to produce directionally solidified eutectic composites capable of 3.5 % plastic strain in compression at room temperature without cracking [80].

A feature reported for both Mo_5Si_3 and Ti_3Si_3 is the presence of transgranular microcracks upon cooling from the processing temperature; for Mo_5Si_3 , samples in one study having average grain sizes greater than $15 \mu\text{m}$ exhibited microcracking [102], while a grain size-dependent microcrack density was also reported for hot pressed Ti_3Si_3 [103, 104]. The root cause of this thermally induced microcracking was in both cases proposed to be an anisotropy in coefficients of thermal expansion leading to microfracture upon cooling in accord with the models of Evans [105]. The critical facet size l_{co} for the onset of microfracture caused by CTE anisotropy, which is related to a critical grain diameter, is

$$I_{co} = \frac{5.2(1+\nu)^2 \gamma_{cb}}{(E)(\Delta\alpha\Delta T)^2} \quad (2.4)$$

showing a strong dependence on the degree of CTE anisotropy ($\Delta\alpha$) and temperature gradient (ΔT); alternatively, it can be shown that the stress intensity factor increases with increasing grain size for materials with anisotropic expansion coefficients [105].

Indeed, single crystal work on Mo_5Si_3 indicates a significant degree of thermal expansion anisotropy [100], $\alpha/\alpha_a \approx 2.2$. Based on this degree of CTE anisotropy in Mo_5Si_3 , tensile stresses near the grain boundaries as high as 1.8 GPa were predicted for the cooling of a polycrystalline material from the melting point. The hexagonal Ti_5Si_3 compound has a CTE anisotropy of $\alpha/\alpha_a \approx 2.3$ [104]; doping Ti_5Si_3 with 0.85 formula unit of carbon results in a reduction in the CTE anisotropy. In the case of undoped Ti_5Si_3 , CTE anisotropy has been predicted to cause thermally induced cracking at grain sizes greater than 4 μm [103].

2.3 Ternary Silicide Compounds

Compared to other areas of silicide development, information on alloying additions and associated ternary silicide phases is somewhat limited. Early efforts in this area were focused on development of M-Si-X ternary isotherms, such as the work of Nowotny [18, 106, 107], Brukl [108], and others [109, 110]. With the recent interest in silicide materials for possible structural applications, ternary isotherms were used in studies of alloying additions to MoSi_2 [91, 92], composite design [12, 58, 77, 97, 111-113], multiphase silicides [7, 14, 114-116], doping to improve oxidation resistance [101, 102], and synthesis of ternary silicide compounds and composites [10, 74, 112, 117-120].

One reason for investigating ternary silicide compounds is based on the premise that either their altered bonding arrangements or, in some cases, higher symmetry crystal structures may allow for improvement upon the poor RT ductility and toughness of binary silicides [74]. Macro-alloying has been used in A_3X intermetallic systems to stabilize

higher symmetry crystal structures with resultant improvements in RT ductility. For example, binary Co_3V is brittle at ambient temperatures and has a complex hexagonal (hP24) structure up to 1030°C , where it transforms to a ordered-fcc L1_2 (cP4) structure. By alloying with Fe, a $(\text{Co,Fe})_3\text{V}$ compound having the L1_2 structure can be stabilized to room temperature for iron concentrations in excess of about 11 At.% [121]. This increase in crystal symmetry results in the activation of more slip systems, which in turn leads to an increase in tensile ductility from 1% for Co_3V to 40% for $(\text{Co, Fe})_3\text{V}$ [11]. However, this sort of crystal symmetry change through compositional control does not always correspond to improvements in ductility, as is the case in Al_3X compounds where alloying additions can stabilize the L1_2 structure, yet these cubic compounds still have only minimal ductility, probably the result of a residual directionality in bonding limiting dislocation mobility and resulting in an intrinsically low resistance to fracture [27, 122, 123].

In the case of Mo-Si-X compounds (Figure 2.9), the potential clearly exists to synthesize cubic or hexagonal ternary silicide phases through macro-alloying. However, it is unclear what effects these transitions to higher symmetry might have on the mechanical properties of these compounds. Compared to the stabilized L1_2 compounds such as $(\text{Co,Fe})_3\text{V}$ that exhibit enhanced ductility, MoSi_2 and other silicide compounds have in general more covalent (Si-Si, Mo-Si) atomic bonding [33], and larger, more complex unit cells. These factors make it less likely that alloying of silicides to increase their symmetry can induce significant improvements in RT mechanical properties, although preliminary studies and modeling efforts have touted the “disembrittlement” of MoSi_2 through micro-alloying [124] and the more “metallic” nature of some ternary silicides [75]. In addition to possible ductility improvements, it has been speculated that ternary silicide compounds may exhibit other interesting properties, either alone or in equilibrium with a metallic solid solution [7, 114].

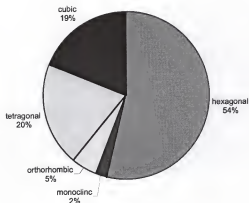


Figure 2.9 Distribution of crystal structure classes for 64 known Mo-Si-X ternary compounds (X=Al, B, C, Co, Cr, Er, Fe, Hf, Nb, Ni, Re, Ta, Ti, U, V, W, Zr) [125].

2.3.1 Mo-Si-Al System

The Mo-Si-Al system has been studied for the purposes of determining phase equilibria [106, 108], possible MoSi₂ deoxidation routes [126], and synthesis of the substitutional Mo(Si, Al)₂ (C40) compound [127]. Because of conflicting Mo-Si-Al isotherms and obvious inaccuracies, a revised 1400°C isotherm has been created [128] (Figure 2.10).

It has been proposed that the hexagonal crystal structure of the C40 compound could lead to RT ductility improvements [10]; however, recent single crystal work [129] indicates that the compound has high critical resolved shear stresses for all slip systems and no additional deformation mechanisms compared with MoSi₂. Another area of study with regard to the C40 compound was the potential for improved high-temperature oxidation

resistance due to a mixed alumina-silica oxide scale; results in this area have been mixed [130, 131] and it has recently been discovered that carbon contamination during powder processing can lead to degradation of the C40 compound at room temperature [39].

2.3.2 Mo-Si-B System

Because boron has been shown to enhance the oxidation resistance of Mo-rich Mo-Si alloys, the Mo-Si-B system has been investigated for its phase equilibria [116, 132, 133], its oxidation resistance as a function of composition [99], the possible production of *in situ* composites [77, 127], and the microstructural evolution of Mo-T2 alloys [114], where T2 is the Mo_5SiB_2 compound shown in Figure 2.11.

A rather unique feature of this system is the equilibrium between the molybdenum solid solution and the ternary silicide phase (T2). In theory, this should make possible the synthesis of alloys having a continuous ductile matrix (Mo) with the silicide phase(s) hopefully lending increased oxidation resistance. However, as with other refractory metal-silicide alloys [79], achieving microstructural optimization is not trivial [114].

2.3.3 Mo-Si-C System and the $\text{Mo}_5\text{Si}_2\text{C}$ Phase

As previously discussed, the Mo-Si-C system is of interest from the standpoint of removing silica from MoSi_2 by carbon additions and producing MoSi_2 -SiC composites through displacement reactions.

2.3.3.1 Thermodynamics of the Mo-Si-C system

Initial work in the Mo-Si-C system was performed by Nowotny and coworkers [18], who generated a 1600°C isotherm (Figure 2.12) for the system. This isotherm has several important features: equilibrium between SiC, MoSi_2 , and $\text{Mo}_5\text{Si}_2\text{C}$ (T); the presence of Mo_5Si_2 , which is now recognized to be Mo_5Si_3 , and MoC, which is not stable at 1600°C according to the currently accepted Mo-C binary diagram [134]; and a range of single-phase stability for $\text{Mo}_5\text{Si}_2\text{C}$ spanning Mo:Si ratios of approximately 1.2 to 2.0 and carbon contents ranging from 6 to 15 At.%. The authors justified this broad compositional range on the basis of variable filling of the atom sites for molybdenum and carbon [18].

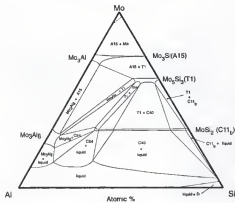


Figure 2.10 Revised Mo-Si-Al 1400°C isotherm [128].

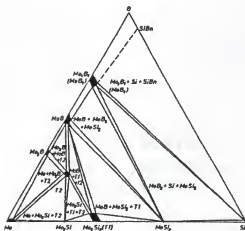


Figure 2.11 Proposed isotherm for Mo-Si-B system at 1600°C. Note the T1(Mo₃(Si,B)₃) and T2 (Mo₃SiB₃) phases [132].

The following formula was proposed for the compositional range of the $\text{Mo}_{25}\text{Si}_3\text{C}_{21}$ phase (so designated to indicate its variable composition),

$$\text{Mo}_6(\text{Si}_x, \text{Mo}_{1-x})_4(\text{C}_y, \text{Si}_{1-y})_6 \quad (2.5)$$

where x varies from 0.1 to 0.55 and y varies from 0.15 to 0.4. The authors also noted variations in axial c/a ratio from 0.695 for Mo-rich compositions to 0.687 for Mo-lean compositions in this study, which was interpreted as indicating a broad range of homogeneity for the ternary phase.

Renewed interest in the Mo-Si-C system for carbothermal deoxidation and production of *in situ* MoSi_2 composites in the late 1980s drew attention to the aforementioned phase equilibria of Nowotny as well as the more recent work of van Loo [19] and others [135]. Using XRD and electron microprobe (EPMA) analysis of arc melted specimens and diffusion couples, van Loo and coworkers proposed a 1200°C isotherm (Figure 2.13) of the Mo-Si-C system.

Two principal differences exist between the Nowotny and van Loo isotherms: (1) van Loo shows MoSi_2 and SiC in equilibrium with Mo_5Si_3 , *not* $\text{Mo}_5\text{Si}_3\text{C}$ and (2) the region of $\text{Mo}_5\text{Si}_3\text{C}$ single-phase stability is significantly reduced on the van Loo isotherm. Issue (1) was addressed by Costa e Silva and Kaufman [136], and it was shown through thermodynamic calculations and systematic experimental investigation of phase relations, that $\text{Mo}_5\text{Si}_3\text{C}$ is in equilibrium with MoSi_2 and SiC at both 1600°C and 1200°C, i.e., the form of the Mo-Si-C isotherm as given by Nowotny (Figure 2.12) is correct. However, recent work [12, 120] has tended to support the conclusion of a significantly smaller homogeneity range for $\text{Mo}_5\text{Si}_3\text{C}$ than that reported by Nowotny. A similarly reduced compositional range was recently reported for the T1 phase in the Mo-Si-B system (Figure 2.11) [115]. The original Mo-Si-C phase equilibria study also yielded a liquidus projection for the Mo-Si-C system (Figure 2.14), indicating a melting point for the ternary phase above 2000°C.

2.3.3.2 Atomic arrangement and crystal structure of $\text{Mo}_5\text{Si}_3\text{C}$

The structure of the $\text{Mo}_5\text{Si}_3\text{C}$ phase was investigated in detail by Parthe and collaborators [137] using neutron diffraction. It was determined previously that the ternary phase had an Mn_5Si_3 -type (hP16 , D8_9) hexagonal crystal structure, but at the time, there was still question as to how the carbon atoms were arranged in the lattice. Four possible structure proposals for $\text{Mo}_5\text{Si}_3\text{C}$ were outlined by Parthe:

1. Partial occupation of silicon $6(g_{II})$ positions by carbon atoms with Si atoms occupying former Mo positions $4(d)$;
2. Carbon atoms substituting on former Mo positions;
3. Carbon completely occupying octahedral interstitial sites $(0,0,0)$ and $(0,0,1/2)$;
4. Octahedral sites filled variably by C atoms and variable occupancy of $4(d)$ positions with Mo atoms.

By examining x-ray diffraction (XRD) and neutron diffraction data, Parthe determined that proposal (4) is correct and can account for the broad range of homogeneity of $\text{Mo}_5\text{Si}_3\text{C}$ reported by Nowotny [18]. The corresponding structure (Figure 2.15) has the $P6_3/mcm$ space group with 6 Mo atoms in $6(g_{II})$ sites with $x=0.24$, 3.6 Mo atoms in $4(d)$ sites, 6 Si atoms in $6(g_{II})$ with $x=0.6$, and 1.2 carbon atoms in the $2(b)$ sites. The values for the lattice parameters a and c are 0.728 nm and 0.505 nm, respectively [137].

2.3.3.3 Processing, microstructures and properties of $\text{Mo}_5\text{Si}_3\text{C}$

Despite the relatively large number of studies concerning the Mo-Si-C system, only three studies (excluding the current work) were found directly applicable to the processing and properties of $\text{Mo}_5\text{Si}_3\text{C}$ -based materials. The first is the original phase diagram study of Nowotny et al. [18], for which materials were hot pressed from elemental Mo, Si, and C powders followed by heat treatment for 12 h at 1600°C. The only microstructure presented in the study is shown in Figure 2.16; it is difficult to discern much from this micrograph, although the sample is quite porous and appears to have features or phases near several grain boundary triple points. In this study, density and Vickers microhardness values of 8.0 g/cm³ and 14.3 GPa (50g load), respectively, were reported for $\text{Mo}_5\text{Si}_3\text{C}$.

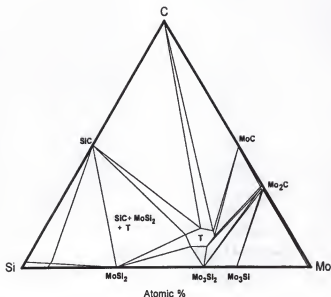


Figure 2.12 Accepted 1600°C Mo-Si-C isotherm at [18]. The ternary silicide $\text{Mo}_3\text{Si}_3\text{C}$ is designated by T, and is shown to be in equilibrium with SiC and MoSi, at this temperature. Note what is now accepted to be Mo_3Si_3 is labeled " Mo_3Si_3 ," and the presence of MoC, in contrast to the now accepted decomposition of MoC into Mo_3C above 1600°C [134].

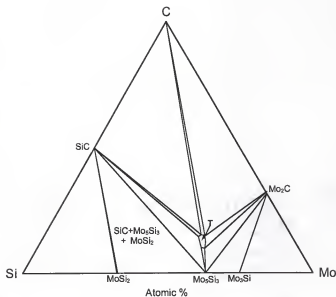


Figure 2.13 Isotherm of Mo-Si-C system at 1200°C [19]. Note the existence of a three phase equilibrium between MoSi_2 , SiC, and Mo_5Si_3 , along with the significantly smaller $\text{Mo}_5\text{Si}_3\text{C}$ single phase field.

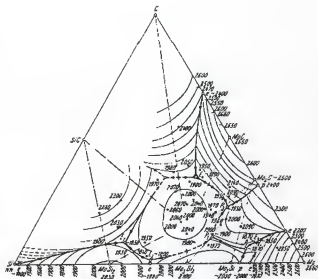


Figure 2.14 Liquidus projection for the Mo-Si-C system [18].

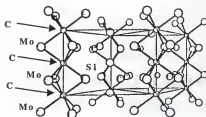


Figure 2.15 Schematic of the $D8_h$ crystal structure of Mo_6Si_3C , showing carbon atoms occupying the octahedral interstitial sites of Mo in $6(g)$ [137].

Quite recently, Suzuki and Niihara [120] investigated $\text{Mo}_5\text{Si}_3\text{C}$ -based compounds as potential high temperature structural materials. Starting with Mo, Si, and C powders (all $< 10\ \mu\text{m}$) wet ball-milled in acetone for 48 h followed by hot pressing at 1500°C using 30 MPa pressure, samples were produced at a nominal composition corresponding to $\text{Mo}_{56.1}\text{Si}_{36.9}\text{C}_{7.0}$. The authors report single phase materials at this composition on the basis of XRD and SEM characterization, although their "single phase" structures (Figure 2.17) contain roughly 4 Vol. % of what is claimed to be SiO_2 . This is somewhat puzzling based on the amount of carbon (1.3 Wt. %) which should be more than sufficient to reduce any silica present on the powders through reactions like those shown in Equations 2.1-2.3. A possible explanation is that the fine starting powders had increased oxygen content owing to their high surface area, and the amount of carbon added was insufficient to fully reduce the silica present. In fact, the authors report a slight carbon *gain* during hot pressing, again inconsistent with the operation of most silica reduction mechanisms. For nearly-single phase $\text{Mo}_5\text{Si}_3\text{C}$ materials, the authors report an average density of $7.58\ \text{g/cm}^3$

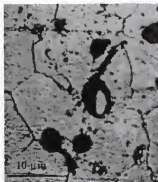


Figure 2.16 Microstructure of ternary $\text{Mo}_5\text{Si}_3\text{C}$ phase from Nowotny et al. [18]. The sample has been etched, explaining the rough surface. The authors report the black regions to be sintering porosity.

(theoretical density $\sim 7.9 \text{ g/cm}^3$), average RT 3-point bend strength of 430 MPa, a Vickers hardness of 12.1 GPa, and a fracture toughness of $3.4 \text{ MPa}\cdot\text{m}^{1/2}$.



Figure 2.17 Scanning electron micrograph of a $\text{Mo}_5\text{Si}_3\text{C}$ sample hot pressed for 2 h at 1500°C . Dark globular regions are reported to be silica [120].

A final study was that of Thom and coworkers [102] who explored the possibility of doping Mo_5Si_3 with B and C, primarily to improve oxidation resistance; they noted carbon additions did not have any beneficial effects on oxidation properties, as a sample with nominal composition $\text{Mo}_5\text{Si}_3\text{C}_{0.1}$ underwent rapid MoO_3 volatilization and weight loss in air at 1000°C . For samples HIP consolidated to $\sim 80\%$ density, Vickers hardness values increased with carbon content up to a maximum of 12.8 GPa for one formula unit of carbon (i.e., the idealized $\text{Mo}_5\text{Si}_3\text{C}$ composition).

CHAPTER 3 PROCESSING AND COMPOSITIONAL RANGE ISSUES

3.1 Introduction

The primary goal of the processing optimization portion of this study was to determine what combination of processing method and composition yielded the best material with respect to such features as single-phase microstructure, sample homogeneity, gas and sintering porosity, macro- and microcracking, and oxide inclusions. These microstructural features were deemed important based primarily on their potential effect on the mechanical properties and deformation behavior of $\text{Mo}_5\text{Si}_3\text{C}$ -based materials. Potential processing schemes were also assessed on the basis of their repeatability, ease of scale-up, and relative complexity. In order to investigate the effects of grain size on the mechanical behavior of $\text{Mo}_5\text{Si}_3\text{C}$, it was also necessary to determine which processing routes allowed for adequate control of the scale of the microstructure. Because of the previously mentioned uncertainty regarding the compositional range of $\text{Mo}_5\text{Si}_3\text{C}$, it was also of interest to re-examine phase stability and equilibria issues in the near- $\text{Mo}_5\text{Si}_3\text{C}$ region of the Mo-Si-C system.

3.2 Materials and Experimental Procedures

3.2.1 Raw Materials

Choice of raw materials form, size, and purity (Table 3.1) varied with processing route and were limited in most cases to those which were produced commercially. When commercially-produced materials were used, every attempt was made to obtain information from the vendor as to the impurity content and type, particle size and size distribution, and

lot number so that the effect of starting materials as a process variable could be properly assessed.

Table 3.1 Raw materials used in the production of $\text{Mo}_5\text{Si}_3\text{C}$ -containing samples.

Material	Form	Purity (%)	Size	Source	Lot Number
Carbon (graphite)	pieces	99.9	2-3 mm	POCO Graphite, Inc.	-
Molybdenum	rod	99.95	3 mm	Alfa AESAR®	H23E06
Silicon	lump	99.9999	2-10 mm	Alfa AESAR®	19294
Carbon (graphite)	powder	99	<50 μm	Alfa AESAR®	GO7E05
Molybdenum	powder	99.9	45-100 μm	Cerac®	X17221
Molybdenum	powder	99.9	<45 μm	Cerac®	X11672
Molybdenum	powder	99.7	3-7 μm	Alfa AESAR®	D27B25
Silicon	powder	99.999	45-150 μm	Cerac®	125889-C-1W
Silicon	powder	99.9999	63-75 μm	Alfa AESAR®	20728
Silicon	powder	99.999	<45 μm	Alfa AESAR®	B20G04
Mo_2C	powder	99+	-	Cerac®	19913
Mo_2C	powder	99.5	<45 μm	Cerac®	117807-A-1-2
MoSi_2	powder	99.995	<150 μm	Cerac®	X16146-1
Mo_5Si_3	powder	99.5	5.4 μm	Cerac®	133457-A-1
Mo_5Si_3	powder	99.5	<45 μm	Cerac®	142793-A-(1-4)
Mo_5Si_3	powder	99.5	<45 μm	Cerac®	153888-A-(1-3)

3.2.2 Processing Routes

Based on previous work in our laboratories [13, 58, 64, 126] and others [48, 70, 103], the following processing routes were thought to have the most potential for the reproducible production of $\text{Mo}_5\text{Si}_3\text{C}$ -containing samples: (1) non-consumable arc melting; (2) mixing of powders followed by hot consolidation; and (3) mechanical alloying of elemental and/or compound powders followed by hot consolidation.

3.2.2.1 Arc melting

Arc melting was done with a non-consumable thoriated tungsten electrode in a Centorr model 5 Bell Jar arc melting furnace powered by a Miller® Gold Star™ SS 400 DC welding power source. At the beginning of each melting session, the chamber and water-cooled copper hearth were thoroughly cleaned and 25 g of melt stock consisting of molybdenum rod, silicon chunks, and graphite pieces were arranged in the melting receptacles within the bell jar. Before melting, the Mo pieces were ground with 400 grit SiC paper to remove any oxide present on the surface. The bell jar was evacuated to 13.3 Pa followed by back-filling to ~50 kPa with ultra high purity argon (< 0.5 ppm total hydrocarbons); this procedure was repeated a minimum of three times to ensure a clean melting environment. In order to scavenge any remaining oxygen, titanium getter buttons were melted just prior to applying the arc to the melt stock. The arc power was controlled using a foot pedal with typical currents on the order of 250 A.

In order to enhance the amount of carbon going into solution while reducing the potential for silicon losses through vaporization, melting was done in two stages, wherein the molybdenum rod and graphite pieces were melted separately and then brought into contact with the silicon chunks and re-melted, drawing in the silicon as it melted. In both melting steps, samples were melted and flipped over a minimum of five times to enhance homogenization; whenever necessary between melting runs, the chamber was opened and cleaned with a rotary wire brush and rinsed with acetone. In order to quantify weight losses during arc melting, samples were weighed before and after each melting step.

3.2.2.2 Powder mixing and hot pressing

The majority of the samples in this study were processed by blending commercially available powders followed by hot pressing. For this processing method, various combinations of (Table 3.1) molybdenum, Mo_2C , Mo_5Si_3 , silicon, and carbon powders were measured out and then blended for 2 h on a tumbler ball mill. Ball milling was conducted in 250 mL polyethylene vials with ZrO_2 milling media at a 3.5:1 (by weight)

ball-to-milling charge ratio. After ball milling, the powders were loaded into high-density POCO HPD-1 graphite tooling (Figure 3.1) consisting of three parts: (1) a cylindrical die with an inner cavity; (2) a top punch to which is loaded by the hydraulic actuator on the hot press; and (3) a shorter bottom punch which holds the powders inside the die. For the processing study and phase stability portion of this work, graphite dies having an inner diameter of 16 mm (5/8") were used, while larger, 32 mm (1.25") inner diameter dies were used for synthesis of samples for mechanical testing. In all cases, the die surfaces were coated with hexagonal boron nitride spray to provide lubrication at processing temperatures and to aid in removal of the consolidated specimens. As an additional aid in the removal of consolidated samples and to minimize sticking of the powders to the die and ram surfaces, 0.13 mm thick GRAFOIL® flexible graphite paper was used to line the die inside diameter as well as the top and bottom punch/powder contact surfaces.

After preparation and charging of the graphite die with the blended powders (~10 g for the smaller dies, ~45 g for the larger dies), the assembly was placed inside a Centorr Model 600 vacuum hot press (Figure 3.2), which was used to consolidate all powder-processed samples in this study. The Model 600 allows for application of uniaxial pressure through a hydraulic actuator and ram in a vacuum (less than 0.13 Pa) or inert gas atmosphere. Heating inside the water-cooled stainless steel chamber was accomplished by induction heating coils powered by a 15 kW TEK Specialties, Inc. MG-15 induction power supply capable of sustaining temperatures in excess of 1700°C for the setup used. A quartz susceptor lined with graphite felt insulation surrounded the die and punch assembly, a graphite spacer block, and two 1.3 cm thick squares of refractory brick, stacked in the order shown in Figure 3.1. A two-color Capintec Ratio-Scope® 8 optical pyrometer was used for temperature monitoring in the hot press; when focused through a viewport in the chamber, the pyrometer measures the temperature at the surface of the graphite die with an accuracy of approximately $\pm 20^{\circ}\text{C}$ over its operating range (650°C to 2200°C).

Variations on a two-stage HP approach (Figure 3.3) were used to produce blended powder samples, with an initial hold under vacuum at temperatures ranging from 1350 to 1500°C followed by a densification step under argon at 1650°C or 1700°C. In some cases, uniaxial pressure was applied to the sample during the initial heating and low-temperature hold cycle (pre-load). Typical heating rates were on the order of 50°C/min, while cooling rates ranged from 16 to 25 °C/min. After densification, pressure was removed and the sample cooled either by reducing the power completely and allowing the sample to furnace cool, or by ramping down the power on the hot press incrementally for 1 h followed by furnace cooling. For all hot press runs, data on temperature and pressure were recorded at prescribed intervals; several actual processing profiles are presented in Appendix A. After cooling and removal of the sample from the die using a mounting press, the sample dimensions and weight were recorded and approximately 1 mm was ground off of each surface to remove the adhered graphite foil and any reaction zone.

For heat treatment of the consolidated samples, a Centorr model M60 with Ta heating elements was used. Heat treatment was for 12 h at 1600°C under high-purity argon followed by furnace cooling at approximately 15 °C/min.

3.2.2.3 Mechanical alloying + hot pressing

The starting powders for mechanical alloying (MA) consisted of molybdenum or Mo_3Si_3 mixed with silicon and carbon. Initially, the powders were blended in polyethylene bottles on a tumbler ball mill using ZrO_2 milling media at a ball-to-charge ratio of 3.5:1 by weight. After blending for approximately 1 h, the powder charge was weighed and placed in a glass vial; the glass vial and a hardened steel grinding vial containing 0.6 cm diameter hardened steel balls were then placed in a glove bag. The glove bag was flushed with argon several times before final inflation and sealing, at which point the powders were transferred to the grinding vial. After tightly sealing the grinding vial, it was removed from the glove bag and placed on a SPEX 8000 Mixer/Mill where it was milled for 15 to 18 h.

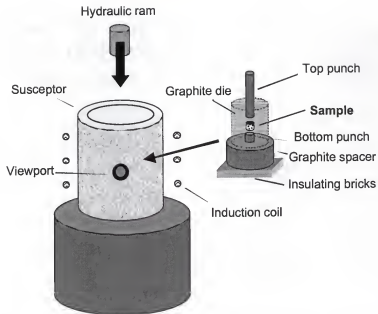


Figure 3.1 Schematic of setup for hot pressing of $\text{Mo}_5\text{Si}_3\text{C}$ -based materials. The die and punch assembly diagrammed on the right side of the figure was placed within the quartz susceptor and surrounded by graphite felt insulation.

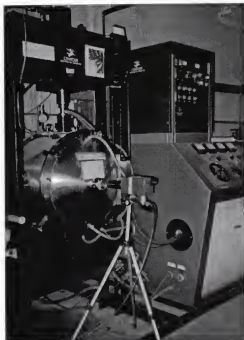


Figure 3.2 Centorr Model 600 uniaxial vacuum hot press with Captintec Ratio-Scope® 8 two-color pyrometer.

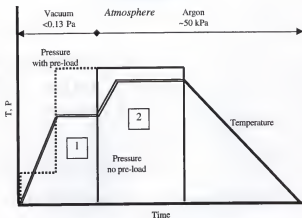


Figure 3.3 Schematic representation of the two-step hot pressing process showing heating and hold stage under vacuum (1) and the high-temperature consolidation step under argon (2). Also indicated are two possible pressure application routes, with or without pre-load.

Powder loadings varied from 10 to 25 g at a constant 2:1 weight ratio of grinding media to charge. For several milling runs, 0.5 g stearic acid ($C_{18}H_{36}O_2$) was added to the milling charge and a mixture of stearic acid and methanol was used to coat the milling vial and balls to minimize powder caking and agglomeration. After milling, the powders were removed from the milling vial and placed back on the tumbler ball mill for several hours to break up any large agglomerates which may have formed during the MA process.

After ball milling and MA, the powders were loaded into graphite dies and hot pressed in a manner similar to that already described. For the MA samples, two different hot pressing (HP) schemes were employed, a single-stage process and a two-stage process. In the first process, samples were pressed at 1400°C for 1 h at a uniaxial pressure of 47 MPa in a vacuum of less than 0.13 Pa. Samples processed using the two-stage method were initially held at 1500°C for 0.5 h without applied pressure in vacuum,

followed by a densification step of 1 h at 1650°C under 47 MPa pressure in an argon overpressure of roughly 50 kPa.

3.2.3 Materials Characterization and Analysis

To examine the effects of process variables and target compositions on sample microstructures and to assess the effectiveness of various processing routes, both starting materials and consolidated samples were subjected to a number of standard materials characterization and analysis techniques.

3.2.3.1 Physical properties

In order to verify the stated powder size and distribution of commercially obtained starting powders and also to examine the effects of various mixing and milling techniques on powder size, particle size analysis (PSA) was performed. In preparation for PSA, approximately 1g of powder was mixed in a water suspension and stored in a 50 mL polyethylene bottle. The powder suspension was loaded into a receptacle filled with de-ionized water in a Coulter LS 230 Particle Size Analyzer which uses a laser-optical measurement system to measure particle size. To reduce the potential for agglomeration, powders were also analyzed after addition of a Trinton X-100 wetting agent.

For both arc melted and hot pressed specimens, weight changes during processing were monitored to aid in the evaluation of processing techniques and parameters. The solid pieces comprising the raw materials of arc-melted samples were weighed out using a Denver Instrument Co. S-110 electronic balance having a resolution of 1 mg; the weight of the arc melted button after final melting was recorded after cleaning with acetone and drying. In some cases, arc melted buttons were weighed in between melting stages as well. The weight of powders charged into dies for hot pressing was recorded prior to pressing and compared with the weight of consolidated samples. Sticking of powder to the graphite dies and reaction of samples with the graphite foil liner complicated accurate determination of post-HP weight; typically a sample was measured as removed from the die

and again after grinding off the residual graphite foil, giving a range of high and low consolidated sample weights.

To estimate the degree of densification in powder-processed samples, the apparent density was measured by a method derived from ASTM Designation C 134-95 [138]. After sectioning a small cube of material from the center of the sample using a Buehler® Isomet diamond saw with a Buehler® low-concentration diamond wafering blade, the cube was ultrasonically cleaned in acetone and dried. The mass of the dry sample was measured on the electronic balance and recorded. Using an INOX digital caliper having 10 µm resolution, the length, width and height of the sample were measured a minimum of five times. Using the appropriate geometrical relations, the volume of the cube was determined. Knowing the mass and the volume of the specimen, an apparent bulk density (ρ) was determined using the following:

$$\rho = m/V \quad (3.1)$$

where m is the mass of the sample in g and V is the volume of the sample in cm^3 .

3.2.3.2 Microstructural analysis

Metallographic preparation. Prior to examination of sample microstructures, specimens were prepared using standard metallographic techniques. After sectioning of the sample using a diamond saw, the specimen was mounted in 2.54 cm diameter mounts of either quick-setting epoxy or a phenolic resin. The mounted sample was then wet ground to a flat, smooth surface using a rotating grinding wheel and a series of silicon carbide grinding papers (180 to 800 grit). Any remaining scratches were removed by diamond polishing on Buehler® TEXMET® polishing cloths with 6 µm and 1 µm water-based diamond slurry. As a final polishing step and to accentuate any phase relief in the samples, samples were mounted into holders and polished for 20 minutes on a Buehler® Vibromet® 2 vibratory polisher using napless nylon cloth and a 0.2 µm silica suspension. After grinding and polishing, samples were ultrasonically cleaned in a mixture of water and ultrasonic cleaning solution, rinsed with methanol, and dried using a hot air blower.

Light optical microscopy. Initial examination of microstructural features such as porosity, secondary phases, cracking, and grain size was conducted using a Nikon Epiphot® inverted metallograph equipped with a high-intensity light source and a Polaroid® film back. The metallograph has four magnifying lenses coupled with a 10x objective and is capable of 50 to 1000x magnification; filters and polarizers including differential interference contrast and Nomarski diffraction enhance the available imaging options. Light optical microscopy (LOM) was also used to check for scratches, beveling, discoloration, and other undesirable metallographic artifacts. The optically anisotropic hexagonal $\text{Mo}_5\text{Si}_3\text{C}$ phase displayed enhanced grain contrast without etching, simplifying determination of the mean grain diameter.

Scanning electron microscopy. For more detailed microstructural examination, scanning electron microscopy (SEM) was performed on polished specimens using JEOL 35CF, JEOL 6400, and JEOL 733 electron microscopes. Strips of conductive carbon paint were painted on specimens prior to insertion into the microscope to minimize charging effects. At a typical accelerating voltage of 12 kV, both secondary electron and backscattered electron images at both low and high magnification were recorded with a Polaroid® film back.

Quantitative image analysis. Images of sample microstructures collected from LOM and SEM were analyzed for quantitative information on three primary microstructural features of interest: (1) phase volume fraction; (2) volume fraction of porosity; and (3) determination of grain size. The first step in the image analysis procedure was digital capture of the images using a flatbed scanner followed by manipulation and enhancement of images in Adobe Photoshop™. The digitally enhanced image in PICT format was then transferred to NIH Image Ver. 1.61 image analysis software (distributed as freeware); NIH Image is capable of performing automated areal analysis for determination of phase and porosity volume fraction and aids in the calculation of average grain size using linear intercept methods.

For areal analysis in NIH Image, the feature of interest is converted to pure black against a white background by making the image binary. Next, the scale is set based upon the micron bar imprinted on the SEM image, or in the case of LOM images, a Vickers microhardness indent of known size was used to calibrate the scale. The area of interest was then measured, followed by analysis of total phase/particle area; dividing the area of particles/phase by the total measurement area yields the area fraction which correlates to the volume percent of a particular feature. This measurement process was repeated at least five times per image and a minimum of five images were used per sample to obtain average phase and porosity volume fractions.

To determine mean grain size, NIH Image was used with a line intercept method similar to that described in ASTM E 112-85 [139]. Using a minimum of five 50 mm test lines per region of interest, converted to the proper scale using the previously described methods, an average number of grain intercepts per test line length was determined from which the average grain diameter was derived. Although grain size analysis was carried out on both SEM and LOM images, the latter was preferred due to the better grain contrast achieved through the use of a polarizing filter in the optical microscope.

3.2.3.3 Phase identification and compositional analysis

X-Ray diffraction. For obtaining crystallographic information and phase identification (phase ID), x-ray data was collected using a Phillips APD 3720 x-ray diffraction (XRD) system. Samples for XRD were either in powder form, as pre-processed powders or comminuted consolidated specimens, or solid 1 cm x 1 cm x 1 mm thick slices from consolidated samples. Powder XRD samples were prepared by mounting <75 μm powders to an x-ray slide with double-sided tape or a suspension of amyl-acetate colloidian. Solid specimens were sectioned from bulk samples with a diamond saw and affixed to x-ray slides using crystal mounting adhesive or double-sided tape; to maintain proper spatial orientation with respect to the x-ray source and detector, a dummy of the same height as the solid sample was made from microscope cover slides and tape and

affixed to the x-ray slide. Using a Cu K α x-ray source at a wavelength of 0.154056 nm, data was collected from 10 to 100° 2 θ at 3° 2 θ /min with an intensity range of 1000 counts/sec full-scale.

After filtering the raw x-ray spectra to obtain the peaks present in the sample, the data were analyzed to determine the phases present and the lattice parameters of the Mo₅Si₃C phase. For phase identification, a standard method [140] was used, comparing interplanar spacings (d-spacings) and relative peak intensities in the x-ray data with d-spacing and intensity information taken from the JCPDS (Joint Committee on Powder Diffraction Standards) database on phases likely to be present in the sample. A positive phase ID for a given peak was arbitrarily defined to be a difference in d-spacings between experimental data and JCPDS file of ~0.0005 nm for large d values and ~0.0002 nm for smaller d-spacings; a reasonable correlation between expected and observed relative intensities was also deemed necessary for a good match. A slightly modified procedure was used for identification of Mo₅Si₃C because of uncertainties in the published x-ray data resulting from its variable composition; observed x-ray peaks were compared with a combination of JCPDS powder diffraction files 8-429 (deleted) and 43-1199, the data of Parthe et al. [137], and simulated diffraction data obtained from Virtual Laboratories Desktop Microscopist software application. Typically the eight highest intensity peaks were identified first to determine major phase constituent(s) followed by identification of successively less-intense peaks.

Lattice parameter determination for the Mo₅Si₃C phase was done by a simplified regression technique using the relationship between lattice parameters (a , c), d-spacing (d), and planar indices (hkl) for hexagonal crystals,

$$d = \frac{1}{\sqrt{\frac{4}{3} \left(\frac{h^2 + hk + k^2}{a^2} \right) + \frac{l^2}{c^2}}} \quad (3.2)$$

Using the observed interplanar spacings (d_{obs}) for ($hk0$) and ($00l$) planes, baseline values were determined for a and c , respectively. For the remaining (hkl), a and c values were calculated by inserting the baseline a and c values (from ($hk0$) and ($00l$) peaks) into Eq. 3.2 and varying these values incrementally until the calculated d-spacing matched d_{obs} for the given plane within ± 0.0001 nm.

Wavelength-dispersive spectrometry. Compositional information and phase ID using wavelength-dispersive spectrometry (WDS) was done on a JEOL 733 electron probe x-ray microanalyzer (EPMA) operating at an accelerating voltage of 12 kV with a spatial x-ray resolution of $\sim 1 \mu\text{m}$. Standards for elements of interest (Table 3.2) were used to set up an automated quantitative analysis routine and their calibration was re-checked at the outset of each EPMA session. After generation of x-ray spectra from a given sample, a PROZA quantitative correction algorithm was run to obtain compositional information in atomic and weight percent. For a given region on a polished sample, the typical procedure was to record x-ray spectra from a minimum of three distinct points per phase present; by spreading the electron beam to $50 \mu\text{m}$, information on bulk composition was obtained. In addition to electron probe microanalysis, x-ray dot maps were generated by selecting the appropriate channel on the image selector corresponding to the spectrometer crystal positioned appropriately for the element of interest.

Table 3.2 Elements measured and standards used for WDS analysis in the EPMA.

Element	X-Ray Spectra	Emission Energy (keV)	Standard
Mo	L α	2.52	molybdenum
Si	K α	1.838	silicon
C	K α	0.283	SiC
O	K α	0.531	quartz
Fe	K α	7.112	iron

Light element analysis. Measurements of minor amounts of elements with $Z < 10$ using WDS is characterized by low characteristic x-ray intensities, low peak-to-background ratios, interference from heavier elements, peak shifting, and surface contamination. These factors contribute to a minimum detection limit of 0.1 to 1 Wt.% for elements with $Z < 10$ [141]. Because of this, combustion-based light element analysis was performed at LECO[®] Technical Services Laboratory (St. Joseph, MI 49085) on several hot pressed samples for more accurate determination of bulk carbon, oxygen, and nitrogen contents. Carbon measurements were done on a LECO[®] CS-444 instrument in which ~ 1g specimens are ignited by an induction furnace and the combustion stream is analyzed by infrared (IR) absorption. A LECO[®] TC-436 nitrogen/oxygen determinator was used for measuring nitrogen and oxygen contents; solid (~2 g) samples were combusted by inert gas fusion with nitrogen measured by a thermal conductivity cell and oxygen detected through an IR absorption cell.

Transmission electron microscopy. Transmission electron microscopy (TEM) was performed on as hot-pressed samples as well as specimens having undergone high-temperature compressive deformation. Analysis was conducted on thin foils in JEOL 200CX and Phillips 420 transmission electron microscopes, operating at 200 kV and 120 kV, respectively. Samples for TEM were initially prepared by sectioning ~400 μm thick slices from 3 mm diameter cylinders using a low-speed diamond saw. Two to three slices were then mounted with crystal mounting wax to a mounting peg and placed in an adjustable-height Gatan disc grinder; samples were ground through a series of SiC grinding papers from 400 to 1200 grit in 25-50 μm increments until a thickness of approximately 150 μm was attained. A Dimpler[®] model P300 rotary thinning tool with 6 μm diamond slurry and a 20 g force offset was used to reduce the foil thickness at the center to approximately 20 μm . Dimpling was followed by ion milling on a Gatan Model 600 dual ion mill at 6 kV and 1 mA with an initial milling angle of 18°, adjusted to 12° for about 1 h

after initial foil perforation. Through this procedure, the area adjacent to the hole in the foil was thinned to a degree sufficient for electron penetration.

Output from TEM analysis included bright-field and dark-field images along with selected-area and convergent-beam diffraction patterns. Resultant diffraction patterns were indexed by standard techniques [142] to determine lattice constants and phase identity.

3.3 Results and Discussion

3.3.1 Processing

Consistent with the primary project goal of examining the mechanical behavior of $\text{Mo}_5\text{Si}_3\text{C}$, the processing of $\text{Mo}_5\text{Si}_3\text{C}$ -based materials was undertaken within the context of what combination of processing routes and process variables allowed for the production of nearly single-phase, fully dense, crack-free samples of various grain sizes. It was recognized from the outset that achieving all goals in terms of material homogeneity and quality could be quite challenging, thus an emphasis was placed on optimizing microstructures as much as possible with respect to sample homogeneity, integrity, and microstructural scale while attempting to quantify and correlate undesirable sample features when they appeared. In addition, every attempt was made to assess processing routes and compositions in a systematic fashion so that the effects of specific process variables and stoichiometry changes could be delineated. Complementary to this systematic, iterative approach was an emphasis on quality and process monitoring during all processing stages and an effort to develop a repeatable set of procedures for each process thereby reducing potential variability.

3.3.1.1 Compositions studied

An initial step in the processing study of $\text{Mo}_5\text{Si}_3\text{C}$ was the identification of target compositions for arc melting and hot pressing. As previously mentioned, a significant degree of stoichiometric variation for $\text{Mo}_5\text{Si}_3\text{C}$ is reported in the literature [18], indicating that single-phase $\text{Mo}_5\text{Si}_3\text{C}$ is stable over a range of compositions (Figure 3.4). As a way to

examine potential compositional effects on mechanical properties, it was decided initially to produce samples of two compositions (1 and 2 in Table 3.3) in the $\text{Mo}_3\text{Si}_3\text{C}$ single-phase field having different amounts of carbon but the same Mo:Si ratio. However, over the course of the project, a significantly expanded number of compositions was produced, primarily because of difficulties in achieving single-phase $\text{Mo}_3\text{Si}_3\text{C}$, which will be discussed in more detail below.

3.3.1.2 Arc melting

Non-consumable arc melting (AM) was considered as a potential processing method for $\text{Mo}_3\text{Si}_3\text{C}$ based on its reputation as a quick, efficient way to melt high-melting point metals for alloy development. One primary advantage of arc melting over powder metallurgy-based methods is the much higher degree of sample cleanliness possible through arc melting. A controlled, high purity atmosphere is used during arc melting in addition to oxygen-gettering titanium buttons, and the solid melt stock are all expected to lead to lower contamination levels than present in their powder-processed counterparts. Compositions produced through arc melting were 1 and 2 (Table 3.3), containing 13.8 and 11.4 At. % carbon, respectively.

An as-cast microstructure for one of these alloys is shown in Figure 3.5 and clearly displays a multiphase structure. This type of microstructure was observed for all arc-melted specimens, and XRD indicated that the major phase was Mo_3Si_3 , not $\text{Mo}_3\text{Si}_3\text{C}$, meaning that the samples were not fully equilibrated and the carbon had not dissolved completely. This is consistent with observations during the melting process of the graphite pieces used as the carbon source not dissolving under the arc, but rather floating on the melt button even after multiple re-melts. Similarly, the Mo-carbide visible in Figure 3.5 is likely a residual unmelted Mo-C master alloy.

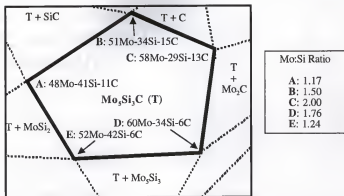


Figure 3.4 Close up of $\text{Mo}_3\text{Si}_3\text{C}$ single phase region taken from the accepted Mo-Si-C 1600°C isotherm (Fig. 2.10) by Nowotny et al. [18]. The compositions for the five terminal points (A-E) of the single phase field were estimated from Eq. 2.4 given for the compositional variation of $\text{Mo}_3\text{Si}_3\text{C}$ in [18].

Table 3.3 Compositional information for samples produced via arc melting (AM), powder blending followed by hot pressing (PBHP), and mechanical alloying followed by hot pressing (MAHP). All compositions shown are nominal (as measured).

Comp. ID	Mo (At.%)	Si (At.%)	C (At.%)	Mo:Si Ratio	Processing Routes	Total No. Samples
1	53.5	32.7	13.8	1.64	AM	5
2	55	33.6	11.4	1.64	AM	4
7	54.5	33	16	1.65	MAHP, AM	10
10	55.5	33.5	11	1.66	PBHP	3
11	59	35.6	5.4	1.66	PBHP	1
13	52.3	37	10.7	1.41	PBHP	2
15	57.2	34.7	8.1	1.65	PBHP	2
C05	59.4	35.65	5	1.67	PBHP	1
C75	57.9	34.6	7.5	1.67	PBHP	1
C8B	56.2	35.8	8	1.57	PBHP	1
C10	56.3	33.7	10	1.67	PBHP	2
C10B	55.3	34.7	10	1.59	PBHP, MAHP	19
C125	54.7	32.8	21.5	1.67	PBHP	1
C15	53.2	31.8	15	1.67	PBHP	1

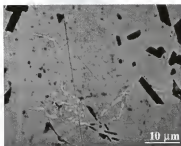


Figure 3.5 Back-scattered electron (BSE) image of CN 2 sample produced by arc melting. Phases displaying dark contrast are SiC, while the lighter-contrast necklace of features are $\text{Mo}_5\text{Si}_3\text{C}$. The majority phase constituent is $\text{Mo}_5\text{Si}_3\text{C}$.

The lack of homogeneity in the samples points to the difficulty of combining elements having a broad range (Si-1685 K, Mo-2890 K, C-4100 K) of melting points—even with the two-step melting process used, attempts to homogenize through further re-melting would have resulted in excessive losses due to silicon vaporization. Heat treatments under a controlled atmosphere are another common approach to alloy homogenization, but the extremely slow decomposition kinetics reported for molybdenum carbides [137] would have resulted in excessive heat treat times (hundreds of hours) and therefore, this approach was rejected as impractical for the purposes of this study.

Arc melting presented further complications with respect to producing samples having sufficient integrity for mechanical testing as all specimens contained significant shrinkage porosity and pervasive macrocracking after solidification (Figure 3.6). The massive cracking observed is probably a result of the large temperature gradient between the top of the arc melted button most recently under the welding arc and the bottom of the button in contact with the copper chill plate. This gradient likely generates thermal stresses that cannot readily be accommodated by the material; the hexagonal D8_h structure of $\text{Mo}_5\text{Si}_3\text{C}$ may result in additional susceptibility to thermally-induced cracking because of

probable thermal expansion anisotropy, seen in other non-cubic intermetallics such as the isostructural Ti_5Si_3 compound [103, 104].

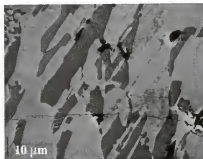


Figure 3.6 Scanning electron micrograph of AM sample of CN 7 showing significant cracking in the as-cast microstructure. The lighter major phase is Mo_5Si_3 , the dark gray elongated phase is MoSi_2 and the black regions are SiC and porosity.

A further impediment to the effective use of AM as a means to produce mechanical test specimens is the lack of grain size control inherent in the process. Typical matrix grain sizes of arc melted samples are in excess of $100\text{ }\mu\text{m}$; to vary this reproducibly with the current setup would be very difficult given the low degree of heat input control and the basically fixed cooling rate imposed by the water cooled copper hearth. Traditional methods of refining and/or modifying the as-cast structure by thermo-mechanical processing have been successfully applied to aluminides [143], although it is doubtful these methods would be feasible for the heavily-cracked silicide buttons produced in this study.

3.3.1.3 Powder processing methods

Given the difficulties encountered during arc melting, processing approaches based on the pressure-assisted sintering of powders were evaluated for production of $\text{Mo}_5\text{Si}_3\text{C}$ -based materials. The primary reason for considering methods based on powder mixing

(PM) was the large degree of flexibility in starting materials, with parameters such as form (elemental or compound), purity, powder size, and size distribution all having the potential to be tailored for a given sample. Varying starting powder size is an obvious way to affect changes in microstructural scale [52], and the more controllable heating and cooling rates available through hot pressing is a further aid to grain size control. Another potential advantage to PM techniques is that by optimizing process parameters, near-fully dense and crack-free bodies can be produced. A final reason to consider powder processing for $\text{Mo}_3\text{Si}_3\text{C}$ -based materials was the large experience base in our research group in powder processing of silicide compounds [13, 58, 73, 126].

The two-stage hot pressing scheme used throughout this study was arrived at based on the work of Henager et al. [72] and Jayashankar [63] on processing of *in situ* composites in the Mo-Si-C systems. In both cases, these researchers used a lower temperature hold followed by a higher temperature densification step. The initial hold is necessary to allow the volatile reaction products of carbon and siliceous powders to leave the sample; it is important that this step be performed under vacuum with only minimal application of mechanical pressure so as to not entrap gas in the sample (Figure 3.7). The densification step is carried out at higher temperature to accelerate the diffusional processes necessary for powder consolidation; this step is done under an applied pressure of 50 MPa to further assist densification while the HP chamber is backfilled with argon to minimize potential silicon losses due to the high vapor pressure of Si at temperatures above 1600°C (Figure 2.4).

Powder mixing + hot pressing. The compositions prepared using this method made up the majority of those studied in this work (Table 3.3) and covered a range of carbon contents from 5 to 16 At.% and variation in Mo:Si ratio of 1.41 to 1.67. As seen in Table 3.4, elemental and compound powders covering a broad range of powder sizes were used as raw materials.



Figure 3.7 Scanning electron micrograph illustrating the effects of applied mechanical pressure on trapping gaseous reaction products in the form of gas porosity (dark spots). Sample of C10B composition, hot pressed at 1350°C for 2 h in vacuum (< 0.13 Pa) under applied pressure of 47 MPa followed by 1 h at 1700°C in argon atmosphere (~50 kPa).

Powders were blended prior to hot pressing in a tumbler ball mill for 2 h with the idea of breaking up agglomerates and producing a more uniform powder mixture prior to hot pressing. The effects of this process are shown in Figure 3.8, where the number of agglomerates equal to or larger than 200 μm is reduced by more than 60 percent after ball

Table 3.4 Powder size information for starting powders used in this study. All powder statistics were measured on a Coulter LS230 particle size analyzer without surfactant additions.

Powder	Reported Particle Size (μm)	Mean Particle Size (μm)	Mode (μm)	Standard Deviation (μm)	50% Vol. Less than (μm)	90% Vol. Less than (μm)
C	<50	45.5	19.8	64.2	18.4	138.7
Si	45-150	115.1	140.1	54.1	120.2	183.9
Si	<45	40.8	80.1	36.1	16.8	91.4
Mo	45-100	69.5	66.4	10.1	68.4	82.4
Mo	3-7	19.1	14.9	21.8	13.9	30.5
Mo ₂ C	<45	71.9	127.6	68.5	77.3	164.1
Mo ₂ Si ₃	5.4	13.2	10.3	10.5	10	28.4
Mo ₂ Si ₁	<45	6.3	5.4	4.9	5.1	12.7

milling (Figure 3.6 (b)); a slight reduction in mean particle size (107.3 to 94 μm) is seen as well. Discrepancies were noted in several cases between the particle sizes quoted by the raw materials vendors and those measured through particle size analysis; for example the Mo, Mo_2C , and Mo_5Si_3 (5.4 μm reported) in Table 3.4 are all larger than expected, indicating a propensity for agglomeration.

Several representative microstructures of samples processed through blending of powders and hot pressing are shown in Figures 3.9 and 3.10. From these micrographs, it is clear that significant variation in phase type and volume fraction is possible depending on starting materials and composition. Phase identification for the samples shown was accomplished through a combination of x-ray diffraction and WDS. Comparing the phases present in these samples to those expected from their starting composition gives the first indication of some combination of a discrepancy with the reported size of the single-phase field for $\text{Mo}_5\text{Si}_3\text{C}$ (Fig. 3.4), compositional shifts occurring during processing, and non-equilibrium microstructures. Compositions (CN) 11 (Fig. 3.9 (a)) and C15 (Fig. 3.10 (b)) have carbon contents that should position them on the bottom and top, respectively, of the single-phase field and would be expected to contain at most a few volume percent of secondary phases, which is not the case. The nearest single-phase sample (Fig. 3.10 (a)) is that processed at CN C10B, having the nominal composition 55.3Mo-34.7Si-10C. Issues concerning the actual compositional range of $\text{Mo}_5\text{Si}_3\text{C}$ will be discussed in more detail below. Phase stability issues aside, samples processed through powder mixing and hot pressing do exhibit the expected refinement in structure (Figure 3.11), control of microstructural scale, and reduction of macro-cracking compared with the arc-melted specimens.

Transmission electron microscopy (TEM) of a thin foil of CN C10B (Figure 3.12) reveals further information about phases present and their crystal structures. As seen in the bright-field image (BF) (Fig. 3.12 (a)), a two-phase microstructure of thinner (light contrast) and thicker (dark contrast) regions is present in this region. A selected-area

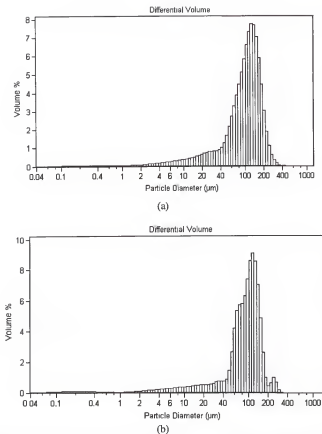
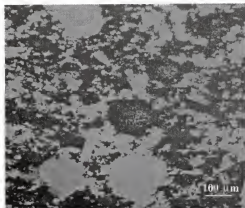
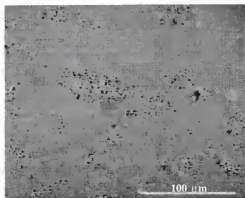


Figure 3.8 (a) Particle size distribution for the as-received Mo, Si, and C powders. (b) Particle size distribution for same powders after 2 h ball milling showing a decreased number of agglomerates $\geq 200 \mu\text{m}$ and slight reduction in mean particle size.



(a)

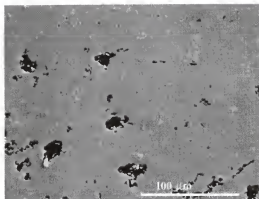


(b)

Figure 3.9 (a) Scanning electron microscope (SEM) image of hot pressed sample of CN 11. Phase displaying light contrast is $\text{Mo}_7\text{Si}_3\text{C}$, while darker phase is Mo_5Si_3 , and very fine, lighter phase is Mo_7C . (b) SEM image of CN 15, produced from a blend of Mo_7C , Mo, and MoSi_2 . Matrix is $\text{Mo}_5\text{Si}_3\text{C}$, light gray platelets are Mo_7C , and black dots are likely a mixture of porosity and SiO_2 from the MoSi_2 powder precursor.



(a)



(b)

Figure 3.10 (a) Micrograph from SEM of composition C10B. Matrix is $\text{Mo}_5\text{Si}_3\text{C}$ with fine SiC encircling gas porosity (linear features). (b) Micrograph of CN C15. Matrix is $\text{Mo}_5\text{Si}_3\text{C}$, dark regions are carbon-rich, and light particles are Mo_4C .

diffraction (SAD) pattern from a "thicker" region (Fig. 3.12 (b)) is consistent with a hexagonal crystal structure oriented along the [0001] beam direction; indexing of this pattern along with a $\mathbf{B} = [11\bar{2}0]$ SAD (not shown) yield lattice parameters of $a = 0.733$ nm and $c = 0.509$ nm. These calculated parameters are close to those reported by JCPDS PDF 43-1199 for $\text{Mo}_{4.8}\text{Si}_3\text{C}_{0.6}$ of $a = 0.7292$ nm and $c = 0.5043$ nm as well those of $a = 0.7286$ nm and $c = 0.5046$ nm from a previous XRD and neutron diffraction study [137].

For the brighter (i.e., thinner), faulted regions of Figure 3.12 (a), the SAD patterns (e.g., Figure 3.12(c)) can be indexed as cubic with a lattice parameter of $a \sim 0.437$ nm, which is close to that of 0.436 nm reported for cubic β -SiC [58]. Furthermore, the faulted appearance of the SiC platelets in the BF image results in streaking and extra diffraction spots (twin spots) as seen in the [011] SAD pattern. Twinning along {111} in β -SiC is not uncommon and has been reported for both vapor-deposited material [144] and carbides resulting from melt processing [78]. The relatively large fraction of SiC observed during TEM analysis is somewhat surprising considering the nearly single-phase nature of the bulk sample (Fig. 3.10 (a)), although preferential thinning near the aforementioned SiC-pore regions is a plausible explanation.

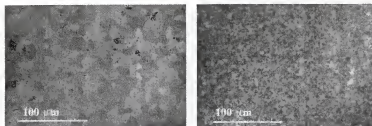


Figure 3.11 Images of powder processed samples showing grain contrast under polarized light. Light optical micrograph on left is of composition C10B; average grain diameter calculated through line intercept methods is 16.8 ± 2.1 μm . Dark regions are porosity. Optical micrograph on right is of C10B with an average grain diameter of 5.6 ± 0.5 μm .

Mechanical alloying + hot pressing. Mechanical alloying (MA) of powders followed by hot pressing was explored as a variant of powder blending methods. Attractive features of MA include refined particle sizes ($< 1 \mu\text{m}$), lower processing temperatures/reduced times, and the ability to synthesize phases during the high energy MA process [49]. Starting compositions of MA samples included CN 7 and C10B. As anticipated, starting powders of Mo_5Si_3 ($< 45 \mu\text{m}$), Si ($< 45 \mu\text{m}$) and C ($< 50 \mu\text{m}$) did show more than a 60 % reduction in mean particle size after a 15 h alloying cycle (Figure 3.13).

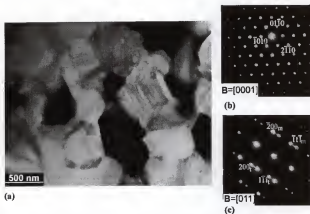


Figure 3.12 (a) Bright field (BF) image of $\text{Mo}_5\text{Si}_3\text{C} + \text{SiC}$ region. The dark areas are the ternary phase, while the light, faulted areas are β -SiC. (b) Selected area diffraction pattern (SADP) taken from dark phase, showing the hexagonal $D8_h$ structure of $\text{Mo}_5\text{Si}_3\text{C}$. (c) SADP ($B=[011]$) of light phase where streaking lines indicates twinning along $\{111\}$ in cubic β -SiC. The m subscripts indicate matrix reflections, while the t subscripts denote twin reflections.

During some MA runs, significant sticking and caking of powders to the steel milling media and vial was observed leading to large agglomerates ($\sim 500 \mu\text{m}$) and reduced powder yield. To counteract caking, $\sim 0.2 \text{ g}$ of stearic acid flakes were added to the powder

charge, the milling media, and milling vial surfaces; the effectiveness of stearic acid is shown in Figure 3.14, which shows the particle size distributions for identical powders and MA runs with and without stearic acid additions.

Microstructures of consolidated MA specimens (Figure 3.15) are basically fully dense and exhibit a matrix grain size typically less than 10 μm , with many grains in the 1 μm range. This fine scale complicated compositional analysis using EPMA, as many of the regions of interest were on the order of the spatial resolution of WDS ($\sim 1 \mu\text{m}$), creating problems with interference and overlap between phases.

Elevated oxygen contents due to the increased surface area of the fine MA powders [9, 56] and contamination from milling media [39] are both concerns when using MA processes. In fact, samples produced through hot pressing of MA powders did show increased oxygen content in the form of $\sim 2\text{-}6 \text{ Vol.}\%$ amorphous silica particles (Figure 3.16), a feature not present in blended powder samples of the same composition. Conflicting results in the literature regarding oxygen pickup during MA of silicide materials [49] indicate the importance of MA process variables. For the materials produced in this study, the amount of silica present in the consolidated bodies probably would have been reduced by process modifications such as adding excess carbon to more fully reduce the silica present and minimizing powder exposure to air after milling by handling the powders in an inert atmosphere (e.g., glove bag). The reactions between silica and carbon occurring during processing will be outlined in more detail below.

One feature of the silica present in these $\text{Mo}_5\text{Si}_3\text{C}$ -based materials is that while there are concentrations of the amorphous phase along grain boundaries, there are also many instances of silica appearing within grains (Figure 3.15) in contrast to much of the data on powder-processed MoSi_2 where SiO_2 is typically reported as present primarily at grain boundaries and triple points [58, 87]. The silica that is present along grain boundaries and at triple points in the $\text{Mo}_5\text{Si}_3\text{C}$ -containing materials may act to stabilize the refined structure by limiting grain growth due to a Zener drag mechanism [61].

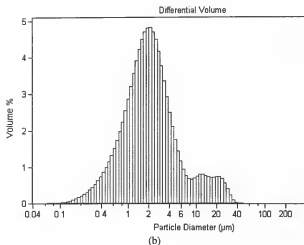
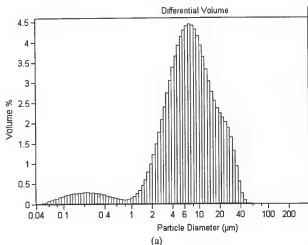


Figure 3.13 Comparison of particle size distribution before (a) and after (b) 15 h of mechanical alloying of a 25 g powder charge at a milling media:charge ratio of 2:1.

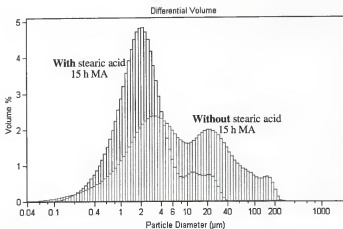


Figure 3.14 Comparison plot of particle size distribution of identical starting powders after 15 h MA run with and without stearic acid additions. Note the bimodal distribution for the powders milled without stearic acid and the large number of particles with diameters greater than 20 μm .

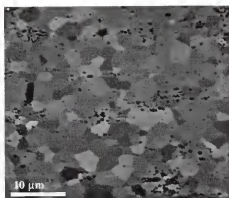


Figure 3.15 Micrograph (BSE image) of sample having composition C10B produced from mechanically alloyed powders. Matrix phase showing grain contrast is $\text{Mo}_3\text{Si}_3\text{C}$, while minor phase with bright contrast is Mo_5C , and sub-micron black particles are either silica or porosity.

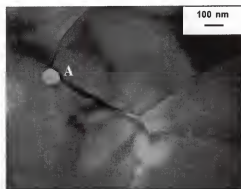


Figure 3.16 Bright-field image of MA sample (CN C10B) showing presence of amorphous silica particle near triple point (A).

Though less obvious than the presence of silica, slight contamination from the steel milling balls and vial in the form of iron was detected from WDS analysis of some mechanically alloyed specimens, typically on the order of 2500 ppm in the $\text{Mo}_3\text{Si}_3\text{C}$ phase. It has been reported that iron partitions readily to the $\text{Mo}_3\text{Si}_3\text{C}$ phase [58] in MA Mo-Si-C materials, although the Fe content reported in the ternary phase is significantly higher than that observed in the present study. It is unclear whether the minor iron contamination might effect phase formation or mechanical behavior of $\text{Mo}_3\text{Si}_3\text{C}$ -containing materials as Fe likely substitutes on Mo-lattice sites.

Carbon-silica reaction issues. With most powder processing methods, the potential exists for the retention of residual phases within consolidated bodies from either intentional (e.g., sintering aids) or unintentional (e.g., oxides on powder surfaces, contamination) sources. As previously discussed, the presence of oxide scales on silicon-containing starting materials leads to the presence of discrete amorphous silica within powder-processed silicide materials. With samples that also contain carbon as either a contaminant or, as in this study, alloying element, reactions inevitably occur during processing that lead to silica reduction with concomitant loss of carbon and production of solid and/or gaseous by-products.

In addition to carbon loss, the silica present on the starting powders leads to an over-estimation of the amount of Si-containing constituent proportional to the percentage of oxygen in the starting siliceous powder. The net result of these two factors is a depletion in Si and C with respect to the nominal composition of a Mo-Si-C alloy, pushing the final composition toward the Mo-rich corner of the Mo-Si-C isotherm. Microprobe analysis and phase distributions of powder-processed samples typically do indicate a slight increase in the Mo:Si ratio compared to starting compositions, consistent with compositional shifts toward the Mo-rich corner. Because the questionable accuracy of light element analysis using WDS, especially for minor amounts [141], light element analysis using combustion/IR techniques was used to quantify the bulk carbon and oxygen content of

several hot pressed specimens. Calculations based on the results of light element analysis show an average depletion of carbon of 1.4 At. % during processing and an average oxygen content of 1544 ppm for the consolidated samples; without using glove box handling or powder etching, this oxygen content is still lower than those typically reported for consolidated silicide materials (Table 2.3); this testifies to the effectiveness of carbon as a catalyst for silica removal. On average, approximately 16 % of the mass of carbon initially in the powder compacts is lost due to reactions with the siliceous components.

Calculations based on a single mechanism (Equation 3.3) assuming complete reaction of an amount of silica in the starting powders equivalent to 2 Wt. % oxygen (from Table 2.3), give an estimated carbon loss in the range of 0.5 to 4 At. %. The magnitude of the estimated loss varies depending on choice of starting materials. It was assumed that different forms of siliceous materials would have equivalent oxygen contents, although this is probably not the case. This explains the large shift predicted (4 At. % C) for $\text{Mo}_5\text{Si}_3 + \text{C}$ samples since the weight fraction of the Si-containing compound (and thus oxygen) is much higher than for samples containing elemental silicon, which probably contains more silica than Mo_5Si_3 for equivalent surface areas due to the higher activity of Si. In these calculations, it is also assumed that all SiO_2 in the starting powders is in intimate contact with carbon, and that no additional carbon enters the powder compacts by diffusion from the graphite paper liners surrounding the compacts during hot pressing. In spite of these uncertainties, the calculated depletion range does encompass the experimentally-observed 1.4 At. % loss, lending some credibility to the calculations.

Evidence of a deoxidation reaction of the type



is seen in Figure 3.17, where a network of β -SiC platelets surrounds a pore, presumably the result of gaseous evolution, in an otherwise single phase material (C10B). These pore/SiC regions tend to be linear in appearance (in cross section) with their long axis perpendicular to the hot pressing direction, indicative of a morphology change occurring

during the densification step. Unlike the majority of gas and sintering porosity existing prior to densification, these SiC/pore regions do not fully close out during densification, likely because of the SiC boundary layer acting as a mechanical and diffusion barrier to pressure-assisted close out of the pore.

Rather than forming these SiC/pore structures, it might be more desirable to produce only gaseous reaction products of the silica reduction during the initial stages of hot pressing and then minimize the subsequent gas porosity through pressure-assisted sintering. However, the SiC/pore defects as in Fig. 3.14 appeared in a number of hot pressed samples of different compositions, indicating that the favored silica reduction mechanisms are those that result in the formation of SiC. Recall that in addition to Equation 3.3, another possible silica reduction reaction is,



indicating the potential for the removal of SiO_2 with only gaseous byproducts. A plausible explanation for SiC-forming reactions (e.g., Eq. 3.3) predominating in hot-pressed samples is shown in Figure 3.18, in which the free energy changes associated with three possible SiO_2 -carbon reactions are plotted as a function of temperature. Over the range of temperatures used in processing, the free energy change of Eq. 3.3 is the smallest, meaning that it is the favored reaction from a thermodynamic standpoint; above $\sim 1510^\circ\text{C}$, the ΔG for Equation 3.3 is negative indicating a driving force for the reduction of silica and the production of SiC and carbon monoxide gas. The ΔG values for the other two possible reactions remain positive and thus it is doubtful that their reaction products would be favored under equilibrium conditions. The calculations assume the activity of carbon is constant throughout the reaction which is not actually the case as carbon is consumed. In fact it has been reported that decreasing carbon activity increases the amount of SiO(g) produced during the reduction of SiO_2 ; at 1507°C , all carbon is consumed to form SiC and only at temperatures in excess of 1700°C does the increased P_{SiO} alter the products of the reduction reaction from SiC to free silicon [145]. It has been proposed that lower partial

pressures of oxygen and a reducing atmosphere, as the case with vacuum hot pressing in graphite dies, shift these free energy curves to lower temperatures, implying the reduction of silica during hot pressing probably begins to occur below 1510 °C [146].

In several cases (e.g., CN 7), intentional additions of excess carbon and silicon were added in hopes of correcting for the inevitable compositional shifts caused by silica-carbon reactions. However, it proved to be difficult to gauge the effectiveness of these attempts for several reasons. First of all, since accurate information on starting oxygen content of silicon or silicide powders was lacking, assumptions were made in order to estimate the additions needed. Accurate quantitative measurement of carbon was not readily available at our facilities, so systematic measurements of carbon losses in samples with intentional additions was not possible. Finally, uncertainties about the size of the $\text{Mo}_5\text{Si}_3\text{C}$ single-phase field made it difficult to determine what phases and phase amounts should be present for given nominal and target compositions. In addition to adding excess carbon, another route explored to possibly achieve tighter control over stoichiometry was the use of larger Si powders ($\sim 115 \mu\text{m}$) because of their decreased surface area for oxidation and assumed lower levels of oxygen. However, the impact of larger silicon powders on composition shifting were inconclusive and the consolidated bodies tended to be less dense than those produced from finer powders.

3.3.2 Compositional Range of $\text{Mo}_5\text{Si}_3\text{C}$

In spite of producing samples at a number of compositions within the reported $\text{Mo}_5\text{Si}_3\text{C}$ single-phase region using different processing routes, nearly all of these materials contained at least five volume percent of other phases. Though complicated somewhat by issues such as homogenization difficulties with arc melted specimens, contamination during MA processes, and compositional shifts during hot pressing, it is proposed that the most significant obstacle to producing single phase $\text{Mo}_5\text{Si}_3\text{C}$ is a much narrower compositional range for this phase than originally thought. To more thoroughly address this issue, it was

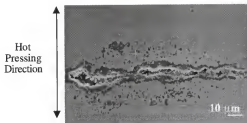


Figure 3.17 Image from SEM of pore surrounded by β -SiC in hot pressed sample. This feature is thought to be the result of reactions between carbon in the sample and SiO_2 on the starting powders.

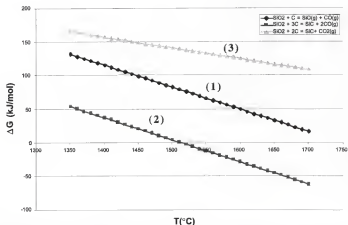


Figure 3.18 Plot of equilibrium free energy versus temperature for three possible reactions between carbon and silica. Plot generated from HSC Chemistry software package and the thermodynamic database contained therein. The trend with temperature predicts that only reaction (2) has sufficient driving force to spontaneously generate its products at temperatures below 1700°C.

decided to systematically reassess the range of compositional variation for the $\text{Mo}_5\text{Si}_3\text{C}$ phase by producing samples through blending of powders and HP, focusing in one set of samples on the range of Mo:Si ratios (width) and in the other on carbon content (height) of the single-phase field as shown in Fig. 3.4.

A summary of phase identification and composition information from XRD, EPMA, and light element analysis for several samples representative of those used to examine the compositional range of $\text{Mo}_5\text{Si}_3\text{C}$ is presented in Table 3.5 and Table 3.6.

3.3.2.1 Width of $\text{Mo}_5\text{Si}_3\text{C}$ single-phase field

To investigate the range of Mo:Si ratios over which $\text{Mo}_5\text{Si}_3\text{C}$ existed as a single phase, starting powders of Mo_2C and Si or Mo_5Si_3 , Si, and C were blended and hot pressed using the standard two step pressing method. As shown in Figure 3.19, samples having average $\text{Mo}_5\text{Si}_3\text{C}$ Mo:Si ratios (Table 3.5) of 1.60 and 1.69 as measured by WDS were not solely $\text{Mo}_5\text{Si}_3\text{C}$ as would be expected from Figure 3.4. These samples contained roughly equal fractions of secondary phases, placing them in the $\text{Mo}_5\text{Si}_3\text{C} + \text{SiC} + \text{MoSi}_2$ (CN 13) and $\text{Mo}_5\text{Si}_3\text{C} + \text{Mo}_2\text{C}$ (CN 10) phase fields on opposing sides of the $\text{Mo}_5\text{Si}_3\text{C}$ single phase region. Composition C8B has an average Mo:Si ratio in the $\text{Mo}_5\text{Si}_3\text{C}$ matrix of 1.65 and is nearer to being single phase than either CN 10 or 13, although it still contains 5.7 Vol.% of the Mo_5Si_3 phase.

In the work of Nowotny et al. [18], it was reported that going from Mo-lean (Mo:Si ~1.2) to Mo-rich (Mo:Si ~2.0) compositions across the $\text{Mo}_5\text{Si}_3\text{C}$ field, the axial ratio (c/a) of $\text{Mo}_5\text{Si}_3\text{C}$ increased from 0.687 to 0.695. A change in lattice parameters across a single-phase field is not unusual [147], although in the case of $\text{Mo}_5\text{Si}_3\text{C}$ other researchers [12, 19, 120] have observed a much smaller compositional range over which this lattice parameter variation occurs. In the present work, the c/a ratio did increase with increasing Mo content from 0.689 to 0.694, but over a Mo:Si ratio range of approximately 0.1, which is significantly less than the ~0.8 given by Nowotny et al [18]. For samples in this study

Table 3.5 Summary of data from XRD and WDS pertinent to the examination of the compositional variation of $\text{Mo}_3\text{Si}_3\text{C}$.

CN	XRD Phase ID <i>Major minor</i>	c/a Ratio $\text{Mo}_3\text{Si}_3\text{C}$	Mo (At. %) Matrix	Si (At. %) Matrix	C (At. %) Matrix	Mo:Si Ratio Matrix
13	$\text{Mo}_3\text{Si}_3\text{C}$	0.689	60.2 \pm 1.6	37.6 \pm 1.5	2.1 \pm 2.3	1.60 \pm 0.07
C8B	$\text{Mo}_3\text{Si}_3\text{C}$, Mo_3Si_3	0.687	61.2 \pm 1.7	37.1 \pm 0.9	1.7 \pm 2.6	1.65 \pm 0.01
10	$\text{Mo}_3\text{Si}_3\text{C}$, Mo_3C	0.694	59.1 \pm 1.3	34.9 \pm 1	6.0 \pm 1.7	1.69 \pm 0.06
C75	$\text{Mo}_3\text{Si}_3\text{C}$, Mo_3Si_3	0.694	60.2 \pm 1.6	36.7 \pm 1.0	3.0 \pm 0.98	1.64 \pm 0.09
C10	$\text{Mo}_3\text{Si}_3\text{C}$, Mo_3C	0.695	60.7 \pm 1.1	35.9 \pm 0.72	3.5 \pm 1.2	1.69 \pm 0.05
C125	$\text{Mo}_3\text{Si}_3\text{C}$, Mo_3C	0.695	58.0 \pm 1.6	37.2 \pm 1.4	4.8 \pm 0.95	1.56 \pm 0.1

Table 3.6 Light element analysis and phase fractions from image analysis for samples in compositional range study.

CN	C (Wt. %) Bulk Analysis	Equivalent At. % C	Oxygen (ppm) Bulk Analysis	Second Phase Vol. %
13	-	-	-	6.1 SiC, trace MoSi_2
C8B	-	-	-	5.7 Mo_3Si_3
10	1.77 \pm 0.04	9.82 \pm 0.2	558 \pm 25	7.7 Mo_3C , trace C
C75	1.12 \pm 0.01	6.22 \pm 0.05	2450 \pm 1670	22.7 Mo_3Si_3 , 1.8 Mo_3C
C10	1.49 \pm 0.02	8.25 \pm 0.1	897 \pm 163	3 Mo_3C
C125	2.02 \pm 0.12	11.24 \pm 0.6	2274 \pm 1551	2.7 Mo_3C , 1.8 C

with higher Mo contents ($\text{Mo/Si} \geq 1.7$), the $\text{Mo}_3\text{Si}_3\text{C}$ c/a ratio approached a constant value of 0.695, indicating that the composition of the ternary phase had reached a terminal value as overall compositions pushed further into two- or three- phase fields.

3.3.2.2 Height of $\text{Mo}_3\text{Si}_3\text{C}$ single-phase field

Samples for examining the variation of $\text{Mo}_3\text{Si}_3\text{C}$ carbon content were produced from blended and hot pressed powders of Mo_3Si_3 and carbon. Starting with a Mo:Si ratio of 1.67 dictated by the Mo_3Si_3 stoichiometry (Figure 3.20), samples having final bulk carbon contents of 6.2 At. % (CN C75, Figure 3.20 (c)) and 11.2 At. % (CN C125, Figure 3.20 (a)) contain $\text{Mo}_3\text{Si}_3\text{C} + \text{Mo}_3\text{Si}_3$ (22.7 Vol. %) + Mo_2C (1.8 Vol. %) and $\text{Mo}_3\text{Si}_3\text{C} + \text{Mo}_2\text{C}$ (2.7 Vol. %) + C (1.8 Vol. %), respectively. Note the aforementioned shifts in composition toward the Mo-rich corner of the Mo-Si-C isotherm after hot pressing. Even with the variations in stoichiometry presumably due to C-SiO₂ reactions, samples such as these having Mo:Si ratios near 1.67 are predicted to remain single-phase $\text{Mo}_3\text{Si}_3\text{C}$ for carbon contents from 6 to 15 At. % (Fig. 3.4) which is obviously not the case. One area in which there is agreement with the original study [18] and more recent work [120] is the minimal variation in the $\text{Mo}_3\text{Si}_3\text{C}$ c/a ratio with carbon content, from 0.694 to 0.695 at overall carbon contents of 5 and 15 At. % C, respectively.

3.3.2.3 Heat treatment

A possible explanation [120] for the much smaller homogeneity range for $\text{Mo}_3\text{Si}_3\text{C}$ reported in the current work and others [12, 19, 120] is that these studies used processing and/or equilibration temperatures other than 1600°C, the temperature for the original isotherm in Figure 2.12. It is plausible that shifts in phase boundaries could occur at some intermediate temperature (i.e., $T < 1600^\circ\text{C}$). In addition, samples produced through hot pressing may not have been fully equilibrated. To investigate these issues, several samples were heat treated at 1600°C and the resultant microstructures characterized by SEM and WDS. As seen in Fig. 3.21 (b), a sample initially containing Mo_2C and C in a $\text{Mo}_3\text{Si}_3\text{C}$

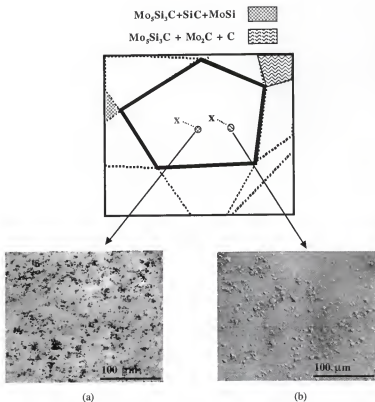


Figure 3.19. Schematic representation of samples used for the width estimation of the $\text{Mo}_5\text{Si}_3\text{C}$ single-phase field. Both CN 13 (a) and 10 (b) have starting (x) and final (•) Mo:Si ratios within the range for $\text{Mo}_5\text{Si}_3\text{C}$ (T) predicted by Nowotny et al. [18], while the phases present in the microstructures indicate that these samples are actually in the adjacent three-phase fields T + SiC + MoSi, and T + Mo_2C + C. The phase displaying dark contrast in (a) is SiC (MoSi, is not clearly discernable in this micrograph), while lighter, raised phase in (b) is Mo_2C and very fine black particles are free carbon.

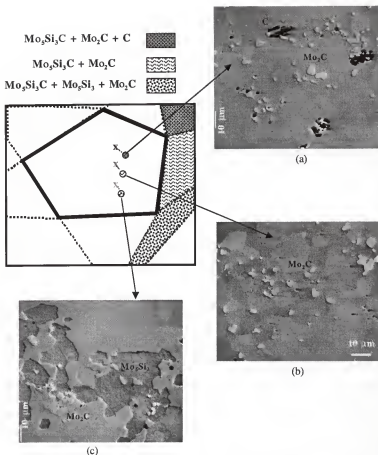


Figure 3.20 Schematic representation of samples used to examine the height of the $\text{Mo}_5\text{Si}_3\text{C}$ single-phase field. Samples are compositions C125 (a), C10 (b) and C75 (c), hot-pressed blends of $\text{Mo}_5\text{Si}_3 + \text{C}$, SEL. All three samples exhibit multiphase microstructures at final (*) carbon amounts that fall within the $\text{Mo}_5\text{Si}_3\text{C}$ field according to [18].

matrix shows little difference in phase type, distribution or scale of microstructure after 12h at 1600°C.

Microprobe analysis is inconclusive for this sample, with the heat-treated specimen showing reduced carbon content in the $\text{Mo}_5\text{Si}_3\text{C}$ matrix as well as in the remaining carbide phase compared with the as-hot-pressed sample, but not to a significant degree. While this may indicate that the as hot pressed sample may not have been fully reacted, and is consistent with the sluggish decomposition kinetics reported for Mo-carbide phases [137], it seems unlikely that extended heat treatments would produce a single-phase $\text{Mo}_5\text{Si}_3\text{C}$ microstructure (i.e., the as-hot-pressed structure is close to equilibrium). The relatively large scale of the carbide phase relative to the matrix is probably a result of retaining undissolved Mo_2C from the starting $\text{Mo}_2\text{C}+\text{Mo}+\text{Si}$ powder mixtures.

In their work on diffusion paths and reaction mechanisms in *in situ* $\text{MoSi}_2\text{-SiC}$ composites, Henager et al. [12] describe the precipitation of fine SiC into $\text{Mo}_5\text{Si}_3\text{C}$ that becomes supersaturated with carbon while van Loo et al. [19] propose that carbon rapidly diffuses from $\text{Mo}_5\text{Si}_3\text{C}$ in contact with Mo forming Mo_2C and Mo_5Si_3 . These results point to the possibility that the solubility of carbon in $\text{Mo}_5\text{Si}_3\text{C}$ may change with temperature and that phases may be precipitated from supersaturated $\text{Mo}_5\text{Si}_3\text{C}$ upon cooling due to the reduced solubility range at lower temperatures (e.g., Figure 2.13). However, the majority of the microstructures produced in the current work are inconsistent with solid-state precipitation of phases from $\text{Mo}_5\text{Si}_3\text{C}$ due to decreasing solubility in the ternary phase with decreasing temperature. The limited phase redistribution during heat treatment at 1600°C and the general observation that the secondary phases in these materials are typically coarser ($\geq 10\text{ }\mu\text{m}$) and less uniformly distributed than what would be expected from second phase formation via precipitation [148], indicate that the majority of the phase formation seen in $\text{Mo}_5\text{Si}_3\text{C}$ -based materials occurs at the hot pressing temperatures (1350-1700°C) and not during cooling.

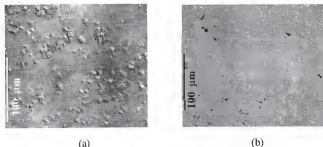


Figure 3.21 (a) Secondary electron image of HP sample of CN 10, showing a $\text{Mo}_5\text{Si}_3\text{C}$ matrix, with Mo_3C (light phase) and a small amount of C (dark phase). (b) Secondary electron image of same sample after heat treatment at 1600°C for 12 h, showing $\text{Mo}_5\text{Si}_3\text{C}$ matrix, with decreased Mo_3C (light phase) and increased amount of free carbon (dark phase).

It is possible that the $\text{Mo}_5\text{Si}_3\text{C}$ phase boundaries may be reduced somewhat at lower temperatures. However, based on the numerous samples produced in this study at compositions encompassing those given for single-phase $\text{Mo}_5\text{Si}_3\text{C}$ which resulted in multiphase structures, the size of the field reported at 1600°C (Figure 3.4) must be a significant overestimation. It is recognized that heat treatment and equilibration of $\text{Mo}_5\text{Si}_3\text{C}$ -based samples with varying initial second phase constituents at several different temperatures would provide a better understanding of the issues surrounding the variation of the $\text{Mo}_5\text{Si}_3\text{C}$ single-phase field size with temperature.

3.3.2.4 Conclusions

One possible explanation for discrepancies between the large compositional range of $\text{Mo}_5\text{Si}_3\text{C}$ reported by Nowotny et al.[18] and more recent work, including this study, is the reliance on x-ray diffraction techniques for phase identification and chemical analysis in the original work. For example, in the current study a sample comprised of three-phases (Figure 3.19 (a)) yielded an x-ray diffraction pattern which was indexed completely to single-phase $\text{Mo}_5\text{Si}_3\text{C}$ (JCPDS PDF 43-1199) with no detectable SiC or MoSi_2 (Figure 3.22). This demonstrates one of the primary drawbacks of relying solely on XRD for

determination of phase diagram boundaries in cases where phase amounts and/or low intensity x-ray patterns from second phases may be below the detection limit of XRD [140].

These results indicate the importance of verifying existing thermodynamic data when attempting to produce *in situ* composites in multi-component systems or trying to synthesize single-phase compounds, an issue addressed in several ternary silicide systems [14, 136]. To confirm the phase boundary locations in a given multi-component system, careful microstructural examination and analysis is needed to complement phase identification from XRD. In fact, a microstructure purported to be single-phase $\text{Mo}_5\text{Si}_3\text{C}$ is presented by Nowotny et al. [18] (Figure 2.15), although the high magnification chosen, sintering porosity, and poor image quality make it difficult to say much about the single-phase nature of this particular composition.

Based on the height and width data of the $\text{Mo}_5\text{Si}_3\text{C}$ field obtained in this study and other work in the Mo-Si-C system [12, 19, 120], a revised schematic version of the Nowotny et al. Mo-Si-C isotherm in the near- $\text{Mo}_5\text{Si}_3\text{C}$ region is presented in Figure 3.23. This modified section shows the much smaller $\text{Mo}_5\text{Si}_3\text{C}$ single-phase region, as well as proper designation for Mo_5Si_3 , and Mo_2C (not MoC) present at 1600°C in agreement with the accepted Mo-C binary diagram [134]. It is postulated that the actual compositional range of the ternary phase may be even narrower than presented in this revised diagram, perhaps approaching a line compound.

3.4 Summary and Conclusions

Despite complications caused by uncertainties in the compositional range of $\text{Mo}_5\text{Si}_3\text{C}$ and challenges related to process optimization, nearly single-phase samples of $\text{Mo}_5\text{Si}_3\text{C}$ (Fig. 3.10 (a)) were produced by hot pressing blended powders at a nominal starting composition of 55.3Mo-34.7Si-10C. Three main processing routes were

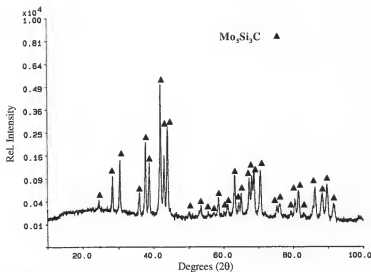


Figure 3.22 Pattern from XRD of sample CN 13 indexed as single-phase $\text{Mo}_5\text{Si}_3\text{C}$ based on JCPDS PDF 43-1199. Comparison with micrograph (Figure 3.19 (a)) showing definite multiphase microstructure indicates the hazards of relying solely on XRD for phase identification.

examined in this study, arc melting, powder blending followed by hot pressing, and hot pressing of mechanically alloyed powders.

While extended heat treatments might serve to homogenize arc melted samples, arc melting was deemed unsuitable because of difficulties incorporating carbon into the melt, concerns about Si loss, and thermally induced cracking. Arc melting of brittle materials susceptible to thermal shock is expected to be an ineffective means of producing samples for purposes other than phase equilibria and alloy screening studies.

Through hot consolidation of blended or MA powders, it was possible to produce $\text{Mo}_3\text{Si}_3\text{C}$ -containing specimens with varying compositions, phase distribution, and microstructural scale. Powder processing routes also alleviate the macrocracking and massive inhomogeneity observed in arc-melted specimens; however compositional control and contamination issues pose other challenges. Shifts in composition during the course of processing toward the Mo-rich corner of the Mo-Si-C isotherm were observed and are likely the result of reactions between silica on the starting Si-containing powders and carbon. Estimation of these shifts and attempts to correct for them were complicated by the uncertainties in oxygen content of the starting powders and the variation of oxygen content with type of siliceous compound.

A further result of reactions between carbon and silica was the formation of SiC-pore features in many of the hot pressed samples; the formation of silicon carbide and evolution of CO (g) was shown to be the most thermodynamically favored of potential silica reduction reactions. The presence of these reaction products points out one of the realities of powder processing silicide materials—other than circumventing powder oxidation through complex pre-processing such as powder etching or glove bag processing [9], one has to accept either the presence of amorphous silica particles in the consolidated samples or the byproducts of silica reduction by intentional deoxidant additions [64].

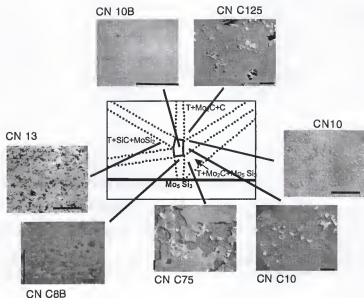


Figure 3.23 Representation of revised portion of Mo-Si-C 1600°C isotherm near the $\text{Mo}_5\text{Si}_3\text{C}$ single-phase field. The significantly reduced $\text{Mo}_5\text{Si}_3\text{C}$ compositional range is shown along with the proper designation for Mo_5Si_3 and the removal of phase fields involving MoC, which is not stable at 1600°C. The stoichiometry best approximating the T region is $\text{Mo}_{4.8}\text{Si}_{3.0.7}$. Scanning electron micrographs surrounding the section show typical microstructures of compositions approximately as indicated on the diagram. For micrographs (13), (10B), (10), and (8B) marker = 100 μm ; for (C125), (C10), and (C75) marker = 10 μm .

Phase identification through XRD and EPMA and quantitative compositional information from WDS and light element analysis of samples produced over a range of starting compositions indicates that the compositional range for $\text{Mo}_5\text{Si}_3\text{C}$ reported [18] on the accepted 1600°C Mo-Si-C isotherm is most likely a significant overestimation. The actual compositional range of the ternary compound probably encompasses only a few percent carbon at basically a fixed Mo:Si ratio. This obviously poses significant challenges to the production of single-phase microstructures especially in light of shifts in carbon and silicon content during powder processing. Given the ongoing interest in Mo-Si-X systems [26, 115, 116, 124, 149-154] for which the bulk of thermodynamic data and phase diagram information was developed over 40 years ago, it seems wise to verify relevant compositional ranges and phase equilibria before embarking on costly processing optimization or property determination studies.

CHAPTER 4 MECHANICAL BEHAVIOR OF $\text{Mo}_5\text{Si}_3\text{C}$ -BASED MATERIALS

4.1 Introduction

One of the primary reasons for studying ternary silicide compounds such as $\text{Mo}_5\text{Si}_3\text{C}$ is to investigate what effects, if any, their higher-symmetry crystal structures have on mechanical behavior, and how their mechanical properties compare with lower-symmetry binary compounds such as MoSi_2 and Mo_5Si_3 . Ideally, comparisons would be made between high purity single crystal materials, allowing for fundamental examination of issues such as elastic constants, operative deformation mechanisms, dislocation generation/mobility, and slip character. Unfortunately, production of homogenous single crystal silicides using float zone or Czochralski techniques is not trivial due to the aforementioned high vapor pressure of silicon [87]; losses of silicon and composition gradients would be especially problematic when trying to synthesize phases such as $\text{Mo}_5\text{Si}_3\text{C}$ having a narrow range of single-phase stability.

Polycrystalline materials are easier to synthesize, but greatly complicate assessment of intrinsic mechanical behavior and comparisons with other materials, particularly at elevated temperatures where grain size/grain boundary effects can dominate deformation. Because of this, it is desirable to be able to prepare samples at several different grain sizes. As detailed in the previous section, production of dense single-phase $\text{Mo}_5\text{Si}_3\text{C}$ samples was greatly complicated by discrepancies in the composition range of the phase as well as processing difficulties; nonetheless, dense, nearly-single phase specimens were produced at coarse ($\sim 20\text{ }\mu\text{m}$) and fine ($\sim 5\text{ }\mu\text{m}$) grain sizes. For the purposes of this study, it was decided that an examination of the mechanical behavior of these optimized samples at low and high temperatures would serve to establish some initial property values and possible

deformation mechanisms for the ternary phase. In addition, comparing the mechanical properties of $\text{Mo}_5\text{Si}_3\text{C}$ with other silicides would shed some light on the effectiveness of alloying to enhance deformability through increased crystal symmetry.

4.2 Experimental Procedure

4.2.1 Sample Characterization and Analysis

Samples for mechanical testing were produced from either hot-pressed blended powders or hot-pressed mechanically alloyed powders; as-hot pressed materials were disks either 16 mm or 32 mm in diameter, with the larger size preferred since it yields more mechanical testing samples per hot press run and is also large enough in diameter to allow for machining of standard 25 mm long bend test bars. Material stock used for mechanical property evaluations was characterized before testing so that the subsequent mechanical behavior could be correlated to sample microstructure and processing route. For all specimens characterized and tested, a minimum of 1 mm was ground from the as-hot pressed sample surfaces to completely remove the residual graphite foil. Unless otherwise noted, the experimental procedure for each characterization method was identical to that described in the previous chapter. For a first check of phases present, x-ray diffraction data was collected from a solid slice of the sample. A section of the testing stock was mounted in epoxy, ground flat, and polished to a 1 μm finish for microstructural analysis on the light optical and scanning electron microscopes, as well as phase identification and quantitative chemical analysis using WDS. From optical and scanning electron micrographs, the average grain size of specimens was determined using standard line intercept methods; image analysis was also used to determine Vol.% porosity and secondary phases. The bulk density of as-hot pressed samples was also measured using the previously described techniques (section 3.2.3.1).

4.2.2 Hardness Testing

Hardness measurements were done at room temperature using a bench mounted Buehler Micromet[®] 2 Microhardness Tester with a Vickers pyramidal diamond indenter at applied loads up to 1 kgf for a 15 sec dwell time. A calibrated eyepiece equipped with a micrometer was used to measure the lengths of the two perpendicular diagonals. A minimum of 15 indents were used to obtain average hardness values for a given sample; to avoid overlapping stress fields, care was taken to position indents such that their minimum separation was a minimum of two indents including any crack zones. To determine hardness values (HV) from indent lengths, the following expression was used,

$$HV = \frac{2P(0.9272)}{D^2} \quad (4.1)$$

where D is the average length of the two diagonals, and P is the applied load in kgf.

4.2.3 Indentation Fracture Toughness Measurements

Fracture toughness of the $\text{Mo}_5\text{Si}_3\text{C}$ compound was measured using indentation microfracture techniques; this method of fracture toughness testing was chosen for its simplicity and amenability to measurements on small samples. Five hardness indents were made at each of three different loads, and from each indent, hardness values were determined from Equation 4.1. Also measured for each indent was the length from the center of the indent to the end of the linear crack emanating from the corners of the indent, the induced crack length (c_o) [155]. Using the following expression,

$$K_{Ic} = A(E/H)^n P/c_o^{3/2} \quad (4.2)$$

where A and n are constants with values [156] of 0.016 and 0.5, E the elastic modulus of the material, and H the Vickers hardness. Because of limited data in the literature, toughness values were calculated with E for both Mo_5Si_3 (323 GPa [157]) and $\text{Mo}_5\text{Si}_3\text{C}$ (285 GPa [120]).

Values of K_{Ic} were derived from the slope of a linear fit to a P versus $c_o^{3/2}$ plot. For each indent, values for c_o were only recorded if they represented a well-defined crack

pattern, without excessive chipping or crack branching; as a measure of validity of the crack system, satisfaction of the criterion $c_0 \geq 2a$ [156], where $2a$ is the average diagonal length of the indent (D in Equation 4.1), was verified for each indent.

4.2.4 Elevated Temperature Compression Testing

To examine the flow behavior of $\text{Mo}_3\text{Si}_3\text{C}$ and its dependence on temperature, strain rate, and grain size, compression testing was done over a temperature range of 1000°C to 1300°C (approximately 0.5 to 0.66 T_m). Cylindrical (3 mm diameter x 5 mm height) compression specimens were cut as ~3.3 mm diameter right cylinders on a Brother HS 100 wire electro-discharge machine (EDM) from hot pressed disks either 31 mm in diameter by 7 mm thick or 16 mm diameter by 8 mm thick. Compression cylinders were machined such that the long axis (5 mm) was parallel to the pressing direction. The extra 0.3 mm tolerance in test specimen cylinder diameter was to compensate for subsequent grinding off of the EDM re-cast layer.

After machining, specimen surfaces were ground using SiC papers ranging from 240 to 800 grit; to ensure flat, parallel contact surfaces, a Starrett V-Block sample grinding holder was used to sequentially grind the ends of the specimens down in ~0.05 mm steps. The sides of the samples were ground down by rotating them manually on the grinding media. After grinding, a rotary diamond polishing wheel and 6 μm diamond slurry were used for final surface preparation. To estimate the degree to which the top and bottom contact surfaces were parallel, measurements of the cylinder height were made at three different points along the surfaces, and the typical height deviation was within $\pm 10 \mu\text{m}$.

An MTS Model 810 Materials Test System under servo-hydraulic control was used for compression testing. This system has a stainless steel jacketed, water cooled furnace chamber and OXYGON furnace. Using resistance-heated molybdenum elements under purified argon, the furnace is capable of sustaining temperatures to 1500°C . Two thermocouples placed approximately 2.5 cm from either side of the sample were used to monitor the temperature in the hot zone. Silicon carbide platens resting on graphite push

rods connect the hot zone to the load train; the graphite push rods thread into stainless steel actuator fittings at the top and bottom of the load train.

After coating sample contact surfaces with boron nitride high-temperature lubricant, the specimen was placed between the platens and a slight load (~ 5 kg) applied to stabilize the setup. The chamber was then purged and backfilled with purified argon several times, and left in the backfilled condition under flowing argon for the remainder of the test. During sample heating at typical heating rates of $16^{\circ}\text{C}/\text{min}$, the MTS was switched to load control to protect the specimen from damage due to expansion of the test fixtures. After a sufficient soak time at test temperature (~ 45 min) to allow for thermal equilibrium between the specimen and platens, the MTS was returned to displacement control for the remainder of testing. For all testing, a 2000 lb (907 kg) load cell was used with a ± 12.7 mm full scale displacement card.

Measurement of strain during testing was obtained indirectly from the displacement output of the servo-hydraulic low voltage displacement transducer (LVDT); the use of more accurate techniques, such as a hang-down extensometer or strain gauges, were made impractical by the small dimensions of the test setup and design of the furnace system. Load and stroke (displacement) data during testing was displayed graphically on a Hewlett Packard plotter with the raw data buffered and collected using LabTech Notebook software application. The data collection period used depended on the projected length of the test from 0.5 to 15 s.

For strain rate change tests, a minimum of three percent steady state deformation after yield was used as the criteria for changing strain rates. For the multiple strain rate tests, specimens were deformed out to strains approaching 0.30 (engineering). For both single and multiple strain rate testing, the viewport in the furnace chamber was used to monitor the specimen for evidence of barreling or off-axis deformation/shearing and if either of these features was observed, the test was halted. Care was taken to minimize the likelihood of these undesirable deformation artifacts through judicious system alignment,

good lubrication between specimen contact surfaces and platens, and careful sample preparation to ensure flat and parallel end surfaces. For both coarse and fine-grained samples, a combination of single and multiple strain rate tests covering strain rates ($\dot{\epsilon}$) of 1×10^{-5} to $9 \times 10^{-4} \text{ s}^{-1}$ were conducted at 1000, 1100, 1200, and 1300°C.

To correct the observed displacement values for machine compliance, load-displacement plots in the elastic regime were obtained with the SiC platens pressing against each other. Compliance data was obtained for 1000, 1150, 1200, and 1400°C at effective displacement rates corresponding to $\dot{\epsilon}$ of 1×10^{-4} and $1 \times 10^{-5} \text{ s}^{-1}$ for 5 mm tall specimens. From the reciprocal of the slope of the linear elastic load-displacement plots a machine compliance parameter as a function of load was determined at each temperature and strain rate of interest. After collection of raw load-stroke (position of crosshead relative to original position) data for a given test, the appropriate compliance correction was used to subtract the machine compliance from the raw displacement yielding an effective displacement more closely matching the actual specimen deformation.

To calculate true stress and true strain values from the load and displacement (compliance-corrected) output, the engineering stress (σ_{eng}) and strain (ϵ_{eng}) were first calculated using the following expressions,

$$\sigma_{eng} = P / A_0 \quad (4.3)$$

$$\epsilon_{eng} = \frac{\Delta l}{l_0} \quad (4.4)$$

where P is the applied load, A_0 is the original cross-sectional area of the specimen, Δl is the compliance-corrected displacement, and l_0 is the original height of the compression cylinder. From these expressions, it is possible to derive [86] the following expressions for true strain (ϵ_t) and stress (σ_t) which are better metrics of actual specimen deformation than their engineering counterparts, especially at high strains,

$$\epsilon_t = \ln(\epsilon_{eng} + 1) \quad (4.5)$$

$$\sigma_t = \sigma_{eng} (1 - \epsilon_t) \quad (4.6)$$

For single-strain rate tests, the flow stress was determined using the standard 0.2 % offset convention [86]; for multiple strain rate tests, a value from the steady-state region of the stress-strain curve was used as the flow stress

In order to examine flow behavior and strain rate sensitivity from strain rate change testing it is necessary to determine the true strain rate ($\dot{\epsilon}_t$) for a given imposed crosshead displacement rate, d [63]. This correction is necessary because the nominal displacement rates programmed into the controller before testing use the initial length of the sample in rate calculations which is only valid for the strain rate used at the outset of a given compression test. Defining the initial true strain rate as $\dot{\epsilon}_{t0}$, which is equivalent to d/l_0 , one can calculate $\dot{\epsilon}_t$ from:

$$\dot{\epsilon}_t = \dot{\epsilon}_{t0} \cdot \frac{1}{1 + \epsilon_{\text{eff}}} \quad (4.7)$$

To gain more insight into the high-temperature deformation mechanisms of $\text{Mo}_3\text{Si}_3\text{C}$, examination of post-deformation microstructures was conducted in the Phillips 420 transmission electron microscope at 120 kV using thin foils from several samples deformed an average of 8 %. Sample preparation techniques were similar to those previously described with a few minor modifications. First of all, slices for subsequent thinning were taken from the center of the compression specimen gage length to minimize the possibility of obtaining regions from the low-strain regions near the ends of the specimen [86]. In some cases it was necessary to attach the partially thinned foil using crystal mounting wax to a 100 μm thick copper supporting grid 3 mm in diameter containing a 1 mm x 2 mm oval cutout; this was necessary during the final stages of manual thinning using the Gatan disc grinder to prevent sample breakage and further edge erosion prior to dimpling and ion milling.

4.2.5 Four-Point Bend Testing

In order to compare the flow and fracture behavior under compression to that in a case involving a tensile loading component, several four-point flexure tests were performed

on $\text{Mo}_3\text{Si}_3\text{C}$ -containing samples. Testing was conducted at Ames Laboratory (Ames, IA 50011) using an MTS servo-hydraulic test system with a Centorr Testorr furnace attachment in a flowing nitrogen atmosphere. Rectangular parallelepiped specimens were tested at room temperature and 1200°C; for the 1200°C testing, the average heating rate was 21°C/min. Sample preparation was in accordance with ASTM Designation C1211-92 [158]. Sample configuration A from this standard was slightly modified to allow for easier sample handling; the sample dimensions used were $b=3$ mm, $d=2$ mm, and $L_f=25$ mm, where b is the width, d the depth, and L_f the length of the specimen. The direction of hot pressing was parallel to the 2 mm (depth) dimension of the specimens which also was the loading direction.

Bend-test specimens were initially cut from 31 mm diameter hot pressed disks using a low speed diamond saw and the surfaces ground with 240 grit SiC paper to remove any irregularities introduced during sectioning. Next, the end surfaces were ground flat using the V-Block and 180 grit SiC paper until the sample was 25 mm in length. Samples were then attached to a cylindrical 3.18 cm diameter stainless steel flat using crystal mounting wax. The flat was inserted into a stainless steel ring 2.54 mm tall with a 3.18 mm inner diameter and the height of the flat adjusted using a set screw until the surfaces of the test samples were just above the surface of the ring. By using the ring and flat with a series of SiC grinding papers from 240 to 600 grit it was possible to achieve the desired sample dimensions while maintaining the four longitudinal surfaces flat and parallel to within 0.02 mm. As a final step, a 45° chamfer was ground into the four longitudinal edges to remove any chipping or flaws along the edges that might otherwise cause premature failure of the specimens.

Both room temperature and elevated temperature testing was done using SiC bend fixtures having a lower support span of 20 mm and a loading span of 10 mm with 1 mm diameter SiC rollers used as contact points. Samples were tested at a constant crosshead displacement rate of 0.14 mm/min, which is equivalent to a nominal strain rate of 7.2×10^{-5}

s⁻¹ for the sample dimensions used. Displacement measurements were taken from both strain gauges affixed to the hydraulic ram and the LVDT. To calculate the strength (S) in four-point bending, the following expression was used,

$$S = \frac{3 \cdot P_f \cdot L}{4 \cdot b \cdot d^2} \quad (4.8)$$

where P_f is the load at failure and L the length of the support span. For calculation of the outer fiber stress, a similar equation was used,

$$\sigma_{of} = \frac{3P(L-s)}{2bd^2} \quad (4.9)$$

where P is the load and s the loading span.

Fracture surfaces of specimens which failed during bend testing were examined in the JEOL JSM 6400 scanning electron microscope at 15 kV. Both low and high magnification examination of the surfaces was done, with an emphasis on obtaining information about fracture mode, fracture path, and possible initiation sites.

4.3 Results and Discussion

4.3.1 Microstructural Characterization of Test Specimens

From each hot-pressed sample used as stock for mechanical test specimens, a section of material was removed and set aside for characterization so that the observed mechanical behavior could be correlated with the starting microstructures and processing variables. The majority of materials used for mechanical testing were similar in that they were close to single-phase $\text{Mo}_5\text{Si}_3\text{C}$ having less than 6.1 volume percent total second phase constituent. Samples also exhibited variations in grain size, porosity, and composition (Table 4.1). For samples processed by powder blending and hot pressing, the average grain size varied from about 14 to 23 μm , while the hot-pressed, mechanically-alloyed samples had average grain sizes of 6 to 8 μm .

One major difference observed between the samples produced from blended powders and those synthesized from MA powders was the presence of amorphous silica

particles in the MA samples (Figure 3.15, 3.16). Silica was typically visible in MA specimens as networks of globular particles $\sim 0.1 \mu\text{m}$ in diameter concentrated near grain boundaries and triple points; in no instance were non-crystalline phases detected during TEM examination of coarser-grain blended powder samples. The most logical explanation for the presence of silica in the consolidated MA samples is the increased surface area of the starting powders leading to significant and rapid oxidation of the powders after exposure to air. In fact, one batch of MA powders had such a rapid and exothermic oxidation upon exposure to air that they exhibited small-scale combustion. Because of the relatively large sample volume, the amount of free carbon in many of the silica-containing regions was probably insufficient to completely reduce the glassy phase during hot pressing. Evidence of a large composition shift as a result of C-SiO₂ reactions is seen particularly in sample LD6, where the shift toward the Mo-rich region of the Mo-Si-C isotherm was significant enough to move the final composition into the Mo₅Si₃C + Mo₂C + Mo₅Si₃ phase field.

Based on work on other silicides containing silica [9,35,159,160], it was expected that the deformation behavior of polycrystalline silica-containing Mo₅Si₃C would be affected, particularly at elevated temperatures. One of the main goals for the processing of samples for mechanical property evaluation was to be able to synthesize nearly-single Mo₅Si₃C over a range of grain sizes. Initially it was hoped that blended powder specimens having a grain size of approximately 10 to 20 μm would act as the lower end of the grain size range while samples produced from coarser ($\sim 95 \mu\text{m}$) starting powders would yield coarse grained ($>40 \mu\text{m}$) specimens. However, 32 mm diameter samples processed from these coarser powders displayed large cracks on the outer surfaces of the hot-pressed disks making them unsuitable for mechanical testing. Microcracks within consolidated samples were previously observed, although large surface cracks were not observed for smaller diameter specimens of any starting powder size.

The most plausible explanation for cracking of these larger grain specimens involves the previously mentioned issue of anisotropy in the coefficients of thermal

Table 4.1 Composition and microstructural characterization information for materials used for mechanical test specimens. Composition number (CN) corresponds to those assigned in Table 3.3. The $\text{Mo}_3\text{Si}_3\text{C}$ phase is designated by T; PBHP indicates powder blending and hot pressing, MAHP indicates mechanical alloying followed by hot pressing. Under "Type of Testing", C corresponds to compression testing and B corresponds to four-point bending.

Sample ID	CN	Proc. Route	Phase ID (Vol. %)	Grain Size, Avg. (μm)	Type of Testing	Notes
13IS2	I3	PBHP	T, SiC (6.1)	13.7 ± 1.4	C	
53C10	C10	PBHP	T, Mo_3C (3)	14.6 ± 1.6	C	
C10B5	C10B	PBHP	T	22.5 ± 2.7	C	SiC/pores < 1 Vol. %
LD1	C10B	PBHP	T	16.8 ± 2	B	> 1.2 % porosity
LD6	C10B	MAHP	T, Mo_3Si_3 (18.2), Mo_3C (2.3)	8.3 ± 0.9	C, B	6.1 Vol. % silica
LD8	C10B	MAHP	T, Mo_3C (0.4)	5.6 ± 0.5	C	2.1 Vol. % silica

expansion of the $\text{Mo}_3\text{Si}_3\text{C}$ compound. Recall that CTE information for $\text{Mo}_3\text{Si}_3\text{C}$ is lacking, although one could reasonably infer an anisotropic CTE for the ternary compound based on the reported CTE anisotropy for the isostructural Ti_3Si_3 compound [103] as well as the adjacent binary silicide Mo_3Si_3 [157]. Recall also from the relationship (e.g., Equation 2.4) between grain size, temperature gradient and thermal stresses upon cooling, the increase in stress associated with large grain size and temperature gradients. Based upon these factors, the 32 mm diameter, coarser grain specimens would be expected to have a higher propensity for thermally-induced cracking upon cooling than would smaller diameter, finer grain samples. As further evidence supporting CTE anisotropy in $\text{Mo}_3\text{Si}_3\text{C}$, it was observed that the density of microcracks tended to scale with the matrix grain size, with the finest grain size materials (e.g., LD8 in Table 4.1) basically crack-free after hot pressing, even in the largest samples.

The noticeable cracking in the large-grained samples as well as the limited availability of coarser starting powders were obstacles to production of large volume, large

grained materials for mechanical testing. Accordingly, the decision was reached to use samples processed by mechanical alloying and HP as the lower end of the grain sizes studied, and use the 10-20 μm grain size materials as the upper end (Table 4.1).

4.3.2 Hardness and Fracture Toughness Measurements

Hardness values for several of the materials produced in this study are presented in Table 4.2. The average hardness of the materials tested was 13.2 GPa (1340 HV) which is between the two values given in the literature for $\text{Mo}_5\text{Si}_3\text{C}$ of 12.1 GPa (1230 HV) [120] and 14.3 GPa (1460 HV) [18]; the range of hardness values reported for the ternary phase may be partially due to the different loads used, 10 kg for [120] and 50 g for [18]. The hardness is marginally higher for the finer grain size materials in Table 4.2, although the reasons for this are unclear. It is possible that elastic anisotropy of the hexagonal $\text{Mo}_5\text{Si}_3\text{C}$ phase could be partially responsible for the variation in hardness with grain size, with local variations in elastic moduli with grain orientation. For coarse grain samples, the typical indent diagonal was twice the average grain diameter, while for the fine grain materials the average diagonal crossed more than seven grains, implying that elastic anisotropy effects would be more pronounced in the large grain material since each indent sampled fewer grains. Further evidence for elastic anisotropy was the slight asymmetry of some indents, presumably due to local variations in elastic constants from grain to grain.

As shown in Figure 4.1, indentation caused cracks to radiate from the corners of the hardness indent into the matrix; in this particular sample, some cracks branch out from the long edges of the indent, i.e., not only from the four corners. The position of the indent relative to a particular set of grains and variations in grain size and shape may account for this observation; the crack emanating from the bottom corner of the indent is straight and well-defined as it runs through a larger grain, while the more diffuse transgranular and intergranular cracking seen at the right corner of the indent is in a region with a higher concentration of smaller grains which provide a lower-energy crack path.

Table 4.2 Vickers microhardness values for $\text{Mo}_3\text{Si}_3\text{C}$ -based materials produced in this study. All values are for 1 kg load at a 15 s loading time.

Sample ID	Hardness (GPa)	Standard Deviation (\pm GPa)
53C10	12.82	0.22
C10B5	13.30	0.16
LD1	13.05	0.23
LD6	13.25	0.18
LD8	13.78	0.22



Figure 4.1 Light optical micrograph (400x) using differential interference contrast showing hardness indent in $\text{Mo}_3\text{Si}_3\text{C}$, sample 53C10. Note the mixture of transgranular and intergranular cracks surrounding the indent.

Based on the presence of cracks surrounding hardness indents at room temperature, it was anticipated that $\text{Mo}_3\text{Si}_3\text{C}$ would exhibit fracture toughness values akin to an intermetallic or ceramic rather than a ductile metal. Using the semi-empirical indentation microfracture method of K_{Ic} determination developed for brittle materials [155], toughness values of $2.40 \text{ MPa}\cdot\text{m}^{1/2}$ or $2.56 \text{ MPa}\cdot\text{m}^{1/2}$ were obtained for sample 53C10 depending on which value of E was used (i.e., $\text{Mo}_3\text{Si}_3\text{C}$ or Mo_3Si_3). Although the differences in toughness with E value chosen are minor, this issue could be further clarified by direct determination of E/H ratios by using a Knoop indenter [161].

Note that the indents used to derive fracture toughness values had better defined crack patterns than shown in Figure 4.1, with sets of symmetric cracks radiating from the corners of the indents. For indents with well-defined crack patterns, plotting load versus crack length resulted in a linear relationship and K_{Ic} values were derived from the slope of this line, per Equation 4.2. However, the non-zero intercept of this plot or, alternatively, the positive slope of a plot of load against crack length-normalized load (Figure 4.2) indicates the presence of a tensile residual stress in the sample, presumably because of the CTE anisotropy-induced thermal stresses upon cooling.

One issue not directly investigated is the effects of second phase content and distribution on the toughness of $\text{Mo}_3\text{Si}_3\text{C}$ -based materials. For example, samples containing distributions of SiC or Mo_2C particles might exhibit higher toughness owing to crack deflection or crack bowing around the carbides, although the nature of the carbide-matrix interface and the residual stress state surrounding the particles would also affect the magnitude of any toughness improvement [25]. A recent study reported little change in toughness with small Mo_2C additions to $\text{Mo}_3\text{Si}_3\text{C}$ [120]. Another issue that is unclear is what effects, if any, the presence of vitreous silica particles have on the toughness of mechanically alloyed $\text{Mo}_3\text{Si}_3\text{C}$; while the influence of silica on high temperature deformation behavior of polycrystalline silicides has been the focus of

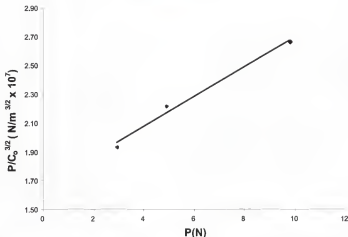


Figure 4.2 Plot of applied indenter load against crack length-normalized load for $\text{Mo}_5\text{Si}_3\text{C}$ sample 53C10. The empirical relationships for indentation-based fracture toughness are based on a plot of this type having a zero slope [Anstis, 1981 #269]; the positive slope in this case is indicative of a tensile residual stress.

considerable work, the effect of silica on the toughness of silicides has received little attention other than the supposition that silica at grain boundaries and triple points may act as flaw initiation sites [9]. Based on the following expression for critical stress intensity in the presence of a semi-elliptical surface flaw in a material having local residual stress,

$$K_{Ic} = 1.65\sigma_f\sqrt{c} \quad (4.10)$$

where σ_f is the fracture stress (~ 300 MPa) and c is the equivalent semi-circular flaw size, the critical flaw size in $\text{Mo}_5\text{Si}_3\text{C}$ is estimated to be on the order of $25 \mu\text{m}$. When observed in $\text{Mo}_5\text{Si}_3\text{C}$ -based samples, the majority of SiO_2 particles are less than $1 \mu\text{m}$ in size, thus other larger voids and defects likely have more influence on ambient temperature fracture susceptibility than does the presence of silica.

4.3.3 High-Temperature Deformation Behavior in Compression

Compression testing was chosen as the primary method for examining the elevated temperature deformation behavior of $\text{Mo}_3\text{Si}_3\text{C}$ -containing materials for several reasons. First of all, the relatively small specimens used for compression testing are better suited to the size of samples possible through hot pressing than are typical tensile specimens. The less intensive machining required of compression specimens is also desirable since it results in lower chance of damage due to handling. Also, a greater degree of deformation is typically available under compression than under tension, since the compressive stress state tends to suppress cracks and limit their propagation and compression testing is less sensitive to surface flaws. Availability of a compression testing apparatus capable of 1500°C and the large amount of data in the literature on compressive behavior of silicides were further reasons to consider compression testing as the primary mechanical testing method.

For a typical compression test, the sample displayed a linear elastic region, a transition region, and a steady-state region of plastic flow. In most cases the onset of the initial linear elastic regime was precluded by a regime in which the stress-strain curve was parabolic in shape; this "tail" is thought to be related to system alignment and typically did not persist after 1 % strain was reached. Appendix B contains several representative compressive stress-strain curves. Considering first the behavior of larger grain ($23\text{ }\mu\text{m}$) $\text{Mo}_3\text{Si}_3\text{C}$ -based materials, a steady drop in flow stress with test temperature from 1000 to 1300°C was observed (Figure 4.3). Note the relatively high strain rate dependence of the flow stress for $\text{Mo}_3\text{Si}_3\text{C}$, more so than for the flow stress of $40\text{ }\mu\text{m}$ grain size MoSi_2 shown in Figure 4.3.

More insight into potential elevated temperature deformation mechanisms can be obtained by displaying the true flow stress as a function of true strain rate on a log-log plot (Figure 4.4). Using a simplified form of a constitutive relationship for polycrystalline deformation at elevated temperature,

$$\dot{\epsilon} = k\sigma^n \quad (4.11)$$

where k is a material specific constant and n the stress exponent, one can obtain the value of n from the slope of a stress-strain rate plot displayed on logarithmic axes. From this plot, the stress exponent value remains basically constant at $n=3.2$ over the range of test temperatures; since n is usually indicative of the controlling deformation mechanism, the fixed n for these large-grain samples over the range of test temperatures indicates that a similar mechanism (or mechanisms) is operative.

Finer grain size samples ($6\text{ }\mu\text{m}$) also exhibited a drop off in flow stress with increasing temperature (Figure 4.5), although it was more rapid than for the $23\text{ }\mu\text{m}$ grain size materials. The log stress-log strain rate plot for the $6\text{ }\mu\text{m}$ grain size samples was considerably different as well, with the n values no longer constant with test temperature as shown in Figure 4.6. Before further analyzing the possible reasons for the differences in observed flow behavior between the coarse and fine grain $\text{Mo}_3\text{Si}_3\text{C}$, it is worthwhile to briefly review some of the characteristics and phenomenological equations for polycrystalline deformation at elevated temperatures.

The commonly accepted mechanisms for deformation of polycrystalline materials at elevated temperatures ($0.4\text{--}0.5\text{ }T_m$) can be grouped generally as either lattice or boundary-related [162]. In higher stress regimes, lattice mechanisms such as dislocation glide and climb are usually favored, with the glide-controlled mechanisms associated with $n \approx 3$ while dislocation-climb controlled mechanisms have $n \approx 4.5$ [163,164]. An example of this situation is dislocation creep controlled by the climb of edge dislocations:

$$\dot{\epsilon} = \frac{ADGb}{kT} \left(\frac{\sigma}{G} \right)^5 \quad (4.12)$$

where A is a material-specific constant, D the diffusivity, G the shear modulus, k the Boltzmann constant, and T the absolute temperature.

At higher temperatures, lower stress levels, and finer grain sizes, mechanisms controlled by boundary processes such as grain boundary diffusion and boundary sliding

are more likely with $n \approx 1-2$ [62,63,163,164]. For example, the well-known Coble relationship describing deformation controlled by stress-driven grain boundary diffusion is given by:

$$\dot{\epsilon} \approx \frac{50\sigma D_{gb} b^4}{kTd^3} \quad (4.13)$$

where D_{gb} is the grain boundary diffusivity and d the grain diameter. The grain size exponent of 3 is indicative of the strong grain size dependence common to boundary mechanisms. Grain boundary sliding ($n \approx 1-2$) is considered to be a non-independent deformation mechanism since the action of shearing displacement between grain boundaries necessitates accommodation by the simultaneous operation of other mechanisms such as diffusional flow or dislocation climb. The presence of an amorphous phase at the grain boundaries can act to accelerate creep deformation by boundary sliding at temperatures above the softening point of the glass. For example, the Coble relationship can be modified to take into account the presence of a liquid phase at the boundaries,

$$\dot{\epsilon} \approx \frac{A\sigma\Omega V_l C_l D_l}{kTd^2} \quad (4.14)$$

where A is a constant, Ω is the atomic volume, V_l is the volume fraction liquid phase, C_l is the solubility of the rate controlling element in the glassy phase, and D_l is the diffusivity in the liquid phase [63]. In the absence of a glassy phase, mechanisms such as the Nabarro-Herring or Coble processes still require the operation of grain boundary sliding to prevent the separation of grains [164]. When multiple mechanisms are operational, the slowest mechanism is the controlling one for mechanisms that operate in series, while the fastest mechanism is rate controlling for parallel, independent mechanisms [164].

In powder-processed ceramics and silicon-containing materials such as MoSi_2 , the presence of a glassy phase along the grain boundaries has definite implications for the enhancement of boundary sliding and diffusion mechanisms. For cases where the

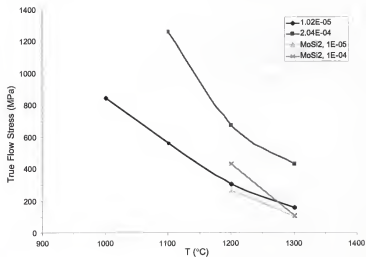


Figure 4.3 Compressive flow stress versus temperature plot for the 23 μm grain size $\text{Mo}_x\text{Si}_3\text{C}$ sample C10B5. Values presented are for strain rates of 1×10^{-3} and $2 \times 10^{-4} \text{ s}^{-1}$. Also shown are flow stress data at 1200 and 1300°C for a high-purity, hot isostatically-pressed MoSi_2 having an average grain diameter of 40 μm [165].

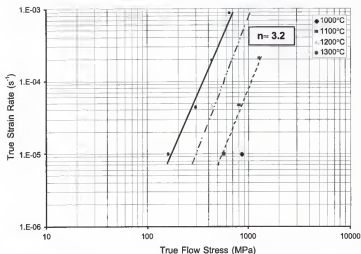


Figure 4.4 Plot of true strain vs. true flow stress for $\text{Mo}_5\text{Si}_3\text{C}$ (grain size $\sim 23 \mu\text{m}$) in compression over a temperature range of 1000 to 1300°C . A linear fit to the data at the test temperatures gives a common slope equivalent to a stress exponent (n) of ~ 3.2 .

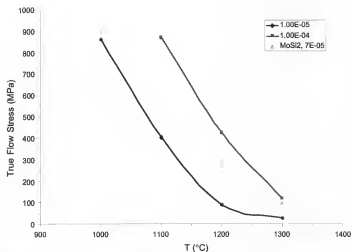


Figure 4.5 Compressive flow stress versus temperature data for 6 μm grain size $\text{Mo}_5\text{Si}_3\text{C}$ sample LD8. Values are presented for initial strain rates corresponding to 1×10^{-5} and 1×10^{-4} . Also included are compressive flow stress data for polycrystalline MoSi_2 having a grain size of 10 μm [76].

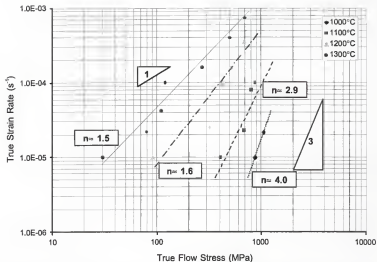


Figure 4.6 Plot of true strain vs. true flow stress for Mo_5Si_3C ($6\ \mu m$ grain size) in compression over the temperature range 1000 to 1300°C. A linear fit to the data at the test temperatures shows slopes decreasing with increasing temperature as the stress exponent (n) varies from 4.0 to 1.5.

intergranular phases wet the boundaries there is a rapid degradation in strength above the softening point of the viscous glass phase [6]. A simple model representing this case is that of Pharr and Ashby [166], wherein the lubricating action of a glassy phase at the grain boundary allows for easier sliding of grain boundaries. From their model, an applied stress results in creep deformation as follows,

$$\dot{\epsilon} = 0.333 \left[\frac{w}{w+d} \right] \left(\frac{\sigma}{\eta} \right) \quad (4.15)$$

where w is the grain boundary thickness and η is the viscosity of the glassy phase.

The situation is less clear in the case of MoSi_2 , in which silica does not appear to wet the grain boundaries and conflicting information has been reported on both the distribution and interfacial characteristics of silica [63].

The aforementioned deformation mechanisms and their characteristic stress exponents are presented with the caution that the majority of these phenomenological relationships were developed for ductile metals and/or idealized systems, so for materials which are brittle at ambient temperatures such as $\text{Mo}_5\text{Si}_3\text{C}$, one would not necessarily expect the same correlations to hold true. With that caveat, possible explanations can now be considered for the controlling deformation mechanisms in polycrystalline $\text{Mo}_5\text{Si}_3\text{C}$. One of the most readily apparent features is the significant difference in flow stress behavior between the coarser and finer grain size materials (Figure 4.7). At 1000°C , the fine grain material actually has a slightly higher flow stress than the $23\text{ }\mu\text{m}$ grain size samples. However, above 1000°C the flow stress of the fine grain material decreases much more rapidly than its coarser grain counterpart, with the ratio of the flow stresses at a strain rate of $1 \times 10^{-5} \text{ s}^{-1}$ for fine and coarse grain $\text{Mo}_5\text{Si}_3\text{C}$ dropping to less than 0.2 at 1300°C . From this plot, it seems likely that diffusional mechanisms, with their strong temperature dependence play a strong role in the deformation of the finer grain material. Noting the rapid drop in flow stress ratio between 1200 and 1300°C for samples tested at $\dot{\epsilon}$ of 1×10^{-4} ,

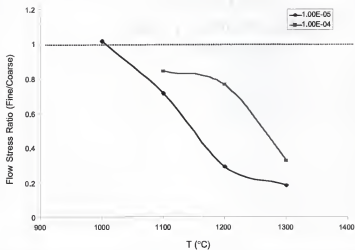


Figure 4.7 Ratio of fine grain and coarse grain flow stress as a function of temperature for $\text{Mo}_5\text{Si}_3\text{C}$ -based materials.

the presence of silica in the 6 μm grain size samples may drive the decrease in stress above 1200°C as the glassy phase softens and coalesces.

Comparing the variation of stress exponent (n) from 1100 to 1300°C for the two different grain sizes (Figure 4.8) sheds more light on the possible deformation mechanisms in $\text{Mo}_5\text{Si}_3\text{C}$. As previously noted, the 23 μm grain size material has a basically fixed $n=3.2$ over the temperatures considered, which is typically associated with deformation controlled by dislocation glide. Conversely, the n values for the finer grain material are not constant, decreasing with increasing temperature from 2.9 at 1100°C to 1.5 at 1300°C, indicative of a transition in mechanisms from a dislocation glide type toward a diffusional flow/boundary sliding type. Most likely multiple, competing mechanisms are active in both the fine and coarse grain materials. Since the larger grain size materials in this study are actually small compared with arc-melted samples ($\sim 100 \mu\text{m}$) or hot pressed specimens processed from coarse powders at high temperatures/long times ($\sim 40 \mu\text{m}$), grain boundary sliding is most likely occurring concurrently with dislocation climb/glide [167].

As the temperature increases, the bulk and grain boundary diffusivities increase, providing an energetically more favorable route for accommodation of grain boundary sliding in the fine grain materials as compared with dislocation glide/climb in the complex D8_8 structure. As already mentioned, it is also possible that the amorphous silica particles in the MA samples start to soften at higher temperatures ($T > 1200^\circ\text{C}$) and those present at or near grain boundaries and triple points further enhance grain boundary sliding accommodated by diffusional flow. In addition to the possibility of the lower-viscosity silica accelerating grain boundary sliding, regions of MA samples having high concentrations of silica particles appear to be locally refined (Figure 3.15), with grain diameters in the 1-2 μm range, which would further increase the propensity of these materials to deform via boundary mechanisms.

In order to discern more clearly between the different possible boundary mechanisms in $\text{Mo}_5\text{Si}_3\text{C}$, it would be necessary to determine the grain size exponent, p ,

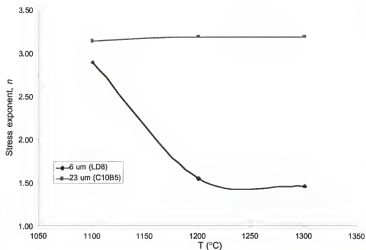


Figure 4.8 Plot of stress exponent, n , as a function of temperature for $\text{Mo}_3\text{Si}_3\text{C}$ -based materials of different grain sizes. The significant drop in n above 1100°C for the fine grain material is consistent with a transition in deformation mechanism from dislocation glide/climb to grain boundary sliding with diffusional flux accommodation and a possible contribution from softening of amorphous silica particles.

which has values of 3, 2, and 1 for the Coble, Nabarro-Herring, and boundary sliding processes, respectively [163]. To do this would require the synthesis of a minimum of one more sample having a grain size different from 6 or 23 μm ; all three grain sizes would have to be tested under constant load, from which a plot of strain rate vs. the reciprocal of grain size at constant stress and temperature would give p [6].

Information on the elevated-temperature deformation mechanisms of silicides other than MoSi_2 and its composites is quite limited. Materials such as Ti_3Si_3 , Mo_5Si_3 , and Cr_3Si have been tested under compressive creep conditions and exhibit stress exponents on the order of 2 to 3 [6,168]. As for MoSi_2 -based materials, stress exponents of 1 to 5 are typical [6,62,63,167], with a strong grain size dependence seen for the disilicide at both high and low stresses for grain sizes below 30 μm . As might be expected, silicide materials showing the best strength retention and lowest creep rates at elevated temperature are those with a combination of large grain size ($\sim 40 \mu\text{m}$) and minimal glassy silica inclusions [169]. Direct comparisons between $\text{Mo}_5\text{Si}_3\text{C}$ and other silicides are complicated by differences in grain size, strain rate, strain history, and stress level (i.e., creep testing), although the same general trends are observed, with the highest flow stress materials (in compression) being those with larger grain sizes and no silica.

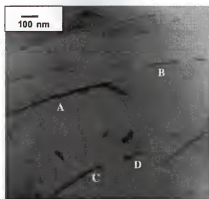
To more thoroughly assess the post-deformation microstructures of $\text{Mo}_5\text{Si}_3\text{C}$ -based specimens after compression testing, transmission electron microscopy (TEM) was used to investigate dislocation density, substructures, and slip character. Initial examination of deformed specimens revealed that a low density of dislocations was present in materials tested at 1000 and 1100°C while dislocations were basically absent in the samples tested at 1300°C; this supports the concept of deformation modes in $\text{Mo}_5\text{Si}_3\text{C}$ changing with temperature from dislocation glide with boundary sliding to diffusional flow with boundary sliding.

During initial dislocation analysis using standard diffraction contrast techniques [170], the choice of diffraction vectors (g) was based on the assumption that the most

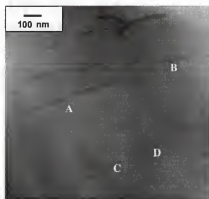
likely operative slip system in the hexagonal $\text{Mo}_3\text{Si}_3\text{C}$ phase would be the system $\langle 0001 \rangle \langle 11\bar{2}0 \rangle$. Attempts to obtain the expected dislocation contrast for the diffracting conditions $\mathbf{g} \cdot \mathbf{b} = 0$ (dislocations in contrast) and $\mathbf{g} \cdot \mathbf{b} \neq 0$ (out of contrast) proved difficult and, in fact, the dislocations that were visible appeared to alternate contrast at \mathbf{g} vectors orthogonal to what would be expected for $\mathbf{b} = [11\bar{2}0]$, implying an operative slip vector 90° to $\langle 11\bar{2}0 \rangle$. After reexamining the D8_8 structure of $\text{Mo}_3\text{Si}_3\text{C}$ (Figure 2.15), it became apparent that the $\langle 11\bar{2}0 \rangle$ directions were not the closest-packed representing a unit translation between like atoms. Primarily due to the ABC stacking of Si on $6(g_h)$ sites and the c/a ratio less than one, it was determined that the shortest repeat vector in the D8_8 cell is the c -axis giving a Burgers vector 0.505 nm in length.

Based on this revised assumption of c -axis slip, samples were again analyzed in the TEM. Figure 4.9 (a), a bright field (BF) image taken with $\mathbf{g} = 0002$ clearly shows several dislocations having strong contrast. When this same region is imaged with $\mathbf{g} = 11\bar{2}0$ (Figure 4.10) the dislocations are either absent or display very little contrast. Assuming Figure 4.9 (b) represents a $\mathbf{g} \cdot \mathbf{b} = 0$ situation, slip vectors equivalent to $\langle 0001 \rangle$ satisfy this condition, confirming what was suggested by the atomic arrangement of the D8_8 structure. While a more detailed analysis might determine if $c[0001]$ slip is the only operative slip vector in $\text{Mo}_3\text{Si}_3\text{C}$ at the temperatures tested, it does appear to be the dominant one. In addition, no faulted regions from twins, anti-phase boundaries, or stacking faults were visible in the TEM, indicating that alternate deformation modes or super-dislocations were not involved in the samples analyzed. These features have been reported in single crystal and polycrystalline silicide materials such as MoSi_2 and $\text{Mo}(\text{Si}, \text{Al})_2$ [129, 171].

Slip along $c[0001]$ has negative implications for the potential plastic deformation of polycrystalline $\text{Mo}_3\text{Si}_3\text{C}$, consistent with the observed brittle behavior under indentation and bending as well as its low fracture toughness. If a system of the type $\{hki0\}\{0001\}$ is



(a)



(b)

Figure 4.9 Bright field (BF) images near a beam direction $\mathbf{B} = [1\bar{1}00]$ for dislocations (e.g., A-D) in sample 13IS2 compressed to 10% strain at 1200°C. (a) Image taken at $\mathbf{g}=0002$ with dislocations in contrast. (b) Image at $\mathbf{g}=11\bar{2}0$ with dislocations out of contrast, consistent with $\mathbf{b}=c[0001]$.

the only mode of deformation available, this represents only two independent slip systems [172], considerably less than the five required by the von Mises criterion [85].

Additionally, the large b and assumed semi-covalent nature of the bonding in $\text{Mo}_5\text{Si}_3\text{C}$ imply a very high Peierls barrier to the generation and motion of dislocations [173].

According to the literature, c -axis slip has not been reported as the primary slip mechanism for any other intermetallic compounds; the deformation mechanisms of other hexagonal structures that are observed in ordered materials (e.g., C40 , D0_{19}) have been studied to some extent, with basal slip and $b=\langle 11\bar{2}0 \rangle$ the most common mechanism reported [129,143,174]. A study of the D8_8 silicide Ti_5Si_3 described slip occurring on $(\bar{1}101)$ and $(2\bar{3}11)$ planes at elevated temperatures, implying $b=\langle 11\bar{2}0 \rangle$, but the analysis is quite limited [41]. Two ceramic materials, $\beta\text{Si}_3\text{N}_4$ and BeO , do slip along $[0001]$; $\{10\bar{1}0\}[0001]$ is the primary mechanism in hexagonal silicon nitride at temperatures above $\approx 1600^\circ\text{C}$ [175], while BeO primarily slips on $(0001)\langle 11\bar{2}0 \rangle$, although $\{10\bar{1}0\}[0001]$ slip occurs above $0.5 T_m$ [162]. In addition, TiB_2 , HfB_2 , and tungsten carbide all exhibit primarily prismatic slip with both $b=[0001]$ and $b=\langle 11\bar{2}0 \rangle$ because of $c/a \approx 1$ [176].

4.3.4 Four-Point Flexure Testing of $\text{Mo}_5\text{Si}_3\text{C}$

To supplement to the information obtained from compression testing, several bend bars from coarse (LD1) and fine (LD6) samples were tested in four-point flexure at both room temperature and 1200°C . The results of the bend tests are summarized in Figure 4.10. For the finer grain material (LD6-2) tested at room temperature (RT), a bend strength of 266 MPa was recorded, with failure occurring with basically zero deflection. At 1200°C , a sample of the same material (LD6-3) displayed a yield stress of approximately 430 MPa and exhibited a deflection of almost 0.9 mm before the test was halted. The coarser grain material (LD1-1) failed at 1200°C after a minimal amount of deflection at a stress of 484 MPa. Room temperature bend testing was planned for this larger grain material as well, but all of the remaining specimens failed during sample preparation and handling.

Some representative fracture surfaces examined in the scanning electron microscope are presented in Figures 4.11 and 4.12. For the larger grain material (Figure 4.11), the fracture morphology appears to change from mixed transgranular and intergranular fracture at RT to predominately intergranular fracture at 1200°C. Figure 4.11 (a) indicates areas of surface connected porosity which may have acted as fracture initiation sites. The finer grain size specimen (LD6-2) containing ~25 Vol.% secondary phases which was fractured at RT (Figure 4.12) shows a mixture of intergranular and transgranular fracture, including some river or twist markings visible in a high-silica region (Figure 4.12 (b)).

The goal of the bend testing was not to establish bend strength values for $\text{Mo}_3\text{Si}_3\text{C}$ nor thoroughly assess the effects of features such as grain boundaries and second phases on fracture behavior, goals which would require the testing of many more samples of each grain size (~30) along with proper Weibull analysis to quantify the effects of flaw distribution on strength [177]. Rather, the aim of the bend testing was to obtain a rough idea of the effects of grain size and temperature on strength and fracture behavior for comparison with what was observed during compression testing. With this in mind, some general observations are possible, with the most obvious being the significant disparity in deflection for the different grain sizes tested at 1200°C. The substantial deflection of the finer grain size material seems to confirm the behavior observed in compression testing, where the smaller grain material deformed very easily at 1200°C and above as a result of grain boundary sliding.

Less obvious is whether the fracture mode is actually varying with temperature in the coarse-grain specimens, where a transition from mixed transgranular/intergranular to primarily intergranular fracture apparently occurs between ambient and 1200°C. It is possible that the variation in fracture type reflects a distribution of grain sizes in the material and not a temperature effect, with more refined regions predisposed to fracture along grain boundaries while coarser areas failing transgranularly, as observed in other brittle materials

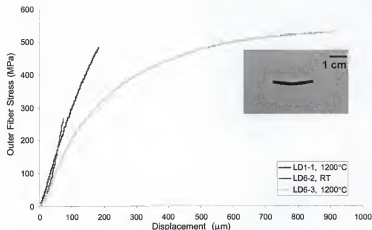


Figure 4.10 Stress-displacement curves for 17 μm (LD1) and 8 μm (LD6) grain size specimens testing in four-point bending at an effective strain rate of $7.2 \times 10^{-3} \text{ s}^{-1}$. The photograph is sample LD6 tested at 1200°C showing the significant deformation (~0.9 mm) occurring without failure in the finer grain MA material, presumably due to grain boundary sliding.

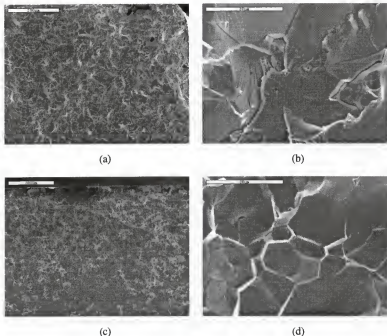
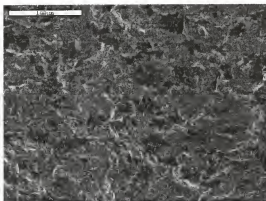
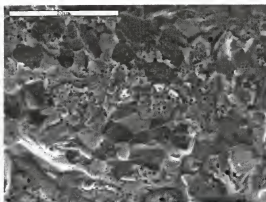


Figure 4.11 (a) Fracture surface (scanning electron image (SEI)) near a corner of a coarser grain ($17\text{ }\mu\text{m}$) grain size specimen which failed at room temperature during sample preparation. (b) Fracture surface of same sample (SEI) showing twist/river markings and mixed intergranular/transgranular fracture. (c) Fracture surface (SEI) of a $17\text{ }\mu\text{m}$ grain size specimen fractured under four point bending at 1200°C , showing surface connected porosity near the upper surface. (d) Higher magnification of (c) clearly showing intergranular fracture (SEI).



(a)



(b)

Figure 4.12 (a) Fracture surface (SEI) of 8 μm grain size $\text{Mo}_5\text{Si}_3\text{C}$ -based material which failed at 266 MPa in four-point flexure at RT; darker contrast regions are most likely Mo_5Si_3 , which is the major second phase constituent of this mechanically alloyed and hot-pressed sample. (b) Fracture surface (3000x, SEI) of same specimen showing a mixture of transgranular and intergranular fracture; as in (a), darker regions are Mo_5Si_3 , while the fine, bright phase near the center of the micrograph is Mo_2C , and the finely distributed black particles are SiO_2 .

[162]. However, intergranular fracture seemed to be consistent across the fracture surface of the 1200°C specimen and the variation in grain size was only on the order of 10 %.

Another possibility is that some minor grain boundary displacement occurred during the limited deflection prior to failure, weakening the boundaries and facilitating a change in fracture path to intergranular. With increasing temperature, a transition from transgranular to intergranular fracture mode in polycrystalline materials has been linked to the combined action of grain boundary sliding and cavitation at the boundaries, occurring preferentially at discontinuities such as interphase boundaries, triple points, ledges, and hard particles [164]. For polycrystalline MoSi_2 , studies indicate that intergranular fracture is also the prevailing fracture mode at higher temperatures, with the fine grain size, higher-oxygen materials apparently yielding in bend tests at $T > 1200^\circ\text{C}$ [77,90,178].

4.3.5 Mechanical Property Comparisons with Other Silicide Materials

Several room temperature and elevated temperature mechanical properties obtained for $\text{Mo}_2\text{Si}_3\text{C}$ in this study are compared with the properties reported for other binary and ternary silicides in Table 4.2 along with comparable data for other silicide materials evaluated for high-temperature structural applications. At ambient temperatures, the hardness of $\text{Mo}_2\text{Si}_3\text{C}$ is higher than the majority of the other silicides listed in Table 4.2. The reasons for this elevated hardness are unclear, although the very high resistance to dislocation motion in the D8_3 structure of $\text{Mo}_2\text{Si}_3\text{C}$ is a likely contributor. The fracture toughness of $\text{Mo}_2\text{Si}_3\text{C}$ is in the same range as most of the other silicides ($\sim 3 \text{ MPa}\cdot\text{m}^{1/2}$); the only material which is notably higher than this range is a cast Mo-14Si-10B alloy containing more than 25 Vol.% of a molybdenum solid solution phase [115]. Despite considerable efforts, the toughness values of silicides remain basically an order of magnitude below the levels ($\sim 20 \text{ MPa}\cdot\text{m}^{1/2}$) which are considered a minimum for structural applications based on current design guidelines [22].

Table 4.2 Room temperature and high-temperature mechanical properties for $\text{Mo}_5\text{Si}_3\text{C}$ and other polycrystalline silicide materials. All materials are powder processed through HP or HIP. Mode refers to type of test, compression (C) or bending (B). Temperatures are in $^{\circ}\text{C}$ and strain rates are s^{-1} . Grain size (GS) is given in μm , Vickers hardness (HV) values are in GPa, and toughness (K_{IC}) is in $\text{MPa}\cdot\text{m}^{1/2}$. $\text{Mo}_5\text{Si}_3\text{C}$ is denoted by T.

Material	GS	HV	K_{IC}	Stress at Temperature			Ref.
				Mode	MPa	T / ϵ	
T+ Mo_5C	15	12.8	2.5			RT	this work
T+ Mo_5Si_3 + SiO_2 + Mo_5C	8	13.3		B	266	RT/7E-5	this work
T	17	13.1		B	484	1200/7E-5	this work
T+ Mo_5Si_3 + SiO_2 + Mo_5C	8			B	430	1200/7E-5	this work
T	23	13.3		C	580	1200/1E-4	this work
T+ SiO_2 + Mo_5C	6	13.8		C	430	1200/1E-4	this work
T	23			C	160	1300/1E-5	this work
T+ SiO_2 + Mo_5C	6			C	30	1300/1E-5	this work
$\text{Mo}_5\text{Si}_3\text{C}$ + SiO_2		12.1	3.3	B	485	20/1.7E-4	[120]
MoSi_2	20	8.6				RT	[66]
MoSi_2			4			RT	[9]
MoSi_2	20			B	200	1200/3E-5	[94]
MoSi_2	10			C	275	1200/7E-5	[76]
Mo_5Si_3	15	12	2.9	C	140	1310/1E-6	[101,102]
Mo_5Si_3 +B	15	11.8					[102]
Mo_5Si_3 +B	4			C	138	1310/1E-6	[101]
Mo-14Si-10B			7-10	B	463	RT	[115]
Mo_5Si_3 +C	15	12.8	3.4				[102]
MoSi_2 -5SiC	40			B	310	1300/2E-4	[63,169]
MoSi_2 -20SiC	6	12.5	3.5	B	20	1300/2E-4	[63,169]
Cr_3Si				B	154	1200/1E-6	[75]
TiSi_2	33	8.5	1.9	C	17	1300/1E-4	[179]
Ti_3Si_2	35	9.5	2	C	250	1300/1E-4	[80]

The RT bend strength of $\text{Mo}_5\text{Si}_3\text{C}$ obtained in the current work is considerably lower than the only other value reported [120]. However, as already discussed, the bend strengths obtained in the current work are highly speculative based on the limited number of specimens tested; the strength obtained by [120] was for three-point bending, which tends to give higher strengths compared with four-point flexure since less of the material is subjected to loading [162]. Without knowing more about the surface condition and flaw distribution for the various silicide samples presented in this table, direct comparison of bend strength values is difficult, although the stress required for deflection/failure of $\text{Mo}_5\text{Si}_3\text{C}$ in the current study appears somewhat higher than for other silicides and composites tested at the same temperature and having similar grain size. Again, this may be related to the very high stresses needed to initiate dislocation glide in $\text{Mo}_5\text{Si}_3\text{C}$ even at 1200°C ; it is also possible that the use of smaller samples than many of the other studies represented in Table 4.2 contributed to the higher strength values [162].

A trend similar to the high-temperature bend strength is observed when comparing the compressive flow stresses of other silicides with $\text{Mo}_5\text{Si}_3\text{C}$ -based materials, although as with bend test data, direct comparisons are complicated by the various combinations of strain rates and grain sizes chosen. Recalling Figures 4.3 and Figure 4.5, the compressive flow stresses of $\text{Mo}_5\text{Si}_3\text{C}$ are equal or higher to MoSi_2 tested at similar grain sizes and strain rates, with the superiority of $\text{Mo}_5\text{Si}_3\text{C}$ more pronounced for larger grain sizes at higher temperatures. Compared with another D8₃ silicide, Ti_5Si_3 [80], $\text{Mo}_5\text{Si}_3\text{C}$ having a grain size of $23\text{ }\mu\text{m}$ displays a flow stress almost 100 MPa higher at 1300°C and $\dot{\epsilon} \sim 10^{-4}$ even though titanium silicide has a larger reported grain size, a fact which should favor its high-temperature strength.

4.3.6 Effectiveness of Alloying to Improve Ductility

From the results presented thus far, it should be clear that the increased crystal symmetry or any possible bonding modification of the interstitially-stabilized $\text{Mo}_5\text{Si}_3\text{C}$ compound did not result in any noticeable improvements in room temperature toughness or

a reduction in brittle-to-ductile-transition temperature (BDTT) compared to other lower-symmetry silicides. To better understand why the desired property improvements were not realized, it is worth examining possible intrinsic and extrinsic mechanisms (Table 4.3) that play a role in the mechanical behavior of $\text{Mo}_5\text{Si}_3\text{C}$.

Table 4.4 Effects of various factors on the mechanical behavior of $\text{Mo}_5\text{Si}_3\text{C}$.

Intrinsic Factors		Extrinsic Factors	
<i>Factor</i>	<i>Effects</i>	<i>Factor</i>	<i>Effects</i>
<i>Semi-covalent bonding</i>	Large Peierls stress, complex dislocation core structure, resistance to motion, high APB energy	<i>Grain size</i>	Fine: minimize CTE anisotropy Coarse: reduce GB sliding, increase strength
<i>Large, 16-atom unit cell</i>	Large b , increased dislocation energy (minimal generation), broad cores/sessile locks?	<i>Stoichiometry</i>	Amount 2 nd phases limit GS, refine structure, vacancies/interstitial filling effects?
<i>Hexagonal symmetry</i>	Bonding, atomic arrangement outweigh? CTE anisotropy: thermal cracking Elastic anisotropy: complex stress states?	<i>Defects</i>	Oxide phases: wetting, composition, distribution Microcracking-loss of strength, toughening? Porosity—strength degradation

Of the issues raised in Table 4.3, the most dominant contribution to the ambient temperature behavior of $\text{Mo}_5\text{Si}_3\text{C}$ is probably the high intrinsic lattice resistance to dislocation motion (Peierls stress). Even at temperatures high enough such that dislocations have some appreciable mobility, the large, complex unit cell restricts slip to $c\{0001\}$ -type. Since the associated slip vector is more than 0.5 nm in length, slip is highly unfavorable energetically for the available slip systems based on the assumption that the energy of a dislocation is approximately proportional to b^2 [86]. In addition, ways through which defects could move at non-unit repeat distances in $\text{Mo}_5\text{Si}_3\text{C}$ such as disassociation reactions and formation of stacking faults would require the breaking of the strong Mo-Si and Si-Si bonds to form the associated faults. It seems evident that the hexagonal

symmetry of $\text{Mo}_5\text{Si}_3\text{C}$ does not lead to the activation of additional deformation mechanisms compared with tetragonal MoSi_2 , in fact the number of available slip systems is probably less even at temperatures near $0.5T_m$. A similar conclusion has also been reached for the hexagonal ternary phase $\text{Mo}(\text{Si},\text{Al})_2$, a compound whose higher symmetry and anticipated more "metallic" character did not result in improved ductility compared with MoSi_2 [129]. For elevated temperature deformation, grain size is a very important factor, along with the composition, amount, and distribution of any non-crystalline phases present.

Efforts to improve the toughness and ductility of intermetallics through stabilizing higher symmetry crystal structures have, in general, met with little success. Despite much effort, ductility improvements achieved through alloying additions to tetragonal Al_3X compounds has been minimal [180-182]. For these stabilized, cubic L1_2 trialuminides, the high symmetry and small unit cells of these ordered fcc structures should favor low-temperature plasticity. However, it has been determined that a directional component to the Al-X bonding in the parent D0_{22} structures is not alleviated by alloying to the higher symmetry L1_2 structure, and, accordingly, these materials remain brittle at room temperature [122,123].

Another example where increased symmetry did not lead to noticeable improvements low-temperature mechanical properties is the ternary silicide $\text{Si}_3\text{Ti}_2\text{Zr}_3$; at ambient temperature, this D8_8 hexagonal compound exhibited a hardness of 15.9 GPa and a toughness of $3.6 \text{ MPa}\cdot\text{m}^{1/2}$ [151]. As with the other hexagonal ternary silicides, $\text{Mo}_5\text{Si}_3\text{C}$ and $\text{Mo}(\text{Si},\text{Al})_2$, enough of a covalent bonding character and complex atom arrangement is retained in $\text{Si}_3\text{Ti}_2\text{Zr}_3$ that neither a measurable density of dislocations nor adequate slip systems for them to move is possible at reasonable temperatures. The behavior of these materials is likely approximated by curve (3) in Figure 4.13, where the intrinsic fracture stress, σ_f , (of which the Peierls stress is an important component) is lower than the flow stress of the material for all meaningful temperatures. Fracture in polycrystalline materials of this type is only suppressed when diffusional flow and grain boundary sliding

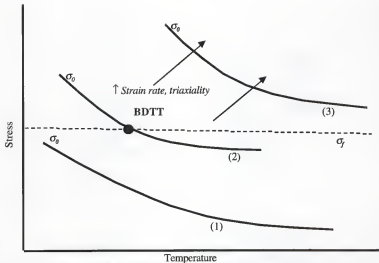


Figure 4.13 Schematic representation of the effects of temperature on the relationship between intrinsic brittle fracture stress (σ_f) and material flow/yield stress (σ_o) after [183]. For type (1) behavior (fcc metal), the flow stress is below σ_f over the entire temperature range, and ductile behavior is expected. Type (2) materials (bcc metals) show a transition from brittle to ductile behavior (BDTT) where the flow stress and fracture stress curves intersect; increases in strain rate or triaxial stress state shift the σ_o curve in the direction indicated, increasing the BDTT. Most intermetallics, including $\text{Mo}_5\text{Si}_3\text{C}$, display behavior similar to (3), where intrinsic factors lead to sufficiently high σ_o values so that polycrystalline ductility is impossible until high temperatures are reached, where dislocation climb and diffusional flow process are capable of accommodating material deformation.

mechanisms intercede and allow deformation and the appearance of a brittle-to-ductile transition (BDT) well before sufficient dislocation-controlled slip mechanisms could be thermally activated. The time-dependent nature of the flow processes which produce the appearance of plastic deformation in materials of type (3) implies that they are intrinsically strain-rate sensitive. Brittle fracture can therefore never be completely suppressed across the range of all potential deformation rates, contrary to a true BDT.

4.4 Summary and Conclusions

An initial assessment of the mechanical behavior of powder-processed $\text{Mo}_5\text{Si}_3\text{C}$ -based materials was conducted to compare the observed property values and behavior to those of other candidate high-temperature materials. A key issue was to determine what influence the stabilized hexagonal crystal structure of $\text{Mo}_5\text{Si}_3\text{C}$ may have on the potential for improved room temperature toughness and ductility. In addition, the elevated temperature behavior of the ternary phase was also examined in both compression and bending. At room temperature, $\text{Mo}_5\text{Si}_3\text{C}$ displays an increased hardness (13 GPa) and similarly low toughness ($\sim 3 \text{ MPa}\cdot\text{m}^{1/2}$) to other silicide materials. Compared with other silicide materials, $\text{Mo}_5\text{Si}_3\text{C}$ has better strength retention at temperatures above 1200°C in both compression and bending especially for the larger grain size materials; deformation mechanisms appear to be similar to those reported for other silicides with a rapid drop off in stress with increasing temperature related to a transition from boundary sliding accommodated by dislocation glide ($n\sim 3$) to grain boundary sliding/diffusional flow controlled deformation ($n\sim 1$).

One issue with larger grain size $\text{Mo}_5\text{Si}_3\text{C}$ is increased microcracking presumably due to the CTE anisotropy-related thermal stresses that develop during cooling from the processing temperatures. Another way in which processing parameters influence the mechanical behavior of $\text{Mo}_5\text{Si}_3\text{C}$ -based materials is evident in the finer grain, mechanically alloyed materials whose very fine starting powder size leads to increased oxygen content in

the consolidated bodies; the retention of silica in the microstructures is thought to augment boundary sliding already favored in the smaller grain size $\text{Mo}_5\text{Si}_3\text{C}$.

Through analysis of the dislocation structures observed in $\text{Mo}_5\text{Si}_3\text{C}$ samples deformed under compression, it was determined that the predominant active slip mechanism above 1000°C was $c[0001]$. This implies the activation of only two independent slip systems, indicating that stabilizing the hexagonal structure did not result in an increased number of slip systems compared with lower-symmetry silicides. Comparing the primary slip systems and its associated slip vector lengths (Table 4.4) of common intermetallics with those of $\text{Mo}_5\text{Si}_3\text{C}$ and $\text{Mo}(\text{Si},\text{Al})_2$, compounds in which it was hoped that alloying would lead to increased potential for ductility, it is seen that both have very high activation temperatures for slip and, in the case of $\text{Mo}_5\text{Si}_3\text{C}$, a very large slip vector. This indicates the general ineffectiveness of alloying intermetallics to improve ductility through crystal symmetry improvements; if the directionality of bonding and/or complex atomic arrangements are not significantly affected by the alloying additions, the transition to higher symmetry crystal structures alone is no guarantee of improved ductility. In fact, $\text{Mo}_5\text{Si}_3\text{C}$ appears to actually have increased hardness and brittleness compared to its lower-symmetry binary silicide counterparts.

Table 4.4 Comparison of slip systems, slip vector lengths, and lower activation temperature limits for $\text{Mo}_5\text{Si}_3\text{C}$ and $\text{Mo}(\text{Si},\text{Al})_2$ with several extensively studied intermetallic compounds.

Material	Crystal Structure	Primary Slip System	Length of Slip Vector, b (nm)	Temp. Range Active ($^\circ\text{C}$)	Ref.
$\text{Mo}_5\text{Si}_3\text{C}$	D8_8	$\{\text{hki}0\}[0001]$	0.505	>1000	this work
$\text{Mo}(\text{Si},\text{Al})_2$	C40	$(0001)\langle 11\bar{2}0 \rangle$	0.156	>1100	[129]
MoSi_2	C11_b	$\{110\}\langle 111 \rangle$	0.453	>500	[171]
NiAl	B2	$\{110\}\langle 100 \rangle$	0.288	RT	[184]
γTiAl	L1_0	$\{111\}\langle 110 \rangle$	0.283	RT	[143]
Ni_3Al	L1_2	$\{111\}\langle 110 \rangle$	0.252	RT	[123]

CHAPTER 5 GENERAL DISCUSSION AND CONCLUSIONS

At its outset, this study was envisioned to be primarily a cursory examination of the mechanical properties of the ternary intermetallic compound $\text{Mo}_5\text{Si}_3\text{C}$ to determine if it exhibited any property improvements compared with MoSi_2 and if these improvements could be correlated with the increased crystal symmetry of the ternary phase. However, over the course of the project, the study was expanded to encompass the examination of a wide range of processing-microstructure-property relationships in $\text{Mo}_5\text{Si}_3\text{C}$ -based materials. This more circuitous route to examining mechanical behavior was a direct consequence of the difficulties faced in producing dense, single-phase, homogeneous, and crack-free $\text{Mo}_5\text{Si}_3\text{C}$.

Conventional arc-casting methods, proved to be ineffective from the standpoint of grain size control, alloy homogenization, and minimizing thermally-induced cracking. Arc melting is appealing for alloy development since it allows for a quick screening of a number of potential compositions; it is less attractive in the case of silicides which mix one or more high melting point refractory metals with low-melting and high vapor pressure silicon, making homogenization through re-melting without excessive weight losses very difficult. Furthermore, the large thermal gradients involved and the large as-cast grain sizes, prove even more problematic when melting non-cubic materials such as $\text{Mo}_5\text{Si}_3\text{C}$ which likely have pronounced thermal expansion coefficient anisotropy.

Powder methods are the preferred processing method for $\text{Mo}_5\text{Si}_3\text{C}$ and other silicides since they can be optimized to result in dense, crack-free materials, and allow for some flexibility in grain size through varying the starting powder size and hot pressing time/temperature combinations. Either blending or high-energy milling of precursor

powders followed by hot pressing have proven reasonably successful, with the latter approach leading to finer microstructures.

One of the main drawbacks to the powder processing of silicides is the presence of siliceous phases on the surfaces of the starting powders which are incorporated into the microstructure as discrete grain boundary phases. From the microstructures of blended powder + hot-pressed materials, and the low oxygen content of the processed materials, it seems clear that silica removal by carbon is an effective way to eliminate silica, although it can result in SiC-lined regions of gas porosity and shifts in composition toward the Mo-rich. This raises a basic issue for the powder-processing of silicides, namely, that without elaborate powder handling schemes, one must either accept the presence of silica or the byproducts of its reduction reactions.

Unfortunately, these larger grain size materials also show an increased density of microcracks, again related to the CTE anisotropy. Microcracking can be suppressed in the finer grain, MA materials, which also show reduced porosity compared to the blended powder samples. However, along with these more desirable features comes the presence of fine distributions of $\sim 1\text{ }\mu\text{m}$ silica particles, which are expected to further reduce the strength at temperature of the fine-grain $\text{Mo}_5\text{Si}_3\text{C}$ already predisposed to grain boundary sliding. The implication here is that, depending on type of loading and temperature, the strength and flow characteristics of the materials processed by powder blending (microcracked) or MA (silica particles) will vary.

An additional impediment to the reproducible processing of single-phase $\text{Mo}_5\text{Si}_3\text{C}$ is the narrow solubility range for the compound (Mo:Si 1.6-1.7, C 8-10 At. %) discovered during the course of this study. Uncertainties and inaccuracies in equilibria and phase boundaries are not uncommon in the thermodynamic data for silicides generated in the 1950s and 1960s [115, 128], primarily because of the heavy reliance on XRD as the sole method of phase identification and inferred compositional information. For example in the current work, samples containing minor second phase constituents may appear as single

phase if only XRD spectra are considered. It is a testament to the skills of these early researchers that much of the thermodynamic data and phase equilibria on silicides collected in the 1950s and 60s have been shown to be correct.

Considering mechanical behavior and properties, $\text{Mo}_5\text{Si}_3\text{C}$ exhibits high hardness (13.2 GPa), low toughness ($2.5 \text{ MPa}\cdot\text{m}^{1/2}$) and compressive flow stresses comparable or superior to other silicides at equivalent strain rate and grain size combinations. A grain size-dependent transition in flow behavior was observed in both compression and bending, with the finer grain, higher-oxygen materials showing a rapid decrease in flow stress and suppression of fracture in bending with increasing temperature because of diffusionally-accommodated grain boundary sliding enhanced by viscous flow of amorphous silica particles near grain boundaries and triple points.

From the low toughness values for $\text{Mo}_5\text{Si}_3\text{C}$ and persistence of brittle failure, even in compression, to temperatures above 1000°C , it is apparent that achieving ductility improvements by alloying to improve crystal symmetry is not a universally applicable method for improving mechanical properties in strongly bonded materials having complex, large (many atoms) unit cells. Consistent with this conclusion, the determination of $c[0001]$ as the prevailing slip vector in $\text{Mo}_5\text{Si}_3\text{C}$ at $T > 1000^\circ\text{C}$ implies both an inherent low density of dislocations and unfavorable and insufficient slip systems for polycrystalline ductility.

Based on attempts in other intermetallic systems [185], methods for improving the ductility of silicides are still under investigation, including microalloying to produce ternary or quaternary compounds with reduced Si-Si or Mo-Si bond strengths [15, 17, 124] or processing of lower Si-content materials with the goal of having a ductile molybdenum solid solution as the continuous matrix phase [150]. Even if successful in improving the toughness of these silicide-based materials, these approaches would most likely result in reductions in other desirable properties such as creep resistance, specific strength, or oxidation resistance. Property tradeoffs of this sort are common in the development of

advanced materials, intermetallics included; an indication of this is as shown in Figure 5.1 where density-normalized elevated-temperature strength is plotted against room temperature fracture toughness for several candidate high-temperature structural materials.

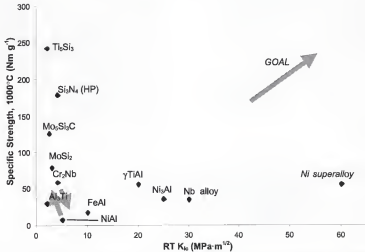


Figure 5.1 Plot of room temperature fracture toughness against specific strength at 1000 °C for several candidate materials for high temperature applications. Note that attempts to toughen high-strength intermetallics through alloying or ductile reinforcements usually lead to a drop in strength such as for the Laves phase Cr₂Nb. Conversely, for materials such as NiAl, mechanisms which improve high temperature strength are usually linked to a drop in toughness [44, 186].

This plot indicates that in their current state of development, the majority of intermetallics simply cannot approach the toughness/impact resistance required for gas turbine engines applications [22, 187]. In addition, Figure 5.1 shows the tradeoffs that often occur when improvements in a particular property are sought; for example in NiAl, improvements in creep resistance are usually at the expense of toughness, while in Cr₂Nb-

based materials, the increased toughness is linked to a degradation in creep strength [44, 186, 188].

Those intermetallics that do show promise (e.g., γ -TiAl) and have undergone some degree of commercial development are typically those envisioned for the lower-temperature, lower-stress regions of gas turbine engines such as compressor vanes, compressor cases, low-pressure turbine blades, and exhaust flaps [187, 189]. In the case of γ -TiAl, the primary reason for its ongoing consideration for these applications is its superior specific strength at $T < 1000^\circ\text{C}$ compared with current structural materials (e.g., ferrous and conventional titanium alloys). For the hottest sections of gas turbine engines, materials systems based on refractory metals with improved oxidation resistance (e.g., Mo-Si-B, Nb-alloys) may at some point be viable alternatives to Ni-based superalloys, although the process development and microstructural optimization of these materials is still in its early stages [46, 114, 150, 190]. Because of difficulties in achieving the desired balance of properties, the focus of ongoing work in silicide-based materials has shifted toward applications in which room-temperature toughness and ductility are not critical, such as long-life heating elements and aids to metal and glass processing [26].

APPENDIX A
SELECTED HOT PRESS TIME-TEMPERATURE-PRESSURE PROFILES

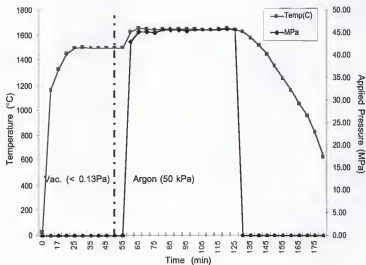


Figure A-1 Plot showing temperature and applied pressure during processing of sample LD8 using two-stage hot pressing method. Processing temperatures are 1500°C for 0.5 h followed by 1650°C for 1 h.

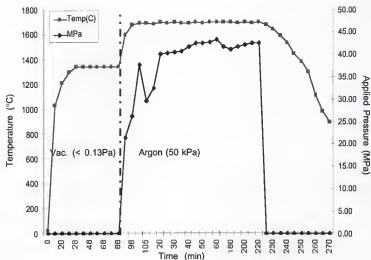


Figure A-2 Plot showing temperature and applied pressure during processing of sample C10B5EL2 using a two-stage hot pressing method. Processing temperatures are 1350°C for 1 h followed by 1700°C for 2h.

APPENDIX B
SELECTED COMPRESSIVE STRESS-STRAIN CURVES

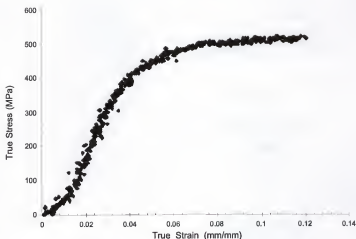


Figure B-1 Compressive stress-strain curve for sample LD8 tested at 1200°C at a nominal strain rate of $1 \times 10^{-4} \text{ s}^{-1}$. Note the change in slope of the elastic region of the curve near 1 % strain; this initial transient is likely related to the alignment and compression of the push rods and platens during which displacement can be accommodated with minimal stress applied to the sample.

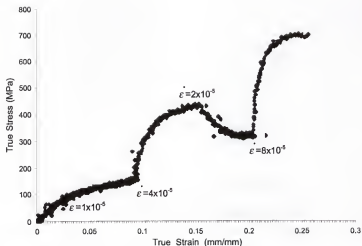


Figure B-2 Compressive stress-strain curve for multiple strain rate test of sample LD8 at 1200°C. The positions of the initial, nominal strain rates indicate where the displacement rate was changed to match the desired strain rate after sufficient prior steady state yield behavior.

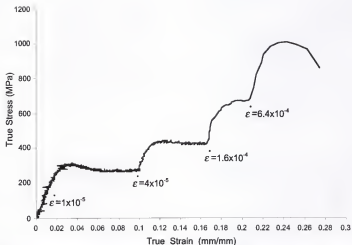


Figure B-3 Compressive stress-strain curve for multiple strain rate test of sample C10B5 at 1200°C. The positions of the initial, nominal strain rates indicate where the displacement rate was changed to match the desired strain rate after sufficient prior steady state yield behavior.

REFERENCES

1. A. Gokhale and G.J. Abbaschian, *The Mo-Si (Molybdenum-Silicon) System*. Journal of Phase Equilibria, 1991. 12(4): p. 493-498.
2. G.V. Samsonov, *Silicides and their uses in engineering*, 1959, Wright Patterson Air Force Base: Dayton, OH.
3. A.K. Vasudevan and J.J. Petrovic, *A comparative overview of molybdenum disilicide composites*. Materials Science and Engineering A, 1992. A155: p. 1-17.
4. D.A. Berztsis, R.R. Cerchiara, E.A. Gulbransen, F.S. Petit, and G.H. Meier, *Oxidation of MoSi₂ and comparison with other silicide materials*. Materials Science and Engineering, 1992. A155: p. 165-181.
5. G. Sauthoff, *The High Temperature Deformation of Intermetallic Alloys*, in *Structural Intermetallics*, R. Darolia, et al., eds., 1993, TMS: Warrendale, PA. p. 845-860.
6. K. Sadananda, C.R. Feng, R. Mitra, and S.C. Deevi, *Creep and fatigue properties of high temperature silicides and their composites*. Materials Science and Engineering A, 1999. A261: p. 223-238.
7. K.S. Kumar, *Silicides: science, technology and applications*, in *Intermetallic Compounds: Vol. 2, Practice*, J.H. Westbrook and R.L. Fleisher, eds., 1994, John Wiley, New York. p. 211-235.
8. Y.-L. Jeng, E.J. Lavarnia, and J. Wolfenstine, *Creep Behavior of Plasma-Sprayed SiC-Reinforced MoSi₂*. Scripta Metallurgica et Materialia, 1993. 29: p. 107-111.
9. D.A. Hardwick, P.L. Martin, S.N. Patankar, and J.J. Lewandowski, *Processing-microstructure-property relationships in polycrystalline MoSi₂*, in *Structural Intermetallics*, R. Darolia, et al., eds., 1993 TMS: Warrendale, PA. p. 665-673.
10. S. Chin, D.L. Anton, and A.F. Giamei, *Ternary MoSi₂ Compounds for High Temperature Structural Applications*, in *High Temperature Silicides and Refractory Alloys*, C.L. Briant, et al., eds., MRS Symposium Proceedings, Vol. 322. 1994, MRS: Warrendale, PA. p. 423-429.
11. C.T. Liu, J.O. Stiegler, and F.H. Froes, *Ordered Intermetallics*, in *Metals Handbook*, Vol. 2. 1991, ASM: Materials Park, OH p. 913-942.
12. C.H. Henager, J.L. Brimhall, and L.N. Brush, *Tailoring structure and properties of composites synthesized in situ using displacement reactions*. Materials Science and Engineering, 1995. A195: p. 65-74.

13. S. Jayashankar, S.E. Riddle, and M.J. Kaufman, *Synthesis and Properties of In-Situ MoSi_2/SiC Composites*, in *High Temperature Silicides and Refractory Alloys*, C.L. Briant, et al., eds. MRS Symposium Proceedings, Vol. 322, 1994, MRS: Pittsburgh. p. 33-40.
14. W.J. Boettinger, J.H. Perepezko, and P.S. Frankwicz, *Application of ternary phase diagrams to the development of MoSi_2 -based materials*. Materials Science and Engineering, 1992. A155: p. 33-44.
15. D. Yi, Z. Lai, C. Li, O.M. Akselsen, and J.H. Ulvensoen, *Ternary Alloying Study of MoSi_2* . Metallurgical and Materials Transactions A, 1998. 29A: p. 119-129.
16. B.K. Vulf, *Ternary Intermetallic Compounds*. Russian Chemical Reviews, 1960. 29(6): p. 364-376.
17. D.P. Shah and D.L. Anton, *Ternary Alloying of Refractory Intermetallics*, in *High Temperature Ordered Intermetallic Alloys IV*. MRS Symposium Proceedings, Vol. 213, 1991 MRS: Pittsburgh. p. 63-68.
18. H. Nowotny, E. Parthe, R. Kieffer, and F. Benesovsky, *Das Driestoffsystem: Molybden-Silizium-Kohlenstoff*. Monatshefte für Chemie, 1954. 85: p. 255-272.
19. F.J.J. van Loo, F.M. Smet, G.D. Rieck, and G. Verspui, *Phase relations and diffusion paths in the Mo-Si-C system at 1200 °C*. High Temperatures-High Pressures, 1982. 14: p. 25-31.
20. D.L. Anton, D.M. Shah, D.N. Duhl, and A.F. Giamei, *Selecting High-Temperature Structural Intermetallic Compounds: The Engineering Approach*. JOM, 1989. 41(9): p. 12-17.
21. J.E. Hartsel and C.J. Smith, *Advanced Materials: the Enabling Technologies for Future Ultra Bypass Engines*, 1989 GE Aircraft Engines: Cincinnati, OH.
22. P.K. Wright, *On Ductility and Toughness Requirements for Intermetallics in Aircraft Engines*, in *Structural Intermetallics*, R. Darolia, et al., eds., 1993, TMS: Warrendale, PA. p. 885-893.
23. G.L. Erickson, *Polycrystalline Cast Superalloys*, in *Metals Handbook: Properties and Selection: Irons, Steels, and High Performance Alloys*, Vol. 1. 1990, ASM: Materials Park, OH. p. 981.
24. J.B. Lambert, *Refractory Metals and Alloys*, in *Metals Handbook, Tenth Addition*, Vol. 2. 1991, ASM: Materials Park, OH. p. 557-577.
25. K.K. Chawla, *Ceramic Matrix Composites*. 1993, London: Chapman & Hall.
26. J.J. Petrovic and A.K. Vasudevan, *Key developments in high temperature structural silicides*. Materials Science and Engineering A, 1999. A261: p. 1-5.
27. G. Sauthoff, *Plastic Deformation*, in *Intermetallic Compounds*, J.H. Westbrook and R.L. Fleischer, eds., Vol. 1, 1994 John Wiley, New York.: New York. p. 911-934.
28. M. Hunt, *The Promise of Intermetallics*. Mechanical Engineering, 1990(3): p. 35-39.

29. R.L. Fleisher, D.M. Dimiduk, and H.A. Lipsitt, *Intermetallic Compounds for Strong High-Temperature Materials: Status and Potential*. Annual Reviews in Materials Science, 1989. 19: p. 231-263.
30. D.P. Pope and R. Darolia, *High-Temperature Applications of Intermetallic Compounds*. MRS Bulletin, 1996. 21(5): p. 30-36.
31. *Graded-density thermal tile reduces damage to Shuttle*. Advanced Materials & Processes, 1994. 146(4): p. 9.
32. S. Tuominen and C. Wojcik, *Alloys for Aerospace*. Advanced Materials & Processes, 1995. 147(4): p. 23-26.
33. P. Schwarzkopf and R. Kieffer, *Refractory Hard Metals*. 1953, Macmillan: New York.
34. W.A. Maxwell, *Properties of certain intermetallics as related to elevated-temperature applications I - Molybdenum disilicide*. NACA Research Memorandum, 1949. RM E9G01.
35. W.A. Maxwell, *Some factors affecting the high-temperature strength of molybdenum disilicide*. NACA Research Memorandum, 1952. RM E52B06.
36. W.A. Maxwell and R.W. Smith, *Thermal shock resistance and high temperature strength of a molybdenum disilicide - aluminum oxide ceramic*. NACA Research Memorandum, 1953. E53F26.
37. J.B. Huffadine, *The fabrication and properties of molybdenum disilicide-alumina*, in *Special Ceramics*, P. Popper, Editor, 1960, Heywood: London.
38. A.G. Evans, *The mechanical properties of reinforced ceramic, metal and intermetallic matrix composites*. Materials Science and Engineering, 1991. A143: p. 63-76.
39. P.D. Eason, *Processing, Phase Equilibria and Environmental Degradation of Mo(Si,Al), Intermetallic Compound*. Ph.D. dissertation, 1998. University of Florida, Gainesville..
40. K.F. Products, *Kanthal Super Handbook*. 2nd ed., 1984 Kanthal Furnace Products: Hallstahammar, Sweden:
41. P.J. Meschter and D.S. Schwartz, *Silicide-Matrix Materials for High-Temperature Applications*. JOM, 1989. 41(11): p. 52-55.
42. M.F. Ashby and D.R.H. Jones, *Engineering Materials I*. 1980, Butterworth-Heinemann : Oxford, UK..
43. E.L. Courtright, *Engineering Property Limitations of Structural Ceramics and Ceramic Composites Above 1600 °C*. Ceramic Engineering and Science Proceedings, 1991. 12(9 - 10): p. 1725-1744.
44. D.B. Miracle and R. Darolia, *NiAl and its Alloys*, in *Intermetallic Compounds: Vol. 2, Practice*, J.H. Westbrook and R.L. Fleisher, eds., 1994 John Wiley, New York. p. 53-72.

45. S.C. Huang and J.C. Chesnutt, *Gamma TiAl and its alloys*, in *Intermetallic Compounds: Vol. 2, Practice*, J.H. Westbrook and R.L. Fleisher, eds., 1994 John Wiley, New York. p. 73-90.
46. C.C. Wojcik, *Processing, Properties and Applications of High-Temperature Niobium Alloys*, in *High Temperature Silicides and Refractory Alloys*, C.L. Briant, et al., eds. MRS Symposium Proceedings, Vol. 322, 1994 MRS: Pittsburgh. p. 519-530.
47. J.B. Wachtman, *Dislocations and Plastic Deformation in Ceramics*, in *Mechanical Properties of Ceramics*, . 1996, John Wiley , New York. p. 297-309.
48. Y.L. Jeng and E.J. Lavernia, *Review: Processing of molybdenum disilicide*. Journal of Materials Science, 1994. **29**: p. 2557-2571.
49. N.S. Stoloff, *An overview of power processing of silicides and their composites*. Materials Science and Engineering A, 1999. **A261**: p. 169-180.
50. S.A. Maloy, A.H. Heuer, J.J. Lewandowski, and J.J. Petrovic, *Carbon additions to molybdenum disilicide: improved high-temperature mechanical properties*. Journal of the American Ceramic Society, 1991. **74**: p. 2704-2706.
51. D.A. Hardwick, *Composites Based on Molybdenum Disilicide: Progress and Prospects*, in *Intermetallic Matrix Composites III*. MRS Symposium Proceedings, Vol. 350. 1994, MRS: Pittsburgh. p. 165 - 176.
52. R. Mitra, Y.R. Mahajan, N.E. Prasad, and W.A. Chiou, *Processing-microstructure-property relationships in reaction hot-pressed MoSi₂ and MoSi₂-SiC_p composites*. Materials Science and Engineering A, 1997. **A225**: p. 105-117.
53. C.H. Worner, *Some Remarks on the Zener Drag*. Scripta Metallurgica, 1989. **23**: p. 1909-1912.
54. S.C. Deevi, *Self-propagating high-temperature synthesis of molybdenum disilicide*. Journal of Materials Science, 1991. **26**: p. 3343 - 3353.
55. Y.-L. Jeng, J. Wolfenstine, and E.J. Lavernia, *Low-Pressure Plasma-Deposition of SiC-Reinforced MoSi₂*. Scripta Metallurgica et Materialia, 1993. **28**: p. 453 - 458.
56. X. Yang and M.N. Rahaman, *Mechanical alloying of Mo and Si powders and their sintering*. Ceramic Engineering and Science Proceedings, 1993. **14**(9 - 10): p. 1209-1217.
57. B.K. Yen, T. Aizawa, and J. Kihara, *Influence of Powder Composition and Milling Media on Formation of Molybdenum Disilicide by a Mechanically Induced Self-Propagating Reaction*. Journal of the American Ceramic Society, 1996. **79**(8): p. 221 - 223.
58. S. Jayashankar and M.J. Kaufman, *Tailored MoSi₂/SiC composites by mechanical alloying*. Journal of Materials Research, 1993. **8**: p. 1428-1441.
59. A.W. Searcy and A.G. Tharp, *The Dissociation Pressures and the Heats of Formation of the Molybdenum Silicides*. Journal of Physical Chemistry, 1960. **64**: p. 1539-1542.

60. E. Fitzer, K. Reinmuth, and H. Schnabel, *Pressen und Sintern von Molybdaendisilizid*. Arch. Eisenhuettenwes, 1969. 11: p. 895-900.
61. J.D. Cotton, Y.S. Kim, and M.J. Kaufman, *Intrinsic second-phase particles in powder processed MoSi_2* . Materials Science and Engineering, 1991. A144: p. 287-191.
62. K. Sadananda and C.R. Feng, *A Review of Creep of Silicides and Composites*, in *High Temperature Silicides and Refractory Alloys*, C.L. Briant, et al., eds.. MRS Symposium Proceedings, Vol. 322, 1994 MRS: Pittsburgh. p. 157-173.
63. S. Jayashankar, *Structure/Property/Processing Relationships in Molybdenum Disilicide/Silicon Carbide Composites*. Ph.D. Dissertation, 1996. University of Florida, Gainesville.
64. A. Costa e Silva, *Synthesis of molybdenum disilicide composites using in situ reactions*. Ph.D., 1994. University of Florida, Gainesville
65. N.S. Jacobson, K.N. Lee, S.A. Maloy, and A.H. Heuer, *Chemical reactions in the processing of MoSi_2 + carbon compacts*. Journal of the American Ceramic Society, 1993. 76: p. 2005-2009.
66. S.A. Maloy, J.L. Lewandowski, A.H. Heuer, and J.J. Petrovic, *Effects of carbon additions on the high temperature mechanical properties of molybdenum disilicide*. Materials Science and Engineering A, 1992. A155: p. 159-163.
67. D.H. Carter and P.L. Martin, *Ta and Nb reinforced MoSi_2* , in *Intermetallic Matrix Composites*. MRS Symposium Proceedings, Vol. 194, 1990, MRS: Pittsburgh. p. 131-137.
68. L. Xiao and R. Abbaschian, *Role of matrix/reinforcement interfaces in the fracture toughness of brittle materials toughened by ductile reinforcement*. Metallurgical Transactions A, 1992. 23A: p. 2863-2872.
69. L. Xiao and R. Abbaschian, *Interfacial modification in Nb/ MoSi_2 composites and its effects on fracture toughness*. Materials Science and Engineering A, 1992. A155: p. 135-145.
70. N.S. Stoloff and D.E. Alman, *Innovative processing techniques for intermetallic matrix composites*, . MRS Symposium Proceedings, Vol. 194, 1990 MRS: Pittsburgh. p. 31-43.
71. R.A. Rapp, A. Eis, and G.Y. Yurek, *Displacement Reactions in the Solid State*. Metallurgical Transactions, 1973. 4: p. 1283-1292.
72. C.H. Henager, J.L. Brimhall, and J.P. Hirth, *Synthesis of a MoSi_2 - SiC composite in situ using a solid state displacement reaction*. Materials Science and Engineering, 1992. A155: p. 109-114.
73. A. Costa e Silva and M.J. Kaufman, *Synthesis of MoSi_2 -boride composites through in situ displacement reactions*. Intermetallics, 1997. 5: p. 1-15.

74. A. Stergiou and T. Tsakiroopoulos, *Study of the Effects of Al, Ta, W Additions on the Microstructure and Properties of MoSi₂ Base Alloys*, in *High-Temperature Ordered Intermetallic Alloys VI*. MRS Symposium Proceedings, Vol. 364, 1995 MRS: Pittsburgh. p. 911-916.
75. D.P. Shah, D. Berczik, D.L. Anton, and R. Hecht, *Appraisal of other silicides as structural materials*. Materials Science and Engineering, 1992. A155: p. 45-57.
76. R.M. Aikin, *Structure and properties of in situ reinforced MoSi₂*. Ceramic Engineering and Science Proceedings, 1991. 12 [9-10]: p. 1643-1655.
77. R.M. Aikin, *Strengthening of discontinuously reinforced MoSi₂ composites at high temperatures*. Materials Science and Engineering, 1992. A155: p. 121-133.
78. D.J. Tilly, J.P.A. Lofvander, and C.G. Levi, *Solidification Paths and Carbide Morphologies in Melt-Processed MoSi₂-SiC In Situ Composites*. Metallurgical and Materials Transactions A, 1997. 28A: p. 1889-1900.
79. M.G. Mendiratta, J.J. Lewandowski, and D.M. Dimiduk, *Strength and Ductile-Phase Toughening in the Two-Phase Nb/Nb₅Si₃ Alloys*. Metallurgical Transactions A, 1991. 22A: p. 1573-1583.
80. G. Frommeyer, R. Rosenkranz, and C. Ludecke, *Microstructure and Properties of the Refractory Intermetallic Ti₅Si₃ Compound and the Unidirectionally Solidified Eutectic Ti-Ti₅Si₃ Alloy*. Zeitschrift fuer Metallkunde, 1990. 81: p. 307-313.
81. P.H. Boldt, J.D. Embury, and G.C. Weatherly, *Room temperature microindentation of single-crystal MoSi₂*. Materials Science and Engineering, 1992. A155: p. 251-258.
82. Y. Umakoshi, T. Sakagami, T. Hirano, and T. Yamane, *High Temperature Deformation of MoSi₂ Single Crystals With the C11b Structure*. Acta Metallurgica et Materialia, 1990. 38: p. 909-915.
83. O. Unal, J.J. Petrovic, D.H. Carter, and T.E. Mitchell, *Dislocations and plastic deformation in molybdenum disilicide*. Journal of the American Ceramic Society, 1990. 73(6): p. 1752-1757.
84. S.A. Maloy, A.H. Heuer, J.J. Lewandowski, and T.E. Mitchell, *On the slip systems in MoSi₂*. Acta Metallurgica et Materialia, 1992. 40(11): p. 3159-3165.
85. R. von Mises, *Mechanik der plastischen Formänderung von Kristallen*. Zeitschrift für Angewandte Mathematik und Mechanik, 1928. 8(3): p. 161-185.
86. G.E. Dieter, *Mechanical Metallurgy*. 3rd ed. 1986, McGraw-Hill :New York.
87. K.J. Bowman, *Refractory Metal Disilicides Research*, . 1992, Metals Information Analysis Center. West Lafayette, IN.
88. L. Xiao, Y.S. Kim, and R. Abbaschian, *Ductile phase toughening of MoSi₂ - chemical compatibility and fracture toughness*, in *Intermetallic Matrix Composites*. MRS Symposium Proceedings, Vol. 194, 1990 MRS: Pittsburgh. p. 399-404.

89. K. Tanaka, H. Inui, M. Yamaguchi, and M. Koiwa, *Directional atomic bonds in MoSi_2 and other transition-metal disilicides with the C11b, C40 and C54 structures*. Materials Science and Engineering A, 1999. A261: p. 158-164.
90. S.R. Srinivasan, R.B. Schwarz, and J.D. Embury, *Ductile-to-Brittle Transition in MoSi_2* , in *High-Temperature Ordered Intermetallic Alloys V*. MRS Symposium Proceedings, Vol. 288, 1993 MRS: Pittsburgh. p. 1099 - 1104.
91. J.J. Petrovic, R.E. Honnell, and A.K. Vasudevan, *SiC reinforced- MoSi_2 alloy matrix composites*, in *Intermetallic Matrix Composites*. MRS Symposium Proceedings, Vol. 194, 1990 MRS: Pittsburgh. p. 123-129.
92. P.S. Frankwicz, J.H. Perepezko, and D.L. Anton, *Phase Stability of MoSi_2 with Cr Additions*, in *High-Temperature Ordered Intermetallic Alloys V*. MRS Symposium Proceedings, Vol. 288, 1993 MRS: Pittsburgh. p. 159-164.
93. J.M. Yang and S.M. Jeng, *Development of MoSi_2 -based composites*. MRS Symposium Proceedings, Vol. 194, 1990 MRS: Pittsburgh. p. 139-146.
94. R.M. Aikin, *On the ductile-to-brittle transition temperature in MoSi_2* . Scripta Metallurgica et Materialia, 1992. 26: p. 1025-1030.
95. K. Sadananda, H. Jones, J. Feng, J.J. Petrovic, and A.K. Vasudevan, *Creep of Monolithic and SiC Whisker-Reinforced MoSi_2* . Ceramic Engineering and Science Proceedings, 1991. 12 [9-10]: p. 1671-1678.
96. P. Grieseson and C.B. Alcock, *The thermodynamics of metal silicides and silicon carbide*, in *Special Ceramics*, P. Popper, Editor, 1960 Heywood: London. p. 183-208.
97. C.R. Kao, J. Woodford, S. Kim, M.-X. Zhang, and Y.A. Chang, *Synthesis of in situ composites through solid-state reactions: thermodynamic, mass-balance and kinetic considerations*. Materials Science and Engineering A, 1995. 195: p. 29-37.
98. B. Aronsson, *The Crystal Structure of Mo_5Si_3 and W_5Si_3* . Acta Chemica Scandinavica, 1958. 9: p. 1107-1110.
99. M.K. Meyer and M. Akinc, *Oxidation Behavior of Boron-Modified Mo_5Si_3 at 800°-1300° C*. Journal of the American Ceramic Society, 1996. 79: p. 938-944.
100. D.J. Thoma, F. Chu, K. McClellan, and P. Peralta, *Processing and Properties of Mo_5Si_3 Single Crystal*. Ceramic Engineering and Science Proceedings, 1998. 19(3-4): p. 413-420.
101. M.K. Meyer, M.J. Kramer, and M. Akinca, *Compressive creep behavior of Mo_5Si_3 with the addition of boron*. Intermetallics, 1996. 4: p. 273-281.
102. A.J. Thom, M.K. Meyer, Y. Kim, and M. Akinc, *Evaluation of $\text{A}_5\text{Si}_3\text{Z}_2$ intermetallics for use as high temperature structural materials*, in *Processing and Fabrication of Advanced Materials III*, V.A. Ravi, T.S. Srivatsan, and J.J. Moore, eds., 1994 TMS: Warrendale, PA. p. 413-438.

103. Y. Kim, A.J. Thom, and M. Akinc, *Synthesis, Processing and Properties of Ti_3Si_2* , in *Processing and Fabrication of Advanced Materials for High Temperature Applications - II*, V.A. Ravi and T.S. Srivatsan, eds., 1993 TMS: Warrendale, PA. p. 189-208.
104. A.J. Thom, M. Akinc, O.B. Cavin, and C.B. Hubbard, *Thermal expansion anisotropy of Ti_3Si_2* , *Journal of Materials Science Letters*, 1994. **13**: p. 1657-1660.
105. A.G. Evans, *Microfracture from Thermal Expansion Anisotropy-I. Single Phase Systems*. *Acta Metallurgica*, 1978. **26**: p. 1845-1853.
106. H. Nowotny and C.H. Brukl, *Ein Beitrag zum Dreistoff: Molybden-Aluminum-Silicium*. *Monatshefte für Chemie*, 1960. **91**: p. 312-318.
107. H. Nowotny, *Alloy Chemistry of Transition Element Borides, Carbides, Nitrides, Aluminides, and Silicides*, in *Electronic Structure and Alloy Chemistry of the Transition Elements*, P. Beck, Editor, . 1963, John Wiley & Sons: New York, NY. p. 179-220.
108. C.H. Brukl, H. Nowotny, and F. Benesovsky, *Untersuchungen in den Dreistoffsystemen: V-Al-Si, Nb-Al-Si, Cr-Al-Si, Mo-Al-Si bzw. Cr(Mo)-Al-Si*. *Monatshefte für Chemie*, 1961. **92**: p. 967-980.
109. L. Brewer and O. Krikorian, *Reactions of Refractory Silicides with Carbon and Nitrogen*. *Journal of the Electrochemical Society*, 1956. **103**(1): p. 38-50.
110. E. Rudy, *Compendium of Phase Diagram Data. Ternary Phase Equilibria in Transition Metal-Boron-Carbon-Silicon Systems*. Vol. V, 1969 AFML, Wright-Patterson Air Force Base: Dayton, OH.
111. A. Costa e Silva and M.J. Kaufman, *The Use of Thermodynamics in the Design of in situ $MoSi_2$ Composites*, in *Processing and Fabrication of Advanced Materials for High Temperature Applications IV*, J.J. Moore and T.S. Srivatsan, eds., 1995 TMS: Warrendale, PA. p. 755-774.
112. R. Radhakrishnan, C.H.H. Jr., J.L. Brimhall, and S.B. Bhaduri, *Synthesis of Ti_3SiC_2/SiC and $TiSi_2/SiC$ composites using displacement reactions in the Ti-Si-C system*. *Scripta Metallurgica et Materialia*, 1996. **34**(12): p. 1809 -1814.
113. M. Suzuki, S.R. Nutt, and J. R.M. Aikin, *Creep Behavior of SiC -Reinforced XD^{TM} $MoSi_2$ Composite*, in *Intermetallic Matrix Composites II*, D.B. Miracle, D.L. Anton, and J.A. Graves, eds.. MRS Symposium Proceedings, Vol. 273. 1992, MRS: Pittsburgh. p. 267-274.
114. A.F. Giamei, S. Chin, D. Berczik, and J. Perepezko. *Advanced High Temperature Molybdenum Alloys & Coatings*. in *AFOSR Structural Metals Workshop*. 1996. AFOSR, Bolling AFB: Washington, DC.
115. J.H. Schneibel, C.T. Liu, M.J. Kramer, and J.J. Huebsch, *Processing, Microstructure, and Properties of Molybdenum-Silicon Intermetallics*. *Ceramic Engineering and Science Proceedings*, 1998. **19**(3-4).

116. C.A. Nunes, R. Sakidja, and J.H. Perepezko, *Phase Stability in High Temperature Mo-Rich Mo-Si-B Alloys*, in *Structural Intermetallics*, M.V. Nathal, et al., eds., 1997 TMS: Warrendale, PA. p. 831-839.
117. E.N. Ross, P.D. Eason, and M.J. Kaufman, *Processing of Low-Silica MoSi₂-Based Compounds*, in *Processing and Fabrication of Advanced Materials V*, J.J.M. T.S. Srivatsan, Editor, 1996 TMS: Warrendale, PA. p. 347-360.
118. D.K. Patrick and D.C. Van Aken, *Physical and Mechanical Properties of MoSi₂-Er₂Mo₂Si₄ Composites*, in *High-Temperature Ordered Intermetallic Alloys V*, MRS Symposium Proceedings, Vol. 288, 1993 MRS: Pittsburgh. p. 1135-1141.
119. P.B. Celis, E. Kagawa, and K. Ishizaki, *Design and production of the Zr₃Ti₂Si₃ intermetallic compound*. Journal of Materials Research, 1991. 6(10): p. 2077-2083.
120. Y. Suzuki and K. Niihara, *Synthesis and mechanical properties of Mo₅Si₃C₃ and Mo₅Si₃C₂-based composites*. Intermetallics, 1997. 6(1): p. 7-13.
121. C.T. Liu and H. Inouye, *Control of Ordered Structure and Ductility of (Fe, Co, Ni)₃V Alloys*. Metallurgical and Materials Transactions A, 1979. 10A: p. 1515-1525.
122. A.H. Cottrell, *Ductile aluminum and brittle trialuminides*. Materials Science and Technology, 1991. 7: p. 981-983.
123. J.S. Wang, *The ductile versus brittle response of LJ₂ intermetallics*. Materials Science and Engineering A, 1997. A239-240: p. 399-403.
124. U.V. Waghmare, V. Bulatov, E. Kaxiras, and M.S. Duesbery, *Microalloying for ductility in molybdenum disilicide*. Materials Science and Engineering A, 1999. A261: p. 147-157.
125. P. Villars and L.D. Calvert, *Handbook of Crystallographic Data for Intermetallic Phases*. 1991, ASM: Metals Park, OH.
126. A. Costa e Silva and M.J. Kaufman, *Microstructural modification of MoSi₂ through aluminum additions*. Scripta Metallurgica et Materialia, 1993. 29: p. 1141-1145.
127. P.D. Eason, E.N. Ross, and L.A. Dempere, *Processing, Microstructure and Mechanical Properties of Mo Silicides and Their Composites*. submitted to Scripta Materialia, 1998.
128. P.D. Eason, K.L. Jolly, and M.J. Kaufman, *Reassessment of the Mo-Si-Al Ternary Isotherm at 1400°C*. Ceramic Engineering and Science Proceedings, 1998. 19(3-4): p. 437-444.
129. M. Moriwaki, K. Ito, H. Inui, and M. Yamaguchi, *Plastic Deformation of Mo(Si, Al)₂ Single Crystals with the C40 Structure*, in *High-Temperature Ordered Intermetallic Alloys VII*. MRS Symposium Proceedings, Vol. 460, 1997 MRS: Pittsburgh. p. 605-610.
130. K. Yanigahara, T. Maruyama, and K. Nagata, *Isothermal and cyclic oxidation of Mo(Si_{1-x}Al)₂ up to 2048K*. Materials Transactions, JIM, 1993. 34(12): p. 1200-1206.

131. V.U. Kodash, P.S. Kisly, and V.J. Shemet, *High temperature oxidation of molybdenum aluminosilicides*. High Temperature Science, 1990. 29: p. 143-152.
132. H. Nowotny, E. Dimakopoulou, and H. Kudielka, *Untersuchungen in den Driestoffsystemen: Molybden-Silizium-Bor, Wolfram-Silizium-Bor und in dem System: VSi_2 - $TaSi_2$* . Monatshefte für Chemie, 1957. 88(2): p. 180 - 192.
133. J.H. Perepezko and C.A. Nunes, *Phase Stability and Microstructural Design in High Temperature (Mo,Nb)-Si-B Alloys*, in *AFOSR Structural Metals Workshop*. 1996. AFOSR, Bolling AFB: Washington, DC.
134. J.O. Andersson, *Thermodynamic properties of Mo-C*. CALPHAD, 1988. 12: p. 1-8.
135. P. Stienmetz, B. Roques, and R. Pichoir, *Etude de la diffusion dans de couples du système ternaire Mo-C-Si*. Journal of the Less-Common Metals, 1976. 48: p. 225-240.
136. A. Costa e Silva and M.J. Kaufman, *Phase relations in the Mo-Si-C system relevant to the processing of $MoSi_2$ -SiC composites*. Metallurgical and Materials Transactions A, 1994. 25A: p. 5-15.
137. E. Parthe and W. Jeitschko, *A neutron diffraction study of the Nowotny phase $Mo_{5/6}Si_3C_{2/3}$* . Acta Crystal., 1965. 19: p. 1031-1037.
138. *Standard Test Method for Size, Dimensional Measurements, and Bulk Density of Refractory Brick and Insulating Firebrick*, in *Annual Book of ASTM Standards*, 1997 ASTM: Philadelphia, PA. p. 35-38.
139. *Standard Methods for Determining the Average Grain Size*, in *Annual Book of ASTM Standards*, 1986 ASTM: Philadelphia, PA. p. 115-148.
140. B.D. Cullity, *Elements of X-Ray Diffraction*. 2nd ed. 1978, Addison-Wesley: Reading, MA.
141. C.R. Herrington, *Quantitative EDS and WDS X-ray Microanalysis of Semiconductor Materials: Principles and Comparisons*. Journal of Electron Microscopy Technique, 1985. 2: p. 471-479.
142. D.B. Williams and C.B. Carter, *Transmission Electron Microscopy*. 1996, Plenum: New York.
143. F.H. Froes, C. Suryanarayana, and D. Eliezer, *Review Synthesis, properties and applications of titanium aluminides*. Journal of Materials Science, 1992. 27: p. 5113-5140.
144. H.E. Cheng, T.T. Tsair, and M.N. Hon, *Multiple twins induced in $\langle 110 \rangle$ preferred growth in TiN and SiC films prepared by CVD*. Scripta Materialia, 1996. 35(1): p. 113 -116.
145. N.S. Jacobson and E.J. Opila, *Thermodynamics of Si-C-O System*. Metallurgical and Materials Transactions A, 1993. 24A: p. 1212-1214.
146. K. Ishizaki, *Phase Diagrams Under High Total Gas Pressures-Ellingham Diagrams for Hot Isostatic Press Processes*. Acta Metallurgica et Materialia, 1990. 38: p. 2059-2066.

147. C.S. Barrett and T.B. Massalski, *Structure of Metals*. 3rd ed. 1966, McGraw-Hill: New York. p. 654.
148. R.E. Reed-Hill, in *Physical Metallurgy Principles*, . 1973, Van Nostrand: New York. p. 365.
149. T.E. Mitchell and A. Misra, *Structure and mechanical properties of (Mo, Re)Si₂ alloys*. Materials Science and Engineering A, 1999. **A261**: p. 106-112.
150. M. Akinc, M.K. Meyer, M.J. Kramer, A.J. Thom, J.J. Huebsch, and B. Cook, *Boron-doped molybdenum silicides for structural applications*. Materials Science and Engineering A, 1999. **A261**: p. 16-23.
151. Y. Ikarashi, T. Nagai, and K. Ishizaki, *Fabrication of zirconium silicide intermetallic compounds with 16H-type crystal structure*. Materials Science and Engineering A, 1999. **A261**: p. 38-43.
152. R. Sakidja, H. Sieber, and J.H. Perepezko, *Microstructural Development of Mo-rich Mo-Si-B alloys*, in *Molybdenum & Molybdenum Alloys*, . 1998, TMS.
153. J.H. Schneibel, C.T. Liu, D.S. Easton, and C.A. Carmichael, *Microstructure and mechanical properties of Mo-Mo₃Si-Mo₃SiB₂ silicides*. Materials Science and Engineering A, 1999. **A261**: p. 78-83.
154. E.L. Courtright, *A comparison of MoSi₂ matrix composites with other silicon-based systems*. Materials Science and Engineering A, 1999. **A261**: p. 53-63.
155. M. Sakai and R.C. Bradt, *Fracture toughness testing of brittle materials*. International Materials Reviews, 1993. **38**: p. 53-78.
156. G.R. Anstis, P. Chantikul, B.R. Lawn, and D.B. Marshall, *A Critical Evaluation of Indentation Techniques for Measuring Fracture Toughness: I, Direct Crack Measurements*. Journal of the American Ceramic Society, 1981. **64**(9): p. 533-538.
157. F. Chu, D.J. Thoma, K.J. McClellan, and P. Peralta, *Mo₃Si₂ single crystals: physical properties and mechanical behavior*. Materials Science and Engineering A, 1999. **A261**: p. 44-52.
158. *Standard Test Method for Flexural Strength of Advanced Ceramics at Elevated Temperatures*, in *Annual Book of ASTM Standards*, 1997 ASTM: Philadelphia, PA. p. 342-351.
159. S. Jayashankar and M.J. Kaufman, *Effect of Oxygen Content on the Superplastic Behavior of MoSi₂/SiC Composites*. Ceramic Transactions, 1996. **79**: p. 163-173.
160. K. Sadananda and C.R. Feng, *Effect of carbon addition on the creep of molybdenum disilicide composites*. Materials Science and Engineering A, 1995. **A192/193**: p. 862-867.
161. D.B. Marshall, *Controlled Flaws in Ceramics: A Comparisons of Knoop and Vickers Indentation*. Journal of the American Ceramic Society, 1983. **66**: p. 127-131.
162. A.S. Jayatilaka, *Fracture of Engineering Brittle Materials*. 1979, London: Applied Science Publishers.

163. T.G. Langdon, in *Deformation of Ceramic Materials*, R.C. Bradt and R.E. Tressler, eds., 1975 Plenum: New York.
164. R.W. Hertzberg, *Deformation and Fracture Mechanics of Engineering Materials*. 4th ed. 1996, Wiley : New York.
165. D.A. Hardwick and P.L. Martin, *Microcracking, Strain Rate and Large Strain Deformation Effects in Molybdenum Disilicide, in High Temperature Silicides and Refractory Alloys*, C.L. Briant, et al., eds.. MRS Symposium Proceedings, Vol. 322, 1994 MRS: Pittsburgh. p. 209-222.
166. G.M. Pharr and M.F. Ashby, *On Creep Enhanced by a Liquid Phase*. Acta Metallurgica, 1983. 31: p. 129-138.
167. A.K. Ghosh and A. Basu, *The Effect of Grain Size and SiC Particulates on the Strength and Ductility of MoSi₂*, in *High Temperature Silicides and Refractory Alloys*, C.L. Briant, et al., eds.. MRS Symposium Proceedings, Vol. 322, 1994 MRS: Pittsburgh. p. 215-222.
168. D.L. Anton and D.P. Shah, *High Temperature Properties of Refractory Intermetallics*, in *High Temperature Ordered Intermetallic Alloys IV*. MRS Symposium Proceedings, Vol. 213, 1991 MRS: Pittsburgh. p. 733-738.
169. J.S. Jayashankar, E.N. Ross, P.D. Eason, and M.J. Kaufman, *Processing of MoSi₂-based intermetallics*. Materials Science and Engineering A, 1997. A239-240: p. 485-492.
170. M.H. Loretto and R.E. Smallman, *Defect Analysis in Electron Microscopy*. 1975, Chapman and Hall: London.
171. T.E. Mitchell, R.G. Castro, J.J. Petrovic, S.A. Maloy, O. Unal, and M.M. Chadwick, *Dislocations, twins, grain boundaries and precipitates in MoSi₂*. Materials Science and Engineering A, 1992. A155: p. 241-249.
172. J.D. Cotton, M.J. Kaufman, and R.D. Noebe, *A Simplified Method for Determining the Number of Independent Slip Systems in Crystals*. Scripta Metallurgica et Materialia, 1991. 25: p. 2395 - 2398.
173. R.W. Hertzberg, *Slip and Twinning in Crystalline Solids*, in *Deformation and Fracture Mechanics of Engineering Materials*, 1989, Wiley: New York. p. 81-90.
174. Y. Umakoshi, T. Nakano, K. Kishimoto, D. Furuta, K. Hagihara, and M. Azuma, *Strength and deformation mechanism of C40-based single crystal and polycrystalline silicides*. Materials Science and Engineering A, 1999. A261: p. 113-121.
175. K. Kawahara, S. Tsurekawa, and H. Nakashima, *Activated slip systems in beta-silicon nitride during high temperature deformation*. Journal of the Japan Institute of Metals, 1996. 60: p. 582-588.
176. F.W. Vahldiek and S.A. Mersol, *Slip and Microhardness of IVa to Via Refractory Materials*. Journal of the Less-Common Metals, 1977. 55: p. 265-278.
177. G.D. Quinn and R. Morrell, *Design Data for Engineering Ceramics: A Review of the Flexure Test*. Journal of the American Ceramic Society, 1991. 74: p. 2037-2066.

178. D.H. Carter, J.J. Petrovic, R.E. Honnell, and W.S. Gibbs, *SiC-MoSi₂ Composites*. Ceramic Engineering and Science Proceedings, 1989. **10(9-10)**: p. 1121-1129.
179. R. Rosenkranz, G. Frommeyer, and W. Smarsly, *Microstructures and properties and high melting intermetallic Ti₃Si₂ and TiSi₂ compounds*. Materials Science and Engineering, 1992. **A152**: p. 288-294.
180. C.L. Fu, *Electronic, elastic, and fracture properties of trialuminide alloys: Al₃Sc and Al₃Ti*. Journal of Materials Research, 1990. **5(5)**: p. 971-979.
181. E.P. George, J.A. Horton, W.D. Porter, and J.H. Schneibel, *Brittle cleavage of L12 trialuminides*. Journal of Materials Research, 1990. **5**: p. 1639-1648.
182. R.A. Varin, M.B. Winnicka, and I.S. Virk, *Strength, Ductility and Fracture of Cubic (L1₂) Titanium and Zirconium Trialuminides, in Structural Intermetallics*, R. Darolia, et al., eds., 1993 TMS: Warrendale, PA. p. 117-124.
183. A.W. Thompson, *Fracture of Intermetallics*, in *Structural Intermetallics*, R. Darolia, et al., eds., 1993 TMS: Warrendale, PA. p. 879-884.
184. D.B. Miracle, *The Physical and Mechanical Properties of NiAl*. Acta Metallurgica et Materialia, 1993. **41(3)**: p. 649-684.
185. I. Baker and P.R. Munroe, *Improving Intermetallic Ductility and Toughness*. Journal of Metals, 1988. **40(2)**: p. 28-31.
186. M. Yoshida, T. Takasugi, and S. Hanada, *Deformation Microstructures of C15 Cr/Nb Laves Phase Intermetallic Compounds*, in *High-Temperature Ordered Intermetallic Alloys VI, Part 2*. MRS Symposium Proceedings, Vol. 364, 1995 MRS: Pittsburgh. p. 1395-1400.
187. W.S. Walston, R. Darolia, and D.A. Demania, *Impact resistance of NiAl alloys*. Materials Science and Engineering A, 1997. **A239-240**: p. 353-361.
188. D.J. Thoma, F. Chu, P. Peralta, P.G. Kotula, K.C. Chen, and T.E. Mitchell, *Elastic and mechanical properties of Nb(Cr,V)₂ C15 Laves phases*. Materials Science and Engineering A, 1997. **A239-240**: p. 251 - 259.
189. P. Bartolotta, J. Barrett, T. Kelly, and R. Smashey, *The Use of Cast Ti-48Al-2Cr-2Nb in Jet Engines*. Journal of Metals, 1997. **49(5)**: p. 48-76.
190. T.G. Nieh and J. Wadsworth, *Recent Advances and Developments in Refractory Alloys*, in *High Temperature Silicides and Refractory Alloys*, C.L. Briant, et al., eds., MRS Symposium Proceedings, Vol. 322, 1994 MRS: Pittsburgh. p. 315-327.

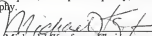
BIOGRAPHICAL SKETCH

Eli Nickerson Ross was born January 24, 1972, in Portland, OR. He attended Cleveland High School where his studies included Russian, journalism, architectural drafting, and advanced chemistry. In his junior year, he was first exposed to the field of materials science and metallurgy by an introductory engineering course for gifted students. After graduating high school in 1989, he enrolled in the department of Materials Science and Engineering at The Johns Hopkins University in Baltimore, MD.

After graduating from Johns Hopkins in 1993, he entered the graduate program in Materials Science and Engineering at the University of Florida in Gainesville, FL. Eli began working under the direction of Dr. Michael Kaufman in 1994, pursuing a specialization in metals while researching high-temperature structural intermetallics. During his time at Florida, Eli had the opportunity to co-author four research publications and give three presentations at materials science conferences. During the summer of 1998, Eli completed an internship at the Boeing Co. in Seattle, working primarily on issues related to titanium investment castings for airframe applications. While in graduate school at Florida, he also studied Japanese for two years. He earned his doctorate in Materials Science and Engineering from the University of Florida in 1999, and accepted a position in materials and processes research and development at Pratt & Whitney in East Hartford, CT.

In his free time, Eli enjoys mountain biking, having ridden in Colorado, Georgia, North Carolina, Oregon, and Washington. In addition to cycling, he pursues other outdoor activities such as hiking, running, camping, kayaking, skiing, and tennis. When not outdoors, Eli can usually be found watching sports, reading, listening to music, or following his interest in aviation and aerospace technology.

I certify that I have read this study and that in my opinion it conforms to acceptable standards of scholarly presentation and is fully adequate, in scope and quality, as a dissertation for the degree of Doctor of Philosophy.


Michael J. Kaufman, Chairman
Professor of Materials Science and
Engineering

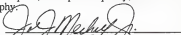
I certify that I have read this study and that in my opinion it conforms to acceptable standards of scholarly presentation and is fully adequate, in scope and quality, as a dissertation for the degree of Doctor of Philosophy.


Reza Abbaschian
Professor of Materials Science and
Engineering


I certify that I have read this study and that in my opinion it conforms to acceptable standards of scholarly presentation and is fully adequate, in scope and quality, as a dissertation for the degree of Doctor of Philosophy.


Robert T. DeHoff
Professor of Materials Science and
Engineering

I certify that I have read this study and that in my opinion it conforms to acceptable standards of scholarly presentation and is fully adequate, in scope and quality, as a dissertation for the degree of Doctor of Philosophy.



John J. Mecholsky Jr.
Professor of Materials Science and
Engineering

I certify that I have read this study and that in my opinion it conforms to acceptable standards of scholarly presentation and is fully adequate, in scope and quality, as a dissertation for the degree of Doctor of Philosophy.


Timothy J. Anderson
Professor of Chemical Engineering

This dissertation was submitted to the Graduate Faculty of the College of Engineering and to the Graduate School and was accepted as partial fulfillment of the requirements for the degree of Doctor of Philosophy.

August 1999


M. Jack Ohanian
Dean, College of Engineering

Winfred M. Phillips
Dean, Graduate School

LD
1780
1999
.R823

